Ground Penetrating Radar

Issue 1, Volume 1

January 2018

www.GPRadar.eu/journal

EDITORIAL

Welcome to Issue 1, Volume 1 of *Ground Penetrating Radar*, the first peer-reviewed scientific journal dedicated to Ground Penetrating Radar (GPR) technology, methodology and applications! Founded in September 2017 as a follow-up initiative of COST (European Cooperation in Science and Technology) Action TU1208 "Civil engineering applications of Ground Penetrating Radar," this is an open-access open-science journal, published quarterly. Our website is www.GPRadar.eu/journal, where all papers are available for free download and an online submission form is waiting for your contributions to the forthcoming issues!

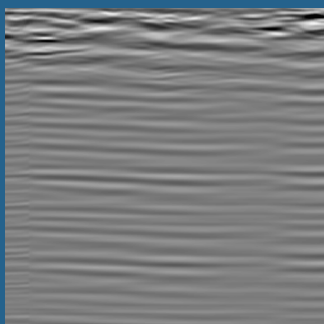The scope of *Ground Penetrating Radar* spans all of the latest and emerging research in the GPR field. Thus, the journal topics cover:

- The development of novel instrumentation;
- The applications of GPR in earth and planetary sciences, environmental and civil engineering, archaeology and cultural heritage, forensics and security, and in any other areas;
- The advancement and use of electromagnetic modelling, imaging, inversion, and data-processing methods for GPR; and,
- The integration of GPR with complementary non-destructive testing techniques.

Ground Penetrating Radar publishes regular research papers, review papers, tutorials, software and data papers, communications, and comments. We also accept manuscripts presenting the outcomes of training, dissemination and outreach activities, as well as papers aiming at communicating to a broader audience with regard to research projects financed with international, European or national funds.

We foster openness, reproducibility and re-use of research. We therefore encourage scientists to publish theoretical, computational and experimental methods and results in as much detail as possible, so that Readers can thoroughly understand and further develop the methods and/or easily reproduce the results. For this reason, there is no restriction on the paper length and supplementary material is most welcome (e.g., data, software, and any other useful electronic file).

GPR is a relatively new inspection technique with a bright future, which started being used in the field of geoscience in the 1950s and rapidly found applications in several other areas. In the last decades, new developments have occurred at an increasing pace and, although the technique has now reached a level of maturity, there still are vast opportunities for further advancements and innovation. The number of GPR-related scientific papers is growing significantly (see Figure 1); over recent years, special issues and books on GPR are published more and more often by

renowned journals and publishing houses. As is well known, GPR has two longstanding dedicated biennial events (the International Conference on Ground Penetrating Radar, held since 1986, and the International Workshop on Advanced Ground Penetrating Radar, held since 2001); additionally, GPR-related sessions are organized in the framework of many international and national conferences. In this landscape, the time is ripe for a GPR journal to start and I am confident that, with the cooperation and support of you all, this challenging but promising project will be a success. *Ground Penetrating Radar* is our journal, created to support and promote the GPR scientific community: all together we can gradually make it a high-quality, innovative, impactful and influential periodical publication.

Our first issue is a humble first step, to kick off this ambitious editorial venture. It includes six papers stemming from recent short-term scientific missions and training schools funded by COST Action TU1208. The second issue is expected for April 2018. *Ground Penetrating Radar* papers are currently processed and published free of charge, thanks to the generous support of the non-profit TU1208 GPR Association.

We welcome your ideas, suggestions, comments, questions, and special-issue proposals! We are looking forward to extending the editorial board and to receiving many interesting manuscripts.

The Editor-in-Chief
Lara Pajewski
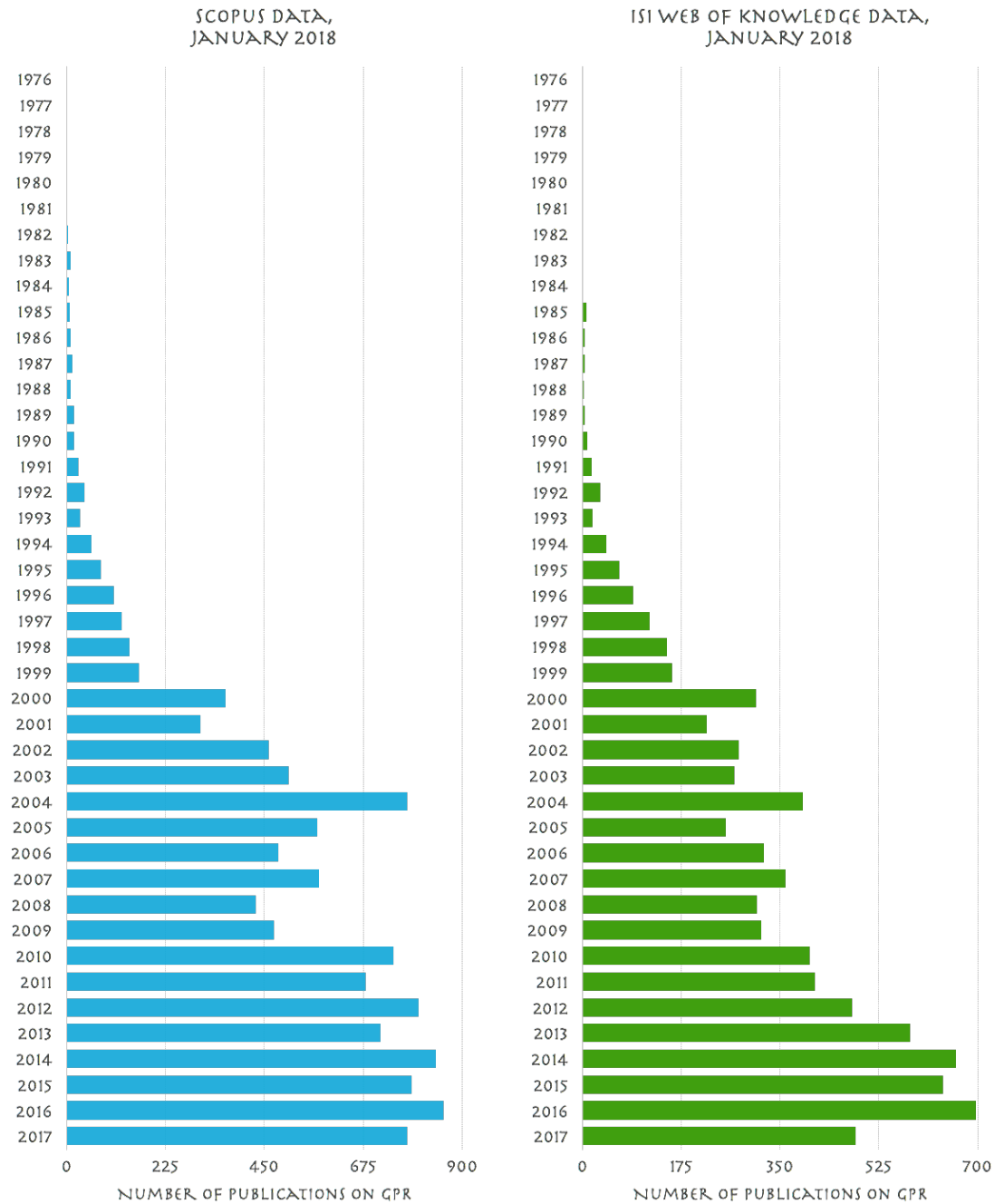
Fig. 1 – Evolution of the number of GPR-related scientific publications over the years. The histogram on the left is obtained from January-2018 Scopus data, whereas the histogram on the right presents January-2018 data taken from ISI Web of Knowledge. Though these data are obviously not exhaustive, they nonetheless give an idea about the increasing trend.

PREFACE

We are delighted and honoured to present the first issue of the first volume of *Ground Penetrating Radar*, which includes six papers stemming from short-term scientific missions and training schools recently funded by COST (European Cooperation in Science and Technology) Action TU1208 "Civil engineering applications of Ground Penetrating Radar" (www.GPRadar.eu). The papers are authored by scientists from eight institutes in five countries (Germany, Italy, Malta, Portugal, Spain).

As is well known, COST (www.cost.eu) is the longest-running European framework supporting trans-national cooperation among researchers, engineers and scholars across Europe. COST Actions are bottom-up science and technology networks where scientists, professionals and stakeholders can jointly develop their own ideas. They are active through a range of networking tools, such as workshops, conferences, training schools, short-term scientific missions, and dissemination activities.

COST Action TU1208 (www.GPRadar.eu) was running from 4 April 2013 to 3 October 2017. Its main objective was to exchange and increase scientific-technical knowledge and experience of Ground Penetrating Radar (GPR) techniques in civil engineering, whilst promoting a wider and more effective use of this safe and non-destructive method in the monitoring of structures. The research activities carried out in the Action included all aspects of the GPR technology and methodology: development and testing of radar systems and antennas; design and application of surveying procedures for the inspection of natural and manmade structures, in civil and environmental engineering, cultural heritage, and beyond; integration of GPR with complementary non-destructive testing methods; development of advanced electromagnetic modelling, inversion and data-processing techniques for radargram analysis and interpretation.

Short-term scientific missions are among the most effective COST networking tools. They are institutional visits aimed at supporting individual mobility across Europe and at fostering collaboration between researchers from different countries; their minimum and maximum duration is 5 and 180 calendar days, respectively. In the framework of TU1208, we have seen very positive results stemming from such missions: several Action Members exploited this networking tool, carried out research together, and were able to achieve impressive results in a short period of time.

The first three papers of this journal issue report and discuss the results of cutting-edge experimental activities carried out in Malta in 2015 and 2016, during two short-term scientific missions and a training school funded by TU1208. Overall, a wide and variegated range of interesting case studies is presented in these three contributions.

The first research paper of the Malta series, entitled "Use of Ground Penetrating Radar and standard geophysical methods to explore the subsurface" and authored by Raffaele Persico and Sebastiano D'Amico, deals with GPR and passive seismic measurements performed in 2015 in several sites of historical and geological interest. Namely, the prospected sites included: an area of the Golden Bay, in the vicinity of Għajn Tuffieħa Tower; an area close to La Ferla Cross church; Madliena tower, in Pembroke; an area outside Santa Maria church, in Birkikara; and, the co-cathedral of St John, in Valletta, a UNESCO World Heritage Site. The used radar system was an innovative reconfigurable stepped-frequency GPR prototype and the investigations carried out in Malta represented a valuable opportunity to test the prototype on various real scenarios.

In the second research paper, entitled "Ground Penetrating Radar investigations in sites of cultural interest in Malta," Raffaele Persico, Sebastiano D'amico, Enzo Rizzo, Luigi Capozzoli, and Aaron Micallef present the results of further GPR measurements performed in Malta in 2016. The reconfigurable stepped-frequency GPR prototype was used to inspect the Argotti Garden in Floriana, where the Authors looked for ancient buried cisterns, and the floor of a Nymphaeum inside the garden, to assess its conditions prior to restoration works. A commercial pulsed GPR system was then employed to assess the walls of the co-cathedral of St. John and of a building of the University of Malta, in Msida.

In the third research paper, entitled "Electrical Resistivity Tomography investigations in Mgarr (Malta)," Raffaele Persico, Sebastiano D'amico, Enzo Rizzo, Luigi Capozzoli, and Aaron Micallef present the results of electrical resistivity tomography (ERT) measurements carried out in 2016 near the village of Mgarr, on the western coast of Malta, in an area of naturalistic and cultural interest. The main objective of the experimental campaign was to perform a hydrogeological study of carbonate rocks close the sea. As is known, ERT allows a deeper penetration than GPR (with a worse resolution) and is often used in combination with GPR.

The journal issue continues with the research paper entitled "Non-destructive tests for railway evaluation: detection of fouling and joint interpretation of GPR data and track geometric parameters." Here, Mercedes Solla and Simona Fontul present the results of a short-term scientific mission funded by TU1208 and carried out in Lisbon, Portugal, in 2015. In particular, the paper deals with the assessment of railways by using GPR, Falling Weight Deflectometer and Light Falling Weight Deflectometer. The Authors investigated how to detect track defects at railway infrastructure level, how to measure the ballast layer thickness, and how to evaluate the fouling level of ballast.

The subsequent contribution is entitled "A practical guide on using SPOT-GPR, a freeware tool implementing a SAP-DoA technique" and is authored by Simone Meschino and Lara Pajewski. This is a software paper, which main objective is to provide practical information on how to use SPOT-GPR release 1.0, a MATLAB®-based software for the analysis of GPR profiles. This tool allows detecting targets and estimating their position in a two-dimensional scenario, it has a graphical user interface and implements an innovative sub-array processing method. SPOT-GPR was developed during three short-term scientific missions funded by TU1208 and carried out in Rome in 2015, 2016, and 2017.

The journal issue is concluded with a tutorial entitled "Thermography: principles and applications," authored by Mercedes Solla and Susana Lagüela. This contribution resumes a lecture given by the first Author during a TU1208 training school on non-destructive testing techniques applied to civil engineering, held in Barcelona, Spain, in 2016. The tutorial presents the main principles of the thermography technique and its civil-engineering applications. Several examples are given and two case studies are described, where thermography and GPR are jointly used to assess a radiant heating floor installed in a building, and to detect moisture in a masonry arch bridge.

The works included in this issue were reviewed by Isabel Rodríguez-Abad, Andreas Loizos, Marian Marciniak, Loredana Matera, Lara Pajewski, and Santo Prontera.

We would like to warmly thank the Authors of the papers and the Reviewers for their efforts. We are grateful to COST for funding and supporting the Action TU1208.

<div style="text-align: right">

Isabel Rodríguez-Abad (Guest Editor)

Marian Marciniak (Guest Editor)

Lara Pajewski (Editor-in-Chief)

</div>

USE OF GROUND PENETRATING RADAR
AND STANDARD GEOPHYSICAL METHODS
TO EXPLORE THE SUBSURFACE

RAFFAELE PERSICO[1] & SEBASTIANO D'AMICO[2]

[1] INSTITUTE FOR ARCHAEOLOGICAL AND MONUMENTAL HERITAGE OF THE NATIONAL RESEARCH
COUNCIL (IBAM-CNR), LECCE, ITALY
R.PERSICO@IBAM.CNR.IT

[2] UNIVERSITY OF MALTA, FACULTY OF SCIENCE, MSIDA, MALTA
SEBASTIANO.DAMICO@UM.EDU.MT

ABSTRACT

This paper presents the results of a series of Ground Penetrating Radar (GPR) and passive seismic measurements performed in Malta in 2015, during a Short-Term Scientific Mission (STSM) funded by COST (European Cooperation in Science and Technology) Action TU1208 "Civil engineering applications of Ground Penetrating Radar." The main purposes of the measurements were: to test the performance of an innovative reconfigurable stepped-frequency GPR prototype, recently upgraded thanks to the results of the research activities carried out in Norway during a previous TU1208 STSM; to investigate the geological conditions of some sites of historical and environmental interest; and to assess the internal status of two monuments. To the best of our knowledge, the GPR measurements carried out during this STSM constitute the first GPR investigations ever performed in Malta.

KEYWORDS: Ground Penetrating Radar; Instrumentation development; Stepped frequency; Cultural heritage; Geology; Passive seismic.

1. INTRODUCTION

A Short-Term Scientific-Mission (STMS) entitled "Use of Ground Penetrating Radar and standard geophysical methods to explore the subsurface" was recently funded by COST (European Cooperation in Science and Technology), in the framework of the COST Action TU1208 "Civil engineering applications of Ground Penetrating Radar" activities. Raffaele Persico visited Sebastiano D'Amico in Malta, from July 13th to July 24th, 2015, and they jointly performed a series of Ground

Penetrating Radar (GPR) and passive seismic measurements in sites of of historical and environmental interest.

The used radar system was an innovative reconfigurable stepped-frequency GPR prototype (Section 2). The original version of this prototype was implemented in Italy, by the Institute for Archaeological and Monumental Heritage of the National Research Council (IBAM-CNR), in cooperation with the University of Florence and the Italian company IDS Ingegneria dei Sistemi, within the research project AITECH funded by Regione Puglia (www.aitechnet.com/ibam.html) [1]. During a previous STSM funded by the COST Action TU1208, carried out in 2014, the prototype was brought to Norway and compared with commercial systems manufactured by 3d-radar [2]. Based on the results collected during that mission, the prototype was improved. The STSM in Malta represented an opportunity to test on real scenarios the improved version of the prototype.

For what concerns the passive seismic acquisitions, single station-location measurements were done.

The geology of Malta is shortly described in Section 3, whereas Section 4 is dedicated to the presentation and interpretation of the obtained results. The main objectives of our measurements were three: to test the performance of the GPR prototype, to study the geological conditions of a series of sites in Malta, and to assess the conditions of some monuments, still in Malta. In particular, we performed measurements in the Golden Bay area, in the vicinity of Għajn Tuffieħa Tower (subsection 4.1); we assessed an area close to La Ferla Cross church (subsection 4.2); we performed measurements inside Madliena tower, in Pembroke (subsection 4.3); and we surveyed the area outside the church of Santa Maria, in Birkikara (subsection 4.4). GPR and passive seismic analyses were performed also in the co-cathedral of St John patrimony of UNESCO, with the aim to test the displacement of some tombs under the floor and investigate the causes of a fracture, which is evident on one of the headstones (subsection 4.5). Measurements performed to test the performance of the improved GPR prototype are presented in subsection 4.6.

To the best of our knowledge, the GPR acquisitions carried out during this STSM constitute the first GPR investigation ever performed in Malta.

2.   EQUIPMENT

The reconfigurable stepped-frequency GPR prototype, which was used to perform the measurements presented in this paper, is equipped with three equivalent couples of antennas, achieved by means of two series of switches along the arms of a couple of bow-tie antennas. The on and off states of the switches make electrically longer or shorter the bow-tie antennas, thus achieving efficient transmission on three different bands that overall cover the frequency range from 50 MHz to 1 GHz. Accordingly, from now on we will distinguish a couple of low-frequency antennas (with a central frequency around 120 MHz), a couple of medium-frequency antennas (with a central around 250 MHz), and a couple of high-frequency antennas (with a central frequency around 500 MHz) [3]. The prototype can gather data with the three equivalent couples of antennas during each profile acquisition, so that it is possible to obtain three B-Scans for each measurement line.

This feature of the prototype can be very useful because, as is well known, a trade-off always has to be achieved between the desired resolution of the GPR images (a better resolution is possible with higher frequencies) and the penetration depth of the GPR radiation (a deeper penetration is possible with lower frequencies). The resolution and depth of course depend also on the electromagnetic properties of the soil. As the condition of the soil and the depth of the sought targets are not always known a-priori, the large quantity of data gathered by the prototype provides robustness against these uncertainties. The same purpose might be reached with a system equipped with three separate couples of antennas. However, such a system would be necessarily larger and heavier than the prototype. Moreover, to the best of our knowledge, no commercial systems with three couples of antennas exist, but only systems with two couples of antennas at most (unless the systems equipped with antenna arrays are considered).

On the other hand, the large amount of gathered data prevents (at the moment) the visualization of the B-Scans in real time. As a possible future development, more efficient acquisition software will be developed (e.g., based on the C language, whereas the current code is written in MATLAB). This new software, along with a more powerful laptop (e.g., equipped with a parallel processor), will allow overcoming this limitation.

Another interesting and innovative feature of the reconfigurable prototype is the possibility to program the integration time of the radiated and received harmonic signals. This option can be useful in order to counteract narrow-band interferences in an efficient way. In particular, commercial stepped-frequency systems allow, at most, setting the integration time of all the radiated and received harmonic tones. This means that, if interference is recognised, it is possible to counteract it only by prolonging the integration time of all the harmonic tones, which is redundant and above all meaningfully prolongs the time required for gathering the data. In the reconfigurable prototype, instead, we have set and tested a method for recognising, in the field, the most disturbed tones (if any), and we have developed and implemented an algorithm that increases the integration times accordingly to the recorded disturbance, tone by tone. This allows to save time and prevents the measurements from becoming too long and expensive.

The algorithm for the choice of the reconfiguration times works as follows. As a first step, a preliminary B-Scan is performed, possibly coinciding with the first B-scan of interest for the GPR prospecting at hand. For each trace of this B-scan, and for each harmonic tone within the trace, N samples of the in-phase and in-quadrature (I and Q) components are retrieved and stored, and the variance of the I and Q samples is calculated as

$$
\begin{cases}
\sigma_{I;f_k,t_h}^2 = E\left[\left(I_{f_k,t_h}\right)^2\right] - \left[E\left(I_{f_k,t_h}\right)\right]^2 \\
\sigma_{Q;f_k,t_h}^2 = E\left[\left(Q_{f_k,t_h}\right)^2\right] - \left[E\left(Q_{f_k,t_h}\right)\right]^2
\end{cases}
\tag{1}
$$

where E indicates the algebraic average of the samples. Then, the variance σ_{f_k,t_h}^2 of each tone is retrieved for each trace, as the algebraic average of $\sigma_{I;f_k,t_h}^2$ and $\sigma_{Q;f_k,t_h}^2$. Subsequently, and conservatively, we keep the maximum of the variance for each tone, as an index representing the degree of disturbance at each frequency. Moreover we keep the quantity $\sigma_{f_k}^2 = max_h(\sigma_{f_k,t_h}^2)$ for each trace, which is the maximum variance over the traces for each tone; this quantity is a function of the frequency. Afterwards, by visualizing the graph of σ_f^2 versus frequency, we can decide whether a reconfiguration of the integration time of each tone is needed or not. At this point, if we decide to apply a reconfiguration, we have just to set an integer number M>1, which quantifies the maximum "degree" of reconfiguration needed in the case

at hand. Then, the reconfiguration code calculates a factor of enlargement for each integration time according to the formula:

$$F(k) = C_{eil}\left(M\,\frac{\sigma_{f_x}^2}{max_k\left(\sigma_{f_x}^2\right)}\right) \tag{2}$$

where F is the factor of enlargement for the kth tone and the function C_{eil} stands for the minimum integer not smaller than the argument. In other words, an enlargement time is calculated for the most disturbed tone, while the other ones are about proportionally less enlarged with the implicit care that the reconfiguration will never shorten the default integration, which is guaranteed by the C_{eil} function. Indeed, the hardware of the system does not allows an enlargement of the default integration time beyond a factor equal to 10, and therefore a subsequent "if-then" instruction saturates to 10 any value $F > 10$. This because the hardware of the GPR system can prolong at most 10 times the default integration time of each harmonic tone. Let us explicitly note that the chosen algorithm is not semantically equivalent to impose that F is minor or equal to 10.

Passive seismic techniques where used to gather useful data to be compared and integrated with those obtained with the GPR prototype.

The ambient noise was recorded by using a three-component seismometer Tromino™ *(www.tromino.eu)*. The Tromino is a compact, lightweight and self-contained instrument; its ease of use makes it ideal to perform a large number of measurements in rugged terrains that are accessible only on foot. Time series of 20 min each were recorded at a sampling rate of 128 Hz and, by following the guidelines suggested by the SESAME project [4], these were divided into 60 non-overlapping time windows, 20-s each. The Fourier spectrum of each window was computed and smoothed, and after 'cleaning' the traces from spurious noise event windows, the resulting H/V, in the frequency domain, was derived by using the geometric mean of the spectral ratio obtained for each time window. The use of the H/V method was first proposed in [5] for the estimate of seismic site response. A subsequent study [6] eventually made this method widely popular as a cost-effective and reliable means of predicting the resonance frequency of a site, particularly when low shear-wave velocity layers present a sharp impedance contrast with the bedrock.

The presence of a resonance peak in the H/V ratio can be interpreted in terms of *SH*-wave resonance in soft surface layers, or in terms of the ellipticity of particle motion when the ambient noise wave train is made up predominantly of surface waves [7]. In practice, the wavefield is expected to be a combination of both types, and the H/V curve contains information about the shear wave velocity profile in shallow sediments.

3. THE GEOLOGY OF MALTA

The experimental results presented in this paper were obtained in several sites in Malta, as depicted in Figure 1.

The geology of the Maltese Islands is well known (see [8, 9] and references therein) and consists of four main sedimentary layers; the relief, which is largely controlled by the neotectonic pattern, is rather complex. The sedimentary sequence was deposited during the Oligocene and Miocene epochs. Starting from the oldest one, the sequence of strata consists of:

FIG. 1 – Map showing the location of the sites were GPR and passive seismic measurements were performed during the STSM.

(i) The Lower Coralline Limestone (LCL) formation (Chattian): This is the oldest unit of rock visible above sea level. It is a hard and compact pale grey limestone, rich in coralline algae, and can be over 140 m thick. The LCL forms the sheer cliffs bordering the south-western coast of the Maltese Islands.

(ii) The Globigerina Limestone (GL) formation (Aquitanian–Langhian): This layer is made up of soft yellowish fine-grained limestone. Its thickness varies between 20 m and 200 m. The fine-grained GL is lightly cemented making this layer soft and easily cut, sculpted and eroded. It is subdivided into three sublayers: the Lower (Mlg), the Middle (Mmg) and the Upper Globigerina Limestone (Mug). These three layers are separated by two thin hard ground conglomerate layers (Mc1/Mc2), which are much harder and more resistant to erosion, and easily identified when exposed.

(iii) The Blue Clay (BC) formation (Serravallian to early Tortonian, denoted as Mbc): This layer can be considered as a continuation of the Globigerina Limestone, being composed of very fine grained sediment and containing deep water planktonic organisms. The main difference is the higher clay mineral content which gives this layer the banded bluish grey colour. The mix of clay between the lime rich sedimentary grains prevent the binding of the particles hence it is the softest layer of all and is eroded very quickly with rain water. Very often it provokes landslides and in various parts of the islands it forms 45° talus slopes over the underlying strata. Its depth varies between 20 m and 70 m, thinning notably from west to east of the archipelago [8]. Above the Blue Clay Formation there is a thin layer of bioclastic limestone named the Greensand Formation (Mgg). This layer varies from 1 m to 11 m in depth and is present only in a limited number of areas of the islands.

(iv) The Upper Coralline Limestone (UCL) formation (late Tortonian–early Messinian): this is the uppermost, and youngest layer and was formed in very similar conditions as the Lower Coralline Limestone, in shallow waters. This hard pale grey layer can reach thicknesses of more than 160 m in certain parts of the islands. As with the LCL, the layer presents a variety of facies ranging from reef limestone to cross-bedded sands and fine-grained muds. No marine sediments younger than the UCL are found on the islands, indicating that the time of uplift of the islands above sea level together with the northern flank of the Sicily Channel Rift [9] occurred around 6 Ma ago. This uplift coincided with

the closure and partial desiccation of the Mediterranean during the Messinian. Some patchy deposits of the Pleistocene epoch containing remains of terrestrial fauna were laid down on land by fluvial action and are mostly found near shorelines and in caves. Over approximately the eastern half of the island of Malta, the BC and UCL layers are absent, the GL being the outcropping layer. The western half of Malta, together with the island of Gozo, on the other hand, conserve the whole sedimentary sequence and are largely surfaced by UCL at a relatively high elevation, underlain by the BC layer, except for eroded topographical features.

As mentioned in Section 2, in this study we performed ambient noise measurements; these were used to investigate the dynamic characteristics of features at different stages of the destabilization process affecting the cliff area on the Maltese Islands. In fact, the archipelago has several areas of coastal instability characterized by active lateral spreading, rock sliding and rock falls. The instability happens to be situated in areas of coastal land that are used as amusement parks [10], urban areas [11], as well as cultural heritage sites; it has therefore solicited some concern.

In the northern part of the island of Malta, as well as in Gozo, the geomorphology is mostly dictated by the fact that the UCL forms a rigid rock slab resting on a much weaker layer of clayey material. This geological situation creates stresses in the upper slab resulting in fracturing and brittle collapse [12]. When the exposure of the geological cross-section is along the coast, the additional weathering effect of marine processes accelerates the destabilization by erosion of the clay layer. This results in the formation of large cliff-parallel surface fractures that produce partially isolated blocks having volumes of the order of thousands of cubic metres. Horizontal and vertical mass movement of such blocks forming part of the cliff face, and boulder detachment and collapse, result in a fractured and boulder-strewn coastline, that is typical of much of the northwest coast of Malta.

4. RESULTS AND INTERPRETATION

4.1. MEASUREMENTS IN THE GOLDEN BAY

We performed a first set of measurements in the Golden Bay area, in the vicinity of Għajn Tuffieħa Tower. The tower is part of the fortification

structures built by the knights of St. John. In particular, it belongs to the "Lascari towers" constructed between 1637 and 1652 and commissioned by the Italian knight Giovanni Paolo Lascaris who was Grand Master of the Order. The area is affected by the presence of later spreading and retreating of the cliff edge, due to the fracturing of the Upper Coralline overlaying the Blue Clay, as explained in Section 3.

The area prospected with GPR is approximately indicated by a red rectangle on the Google satellite map reported in Figure 2. This area was chosen because of the presence of large fractures in the nearby region. The arrows show two points where the soil collapsed. Figure 2 also shows the location of the single-station measurements and the position where H/V results were obtained, whereas Figure 3 presents the passive-seismic results.

By examining Figure 3, notable characteristics can be identified for each investigated location. The first important observation is the presence of an ubiquitous resonance peak between 1.0 Hz and 2.0 Hz, and a dip in the spectral ratio below 1.0 over a wide frequency range. This is not surprising because previous ambient noise studies did repeatedly confirm similar results [11, 13, 14]. The dip in the H/V ratio can be interpreted in terms of a shallow shear-wave velocity inversion, which in this case corresponds to the interface between the UCL and BC. The interpretation of other features of this peak, in terms of Rayleigh wave ellipticity and/or trapping of SH waves in the low-velocity layer, is the subject of an ongoing study that makes use of numerical modelling. Moving from the inland area towards the cliff edge and rock sliding area, the nature of the H/V response changes strikingly. On the plateau away from the cliff edge, the site response shows only the simple and consistent peak at around 1.5 Hz, as described above, whereas the rest of the H/V amplitudes remain at a level well below 2.0. Moreover, it is noted that at higher frequencies of the spectrum there are peaks not observed on the plateau area, which may be tentatively associated with mechanical vibration modes of the whole blocks.

The area investigated by using the GPR is about 5.2 m × 6.5 m wide. This area was prospected by acquiring a series of parallel B-Scans, directed toward the sea and spaced 40 cm from each other. All the B-Scans end in proximity of the cliff, which is about 30 m high and sharply overhanging the sea.
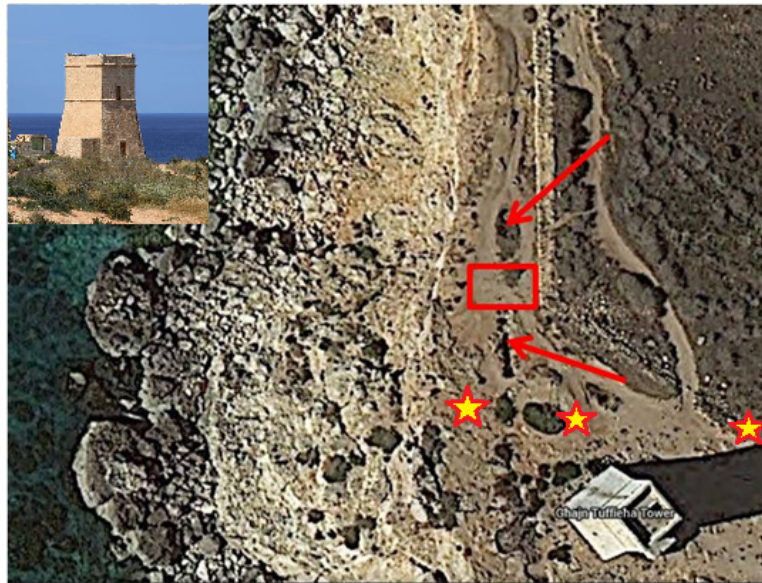
FIG. 2 – Golden Bay. The area prospected with GPR is approximately indicated by a rectangle. The arrows show two points where the soil is collapsed. The stars indicate the location of single-station measurements.
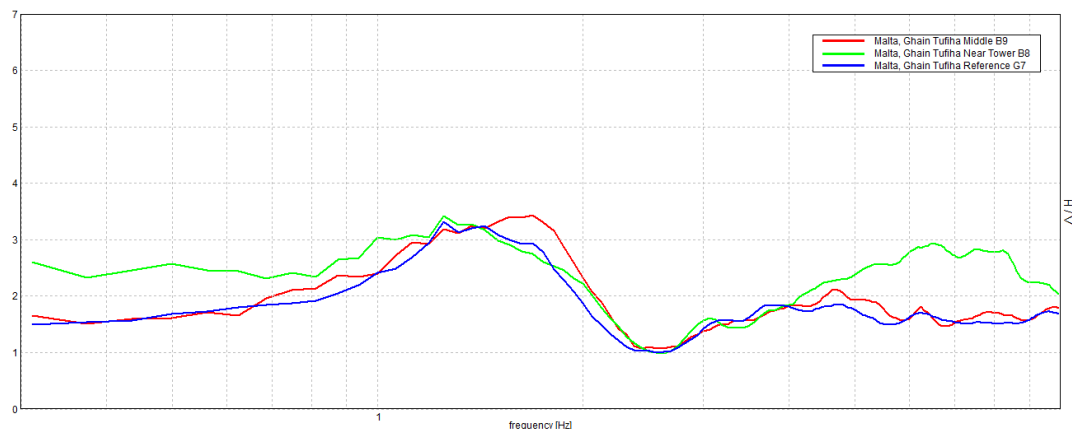
FIG. 3 – H/V curves (average H/V versus frequency) obtained at the three different sites, in the Golden Bay.

In Figures 4-7, horizontal slices at different time-depth levels are reported, showing that the subsidences have a deep track. The two subsidences appear to be separated; however, they could join each other in the future, if the phenomenon is progressive. In this case study, the data recorded by the low-frequency antennas have been exploited, because the anomalies of interest are quite extended and it was important to achieve a high penetration depth of the signal. The

data processing was minimal and included zero timing, application of gain versus depth, background removal, and slicing [15]; no migration was performed, being the anomalies quite large; the Reflexw commercial software was used [16]. Let us mention that the conversion time-depth was done on the basis of the fact that the cliff is made of limestone and the soil was dry. The B-Scan did not show any meaningful hyperbola associable to a small target, therefore the method of the diffraction hyperbolas [17, 18] was not applicable, neither we had at disposal separable antennas in order to perform a common mid-point (CMP) measurement.

FIG. 4 – Horizontal slice at shallow depth, superimposed on the Google satellite image of the Golden Bay.
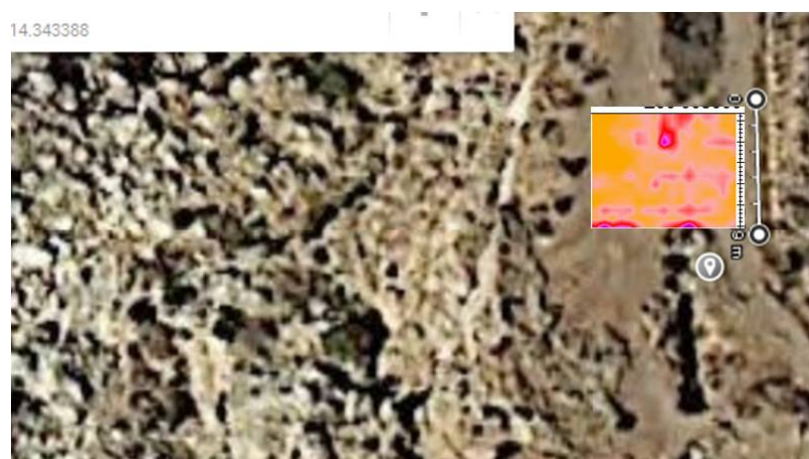
FIG. 5 – Horizontal slice at 15 ns, corresponding to a depth of about 85 cm.
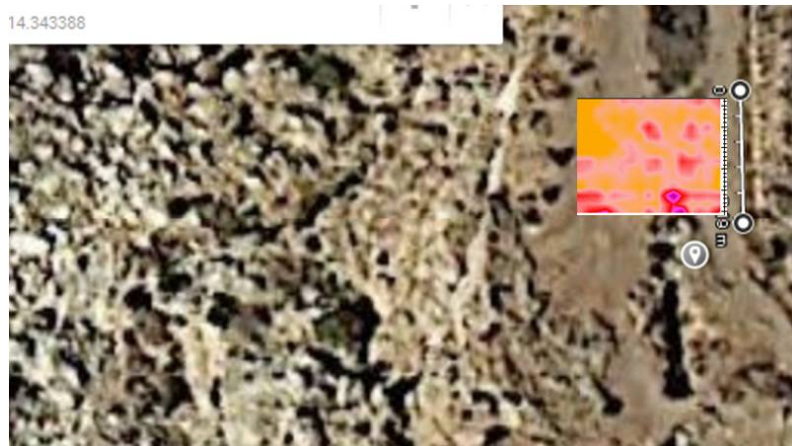
FIG. 6 – Horizontal slice at 30 ns, corresponding to a depth of about 170 cm.

FIG. 7 – Horizontal slice at 50 ns, corresponding to a depth of about 280 cm.

4.2. MEASUREMENTS AT LAFERLA CROSS, MALTA

After the case study of the Golden Bay, essentially done for geological reasons, we dealt with a survey of interest for both geological and engineering reasons, which also reminded us of a previous study carried out in Italy [19].

The church of Laferla is an abandoned construction on the top of a small hill, near to Laferla Cross. In Figure 8, the church is the building on the low-middle part of the image. There is a geological sliding in that area, which has strongly damaged the church. Indeed, the access to the church is prohibited because dangerous. People living in the area are attached to this old church and there are proposals of moving the

building away from its current position. We performed a preventive investigation, to check the situation of an area nearby the church.

It was not easy to perform a complete series of parallel B-Scans here, because of the irregular topography of the soil, and so we performed 6 B-Scans, as referenced in Figure 8. We did not have at our disposal a GPS system; therefore, the position of the B-Scans is qualitative, based on our sketches and on some distances taken by us in the field. Due to the purposes of this prospecting, the most interesting data were those recorded by the medium-frequency antennas. The processing was the same as that described for the Golden Bay, but the data have been migrated too, because in this case it was possible to evaluate the propagation velocity from diffraction hyperbolas (the estimated value was about 12 cm/ns). In the following, we discuss and interpret the various B-Scans.

In Figure 9, the processed B-Scan No. 1 is shown. This B-Scan was recorded parallel to one of the sidewalls of the church, which has a big fracture in its central part. We were therefore looking for something buried in the subsoil, which could be correlated to this fracture. The B-Scan shows some anomalies, the most evident of which is at the abscissa 80 cm and between 10 ns and 20 ns: we deem it ascribable to some boulder or ashlar (because it is large, but the reflection is not strong), and not to the fracture.

The processed B-Scan No. 2 is presented in Figure 10. Here, we appreciate that the soil is layered in the first 20 ns (corresponding to about 120 cm) and we also see at least three relevant discontinuities. The strongest one, between the abscissas 8 m and 10 m, is possibly related to a cavity with reinforced ceiling. In fact, it is known that there is a cavity in that area, which ceiling was reinforced; maybe, the floor of the cavity produces the multiple flat reflections that can be seen below that anomaly. Another strong but localized anomaly is visible around the abscissa 5 m: this might be associated to some boulder. Two further meaningful discontinuities can be observed under the first 2 m of the scan, between the abscissas 16 m and 18 m. The second one of these discontinuities is quite meaningful and might be related to another cavity, else to a part of the same cavity visible between the abscissas 8 m and 10 m, but with a non-reinforced ceiling. There is also an anomaly visible in the first meters of the B-Scan, possibly connected to the B-scan No. 6 as discussed later on.

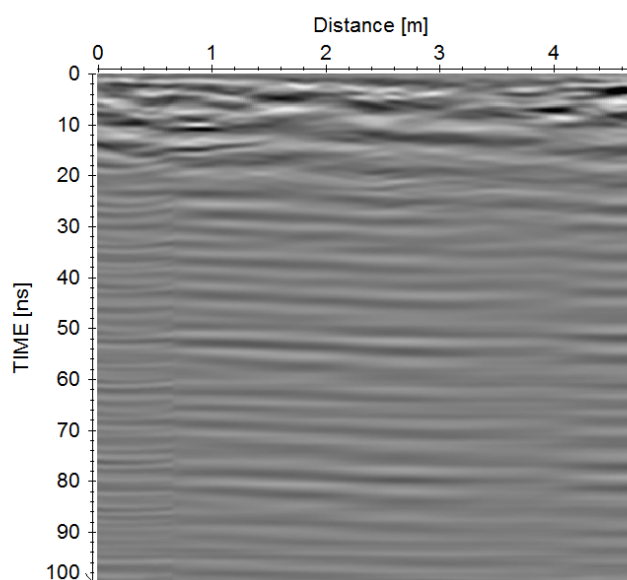**FIG. 8** – La Ferla church and the B-Scans performed close to it.

FIG. 9 – B-Scan No. 1 of Fig. 6.
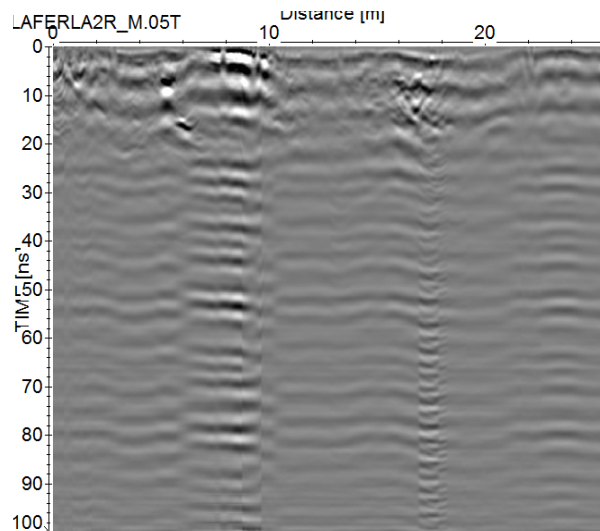
FIG. 10 – B-Scan No. 2 of Fig. 6.

The processed B-Scan No. 3 is reported for the sake of completeness in Figure 11, but these data do not show any anomaly of interest apart from a confirmation of some layering of the shallower part of the soil.

The processed B-Scan No. 4 is presented in Figure 12 and shows a large anomaly between the abscissas 2 m and 6 m. This anomaly is probably related to the one visible in B-Scan No. 2 between the abscissas 16 m and 18 m, and it enforces the hypothesis of a buried cavity in that area. A second anomaly is present in B-Scan No. 4, between the abscissas 8 m and 12 m. This anomaly seems to be the contact line between two zones with different properties of the soil and might be related to some work done in the past.

The processed B-Scan No. 5 is reported in Figure 13. Here, we see a strong and large superficial anomaly between the abscissas 5.2 m and 8 m, which we ascribe to the reinforced ceiling of a cavity. In particular, we deem that this strong anomaly can be related to the strong superficial anomaly visible between 8 m and 10 m in B-Scan No. 2. A meaningful reflection among the abscissas 10 m and 12 m is also visible in Figure 13, possibly ascribable to a material of different consistency.

Finally, in Figure 14 the processed B-Scan No. 6 is presented, where several anomalies are visible. We identify an oblique descending part of the trace in the first part and an oblique ascending part from about 6 m and 8 m. We know that in that area a collapse happened in the past

and was filled up. We interpret the B-Scan No. as a cut of the collapsed area. In particular, looking at the displacement of the B-Scans and at the first 7.5 m of B-Scan No. 2, we notice some resemblance between the sort of filled tank that appears in B-Scan No. 6 and something similar in B-Scan No. 2, indicating possibly two different cuts of the same collapsed and subsequently filled up hole.
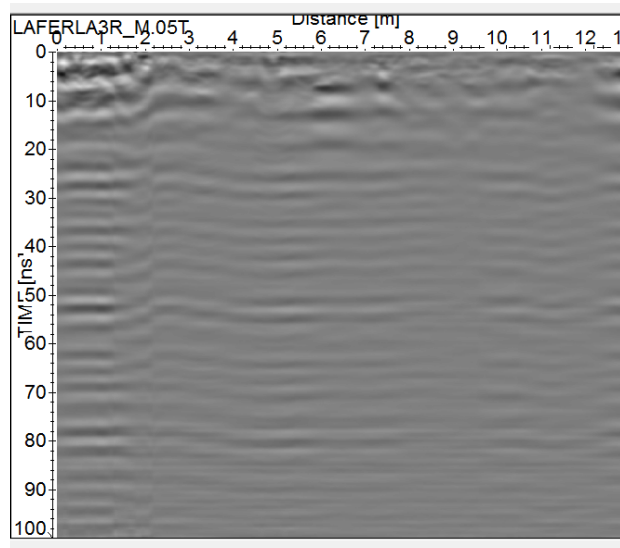

FIG. 11 – B-Scan No. 3 of Fig. 6.
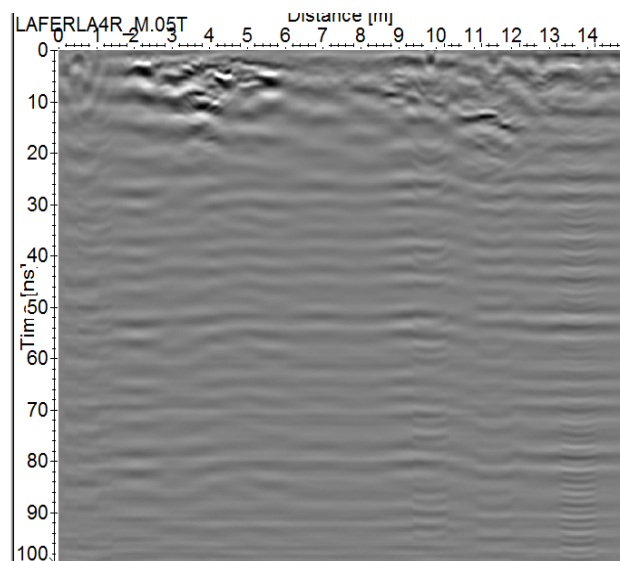
FIG. 12 – B-Scan No. 4 of Fig. 6.
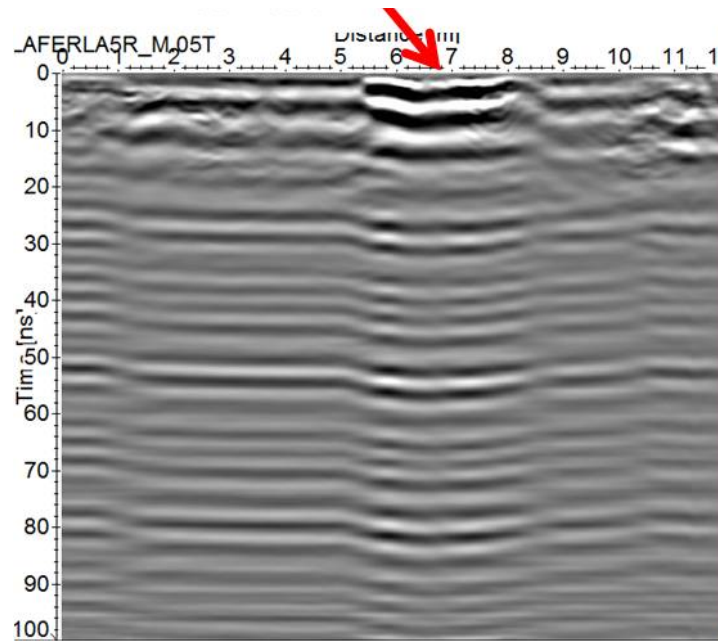
FIG. 13 – B-Scan No. 5 of Fig. 6.
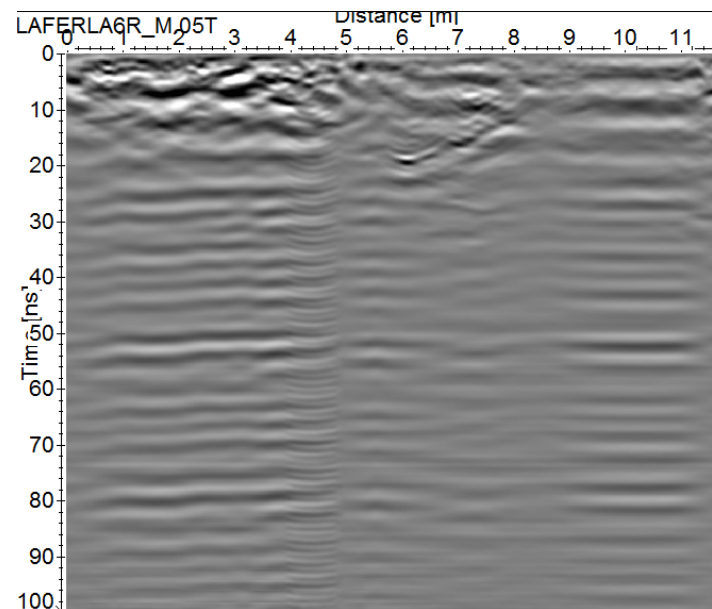
FIG. 14 – B-Scan No. 6 of Fig. 6.

Overall, the GPR measurements show a stratified soil, at least in the shallower layers (down to about 1.2 m), with several anomalies, part of which may be ascribable to buried cavities.

4.3. Measurements in Madliena Tower, Pembroke

Madliena tower is a mighty structure, exploited as a watchtower between 1658 and 1659; it has with very thick walls, because it was a military defensive structure. A photo of the tower is shown in Figure 15.

The inner of the tower, at the ground floor, is a rectangular room with size 2.9 m × 3.9 m, plus a small corridor towards the entrance door. We prospected the room by using our GPR prototype, with spacing between parallel profiles of 20 cm. We exploited an option of the instrument that allows assembling the manhole in a vertical position. Usually the manhole of a GPR is slightly oblique, because in this way the human strength for pushing the instrument is dynamically better exploited. However, an oblique manhole is practical (and in many cases essential) when the prospecting is done on the grass. Indoor, the mechanical resistance to the rotation of the wheels is customarily much lower, and a vertical manhole allows saving space and prospecting a larger area.

FIG. 15 – Madliena tower at Pembroke.

In Figures 16-19, depth slices at different depths are shown. These data were gathered with the medium-frequency antennas and the processing steps were the same as in the investigations presented in the previous subsections of this paper. In the present case study, the data were not migrated because we did not have accurate information about the propagation velocity. The GPR results suggest the presence of a

foundation structure, with walls reaching a depth of at least 1 m in the subsurface, possibly enlarging with depth. Such foundation is probably excavated directly in the rock. The lack of an accurate value of the propagation velocity prevents us from more detailed evaluations.

The tower was also probed with a passive seismographic device: the results are presented in Figure 20. Measurements were taken at the top and middle levels of the tower, and at the ground floor. The ground-floor data confirm that the tower is located on a solid rock: as seen in previous studies, this gives a flat response in the H/V curve [13, 14]. The high-frequency peaks (between 100 Hz and 200 Hz) may be due to a thin layer of soil (shown also by the GPR), but further investigations and numerical modelling are needed to confirm this hypothesis. At the roof level, the fundamental frequency (i.e., the lowest frequency of the building) is clearly identified at about 6 Hz. Higher frequency modes were difficult to identify because the structure is not very high.
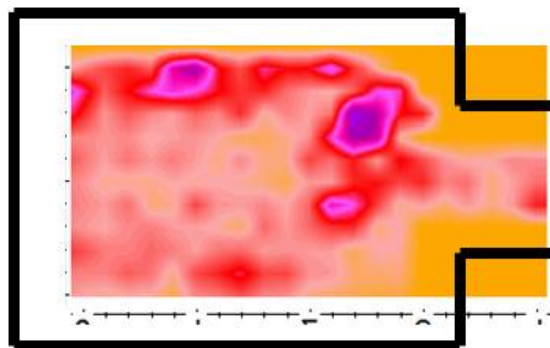
FIG. 16 – Horizontal slice at 5 ns (about 25-35 cm), from data recorded at the ground floor of Madliena tower. The homogeneous orange colour indicates areas where the GPR instrument could not pass.
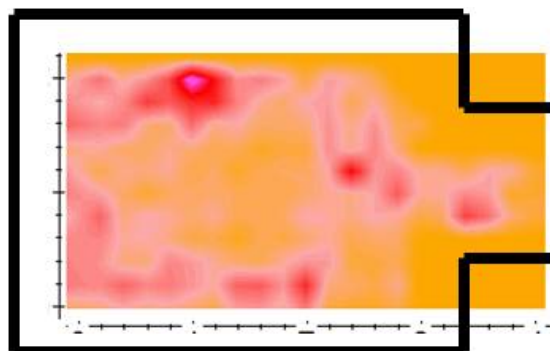
FIG. 17 – Same as in Fig. 16, at 10 ns (about 50-75 cm).
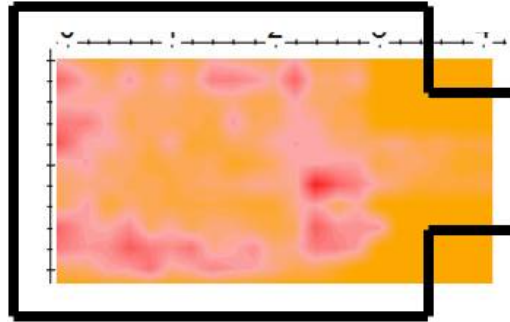
FIG. 18 – Same as in Fig. 16, at 15 ns (about 75-108 cm).
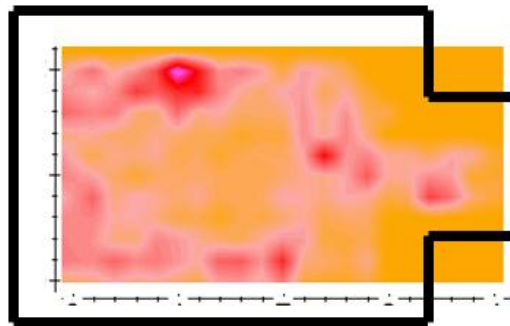
FIG. 19 – Same as in Fig. 16, at 20 ns, about (100-150 cm).
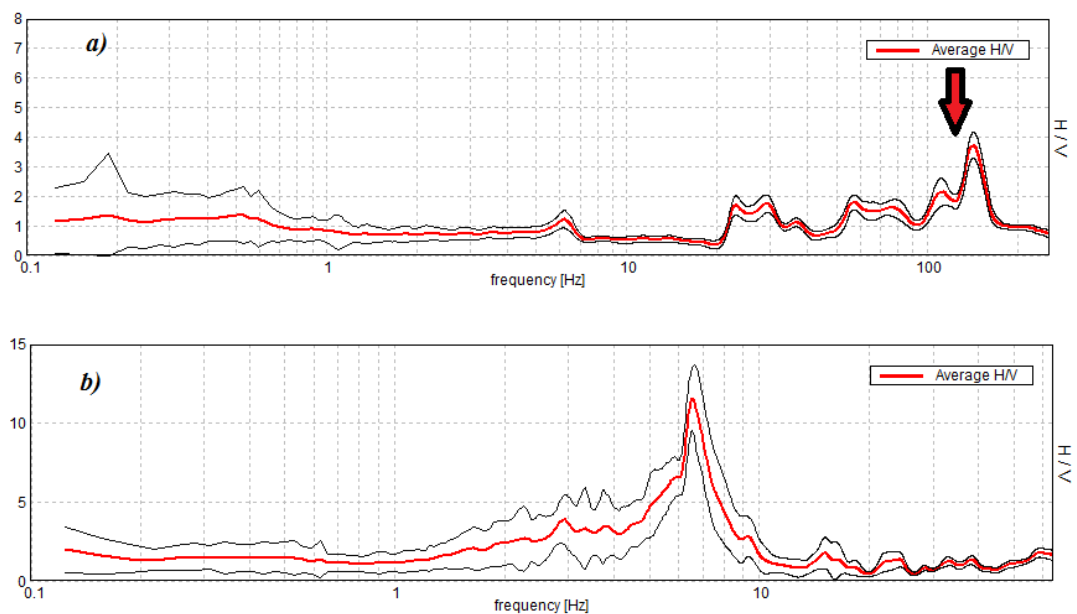
FIG. 20 – Seismographic results in Madliena tower. The top and bottom panels show results obtained on the ground floor and at the roof level, respectively.

4.4.   MEASUREMENTS OUTSIDE THE CHURCH OF SANTA MARIA, BIRKIKARA

Measurements were performed also outside the church of Santa Maria, a historical building where structural problems had been noticed. In particular, some fractures and movements of the walls were observed.

GPR data were gathered with 50-cm spacing between adjacent profiles. The results presented in Figure 21 (horizontal slices at different depths) were recorded by the medium-frequency antennas. The processing was the same as in the previous cases. The notch on the white lines corresponds to a length of 2 m. The homogeneous orange colour indicates areas where the GPR could not pass.

The data show a confused situation at the shallowest levels, which were strongly reshuffled in the 20th century. After 10 ns, more isolated

Slice at 5 ns, about 25 cm	Slice at 10 ns, about 50 cm
Slice at 15 ns, about 75 cm	Slice at 20 ns, about 100 cm
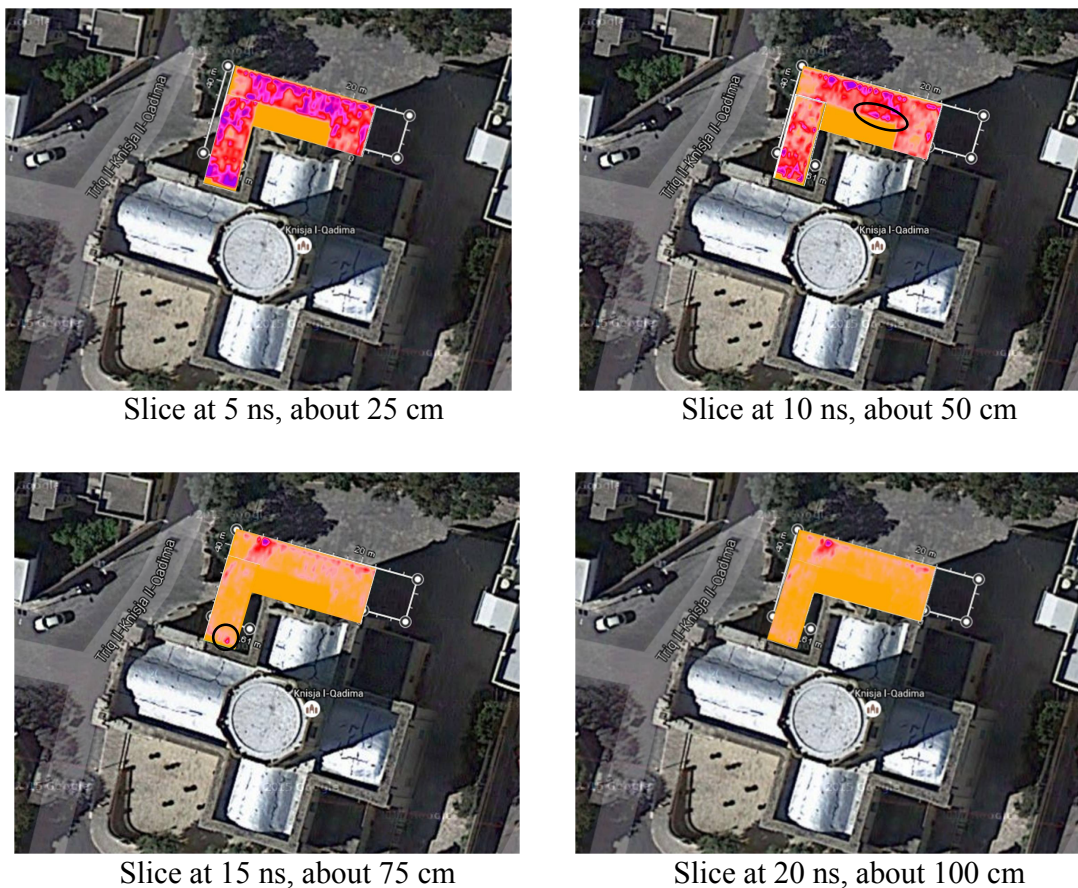
FIG. 21 – Horizontal slices at different depths outside the church of Santa Maria.

anomalies are visible. The anomalies farthest from the wall of the church are at least partially ascribable to tombs; indeed, it is known that there was a cemetery in that area. Some clear anomalies close to the walls of the church are outlined by the ellipsis superimposed to the slice at 10 ns and by the circle superimposed to the slice at 15 ns; they might be related to the structural problems that the building is having.

Three B-Scans were recorded along the sidewalk that runs around the church structure, in order to gather some data very close to the building. The location of the B-Scans is shown in Figure 22, whereas the results are shown in Figure 23. Looking at Figure 23, we see in B-Scan No. 1 a rather clear discontinuity, suggesting the presence of a two-layered soil in the first part of the profile. The time depth of this interface oscillates slowly around 15 ns (about 75 cm). Several stronger reflections are present in B-Scan No. 1, indicating maybe past works with heterogeneous materials used for the filling. Overall, the prospecting reveals clearly that the most inhomogeneous conformation is under the line of B-Scan No. 1.
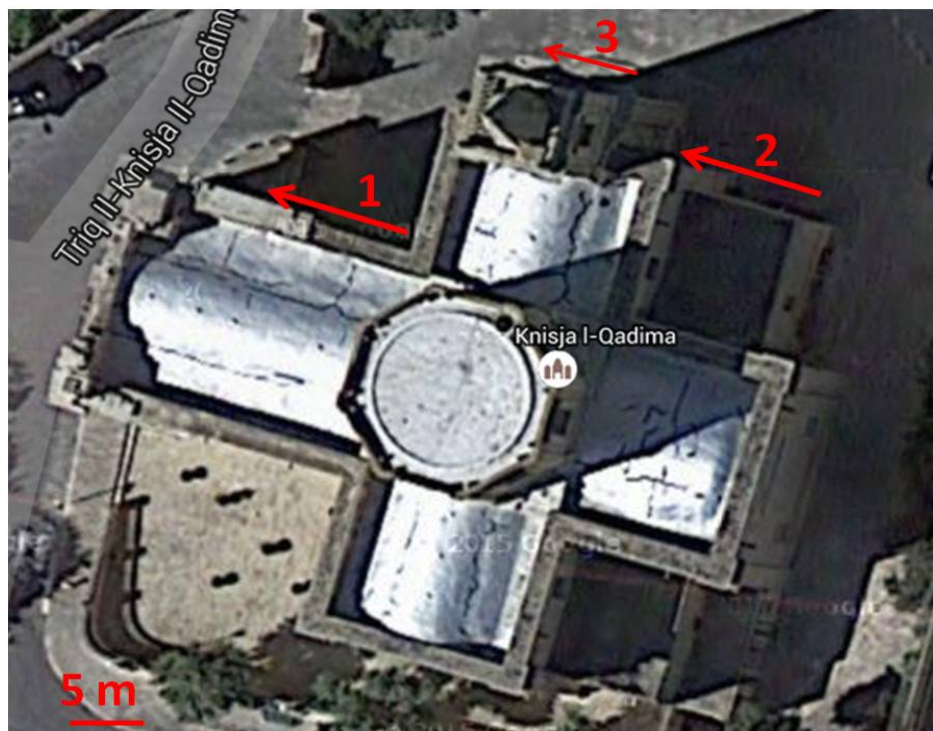
FIG. 22 – The displacement of three B-Scans gathered around the church of Santa Maria.
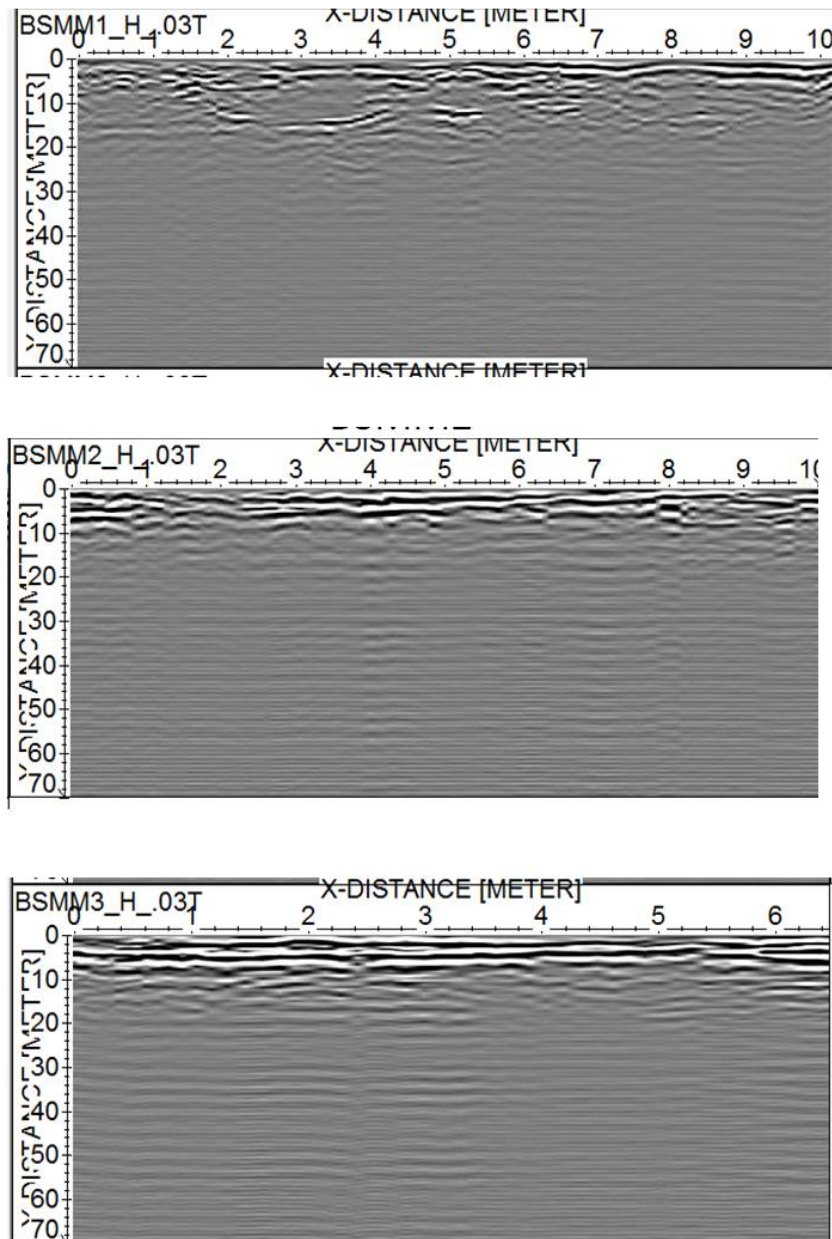
FIG. 23 – From top to bottom, the processed B-Scans No. 1, 2 and 3 as indicated in Fig. 17.

4.5. MEASUREMENTS IN THE CO-CATHEDRAL OF ST. JOHN, LA VALLETTA

Measurements were performed in the co-cathedral of St. John, which is an important monument, patrimony of UNESCO, with precious frescoes and paintings, as well as the tombs of many knifes of the order of Malta, including some Grand Masters of the knifes. Both GPR and passive

seismographic data were gathered in the co-cathedral. The obtained results are presented in this subsection of the paper.

With regard to the GPR data, a small rectangle evidenced in Figure 24 was prospected with interline spacing of 40 cm. Moreover, three B-Scans were recorded in the main nave, as shown in Figure 24.
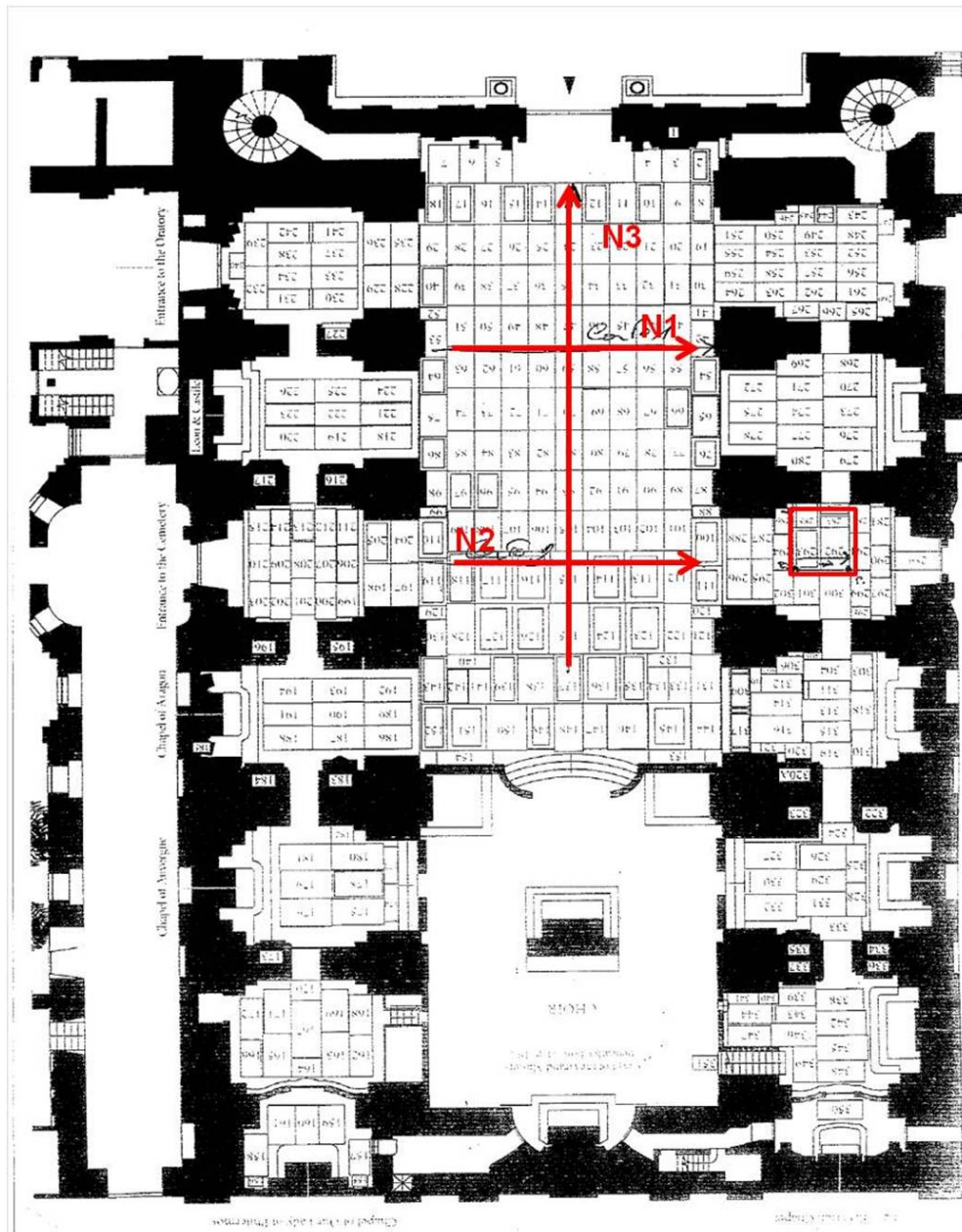
FIG. 24 – Map of the GPR prospecting in the co-cathedral of St. John.

The data gathered on the rectangle in the lateral chapel (where nowadays is the entrance for the tourists) were aimed to establish whether a crack on a gravestone on the floor is due to a void under it. In fact, the floor of the church is a sequence of gravestones, but not all of them really correspond to an underlying tomb. GPR data were therefore recorded on a small rectangle (2.4 m × 3.1 m) approximately centred on the crack. This time, the high frequency antennas were exploited, as the crack was likely to be related to a possible cause buried in the first meter at most. The obtained results are reported in Figure 25 and reveal the presence of superficial inhomogeneous features, no meaningful cavities are seen. This suggests that the causes of the crack must be superficial.
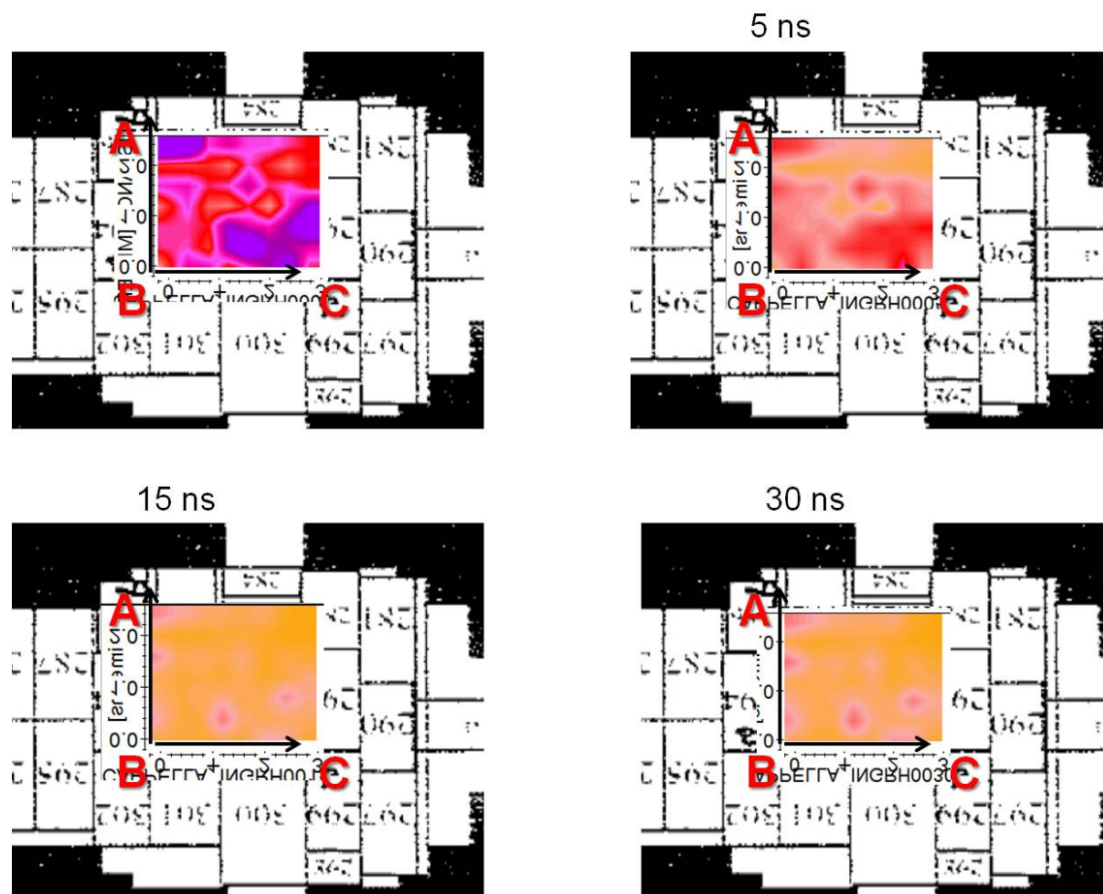
FIG. 25 – Horizontal slices in the entrance chapel of the co-cathedral of St. John. For time depth conversion: the upper left slice is quite superficial (about 5 cm - 7 cm), 5 ns correspond to about 25 cm, 15 ns correspond to about 75 cm, and 30 ns correspond to about 150 cm.

When present, shallow cavities are usually well visible, as can be appreciated from the results recorded in the nave of the church and presented in Figure 26. In general, single B-Scans are not sufficient to foresee the presence and position of tombs (horizontal slices are well advised for that). However, in the case at hand the presence of tombs is revealed in the areas where several multiple reflections occur: such reflections are well visible in several points of the B-Scans, and are particularly evident in the longitudinal B-scan No. 3, probably because this one crosses some tombs along their long side.

B-Scan No. 1

B-Scan No. 2

B-Scan N0. 3
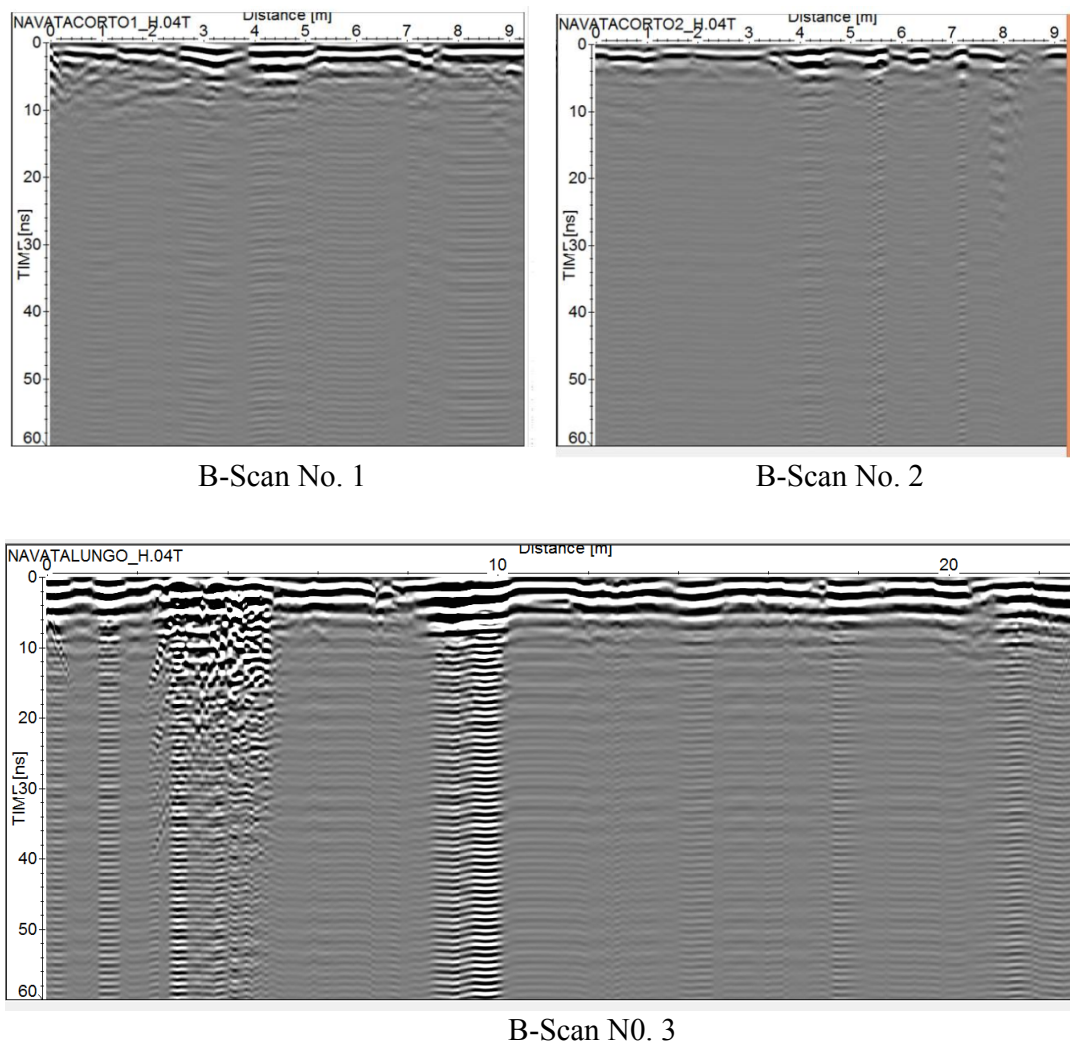
FIG. 26 – B-Scans gathered in the main nave of the co-cathedral of St John.

4.6.   TESTING THE RECONFIGURATION OF INTEGRATION TIMES

As mentioned in Section 2, the stepped-frequency GPR prototype allows gathering data with three couples of antennas and reconfiguring the integration times of the transmitted and received harmonic tones.

In the framework of the investigations presented in this paper, in some cases the most useful data were recorded by the low-frequency antennas (e.g., at Golden Bay), in some other cases the most interesting data were gathered by the medium-frequency antennas (e.g., Laferla Cross, Madliena tower, Santa Maria church), and we exploited the high-frequency data for the study carried out in the co-cathedral of St. John. Our system gathered three sets of data in each site, and so, for further possible analyses, we have at our disposal other data, beyond those reported and interpreted in the previous sub-sections of the paper.

The reconfiguration of the integration times was performed everywhere, apart for Golden Bay, due to technical problems that could be solved only after that (first) prospecting. So, the data of Laferla cross, Madliena tower, Santa Maria church and St. John co-cathedral have been gathered after a reconfiguration of the integration times. We will show here how the system is able to recognize the interferences, according to the algorithm described in Section 2, and how the data look slightly cleaner – in a couple of cases – after the reconfiguration of the integration times. The effects of the interferences are not strong in the cases at hand, both because there was no strong source of interference close to the investigated areas, and because the prototype uses default integration times quite longer than those of commercial systems.

In Figure 27 we show the variance of the tones (see Section 2) for data recorded at Laferla Cross and Madliena tower. As can be noticed, in both cases the most disturbed frequencies are in the lower part of the 50–1000 MHz range. This happens most times, first of all because FM broadcast transmissions usually occupy the band around 100 MHz, and also because the GPR antenna shielding is customarily less efficient at low frequency. We observe that the variance level measured at Laferla cross is much higher (3 orders of magnitude) than that gathered inside Madliena tower. This is coherent with the fact that Madliena tower is a historical building with rather thick walls, which isolate the internal room from the external environment, whereas Laferla Cross is an outdoor site.
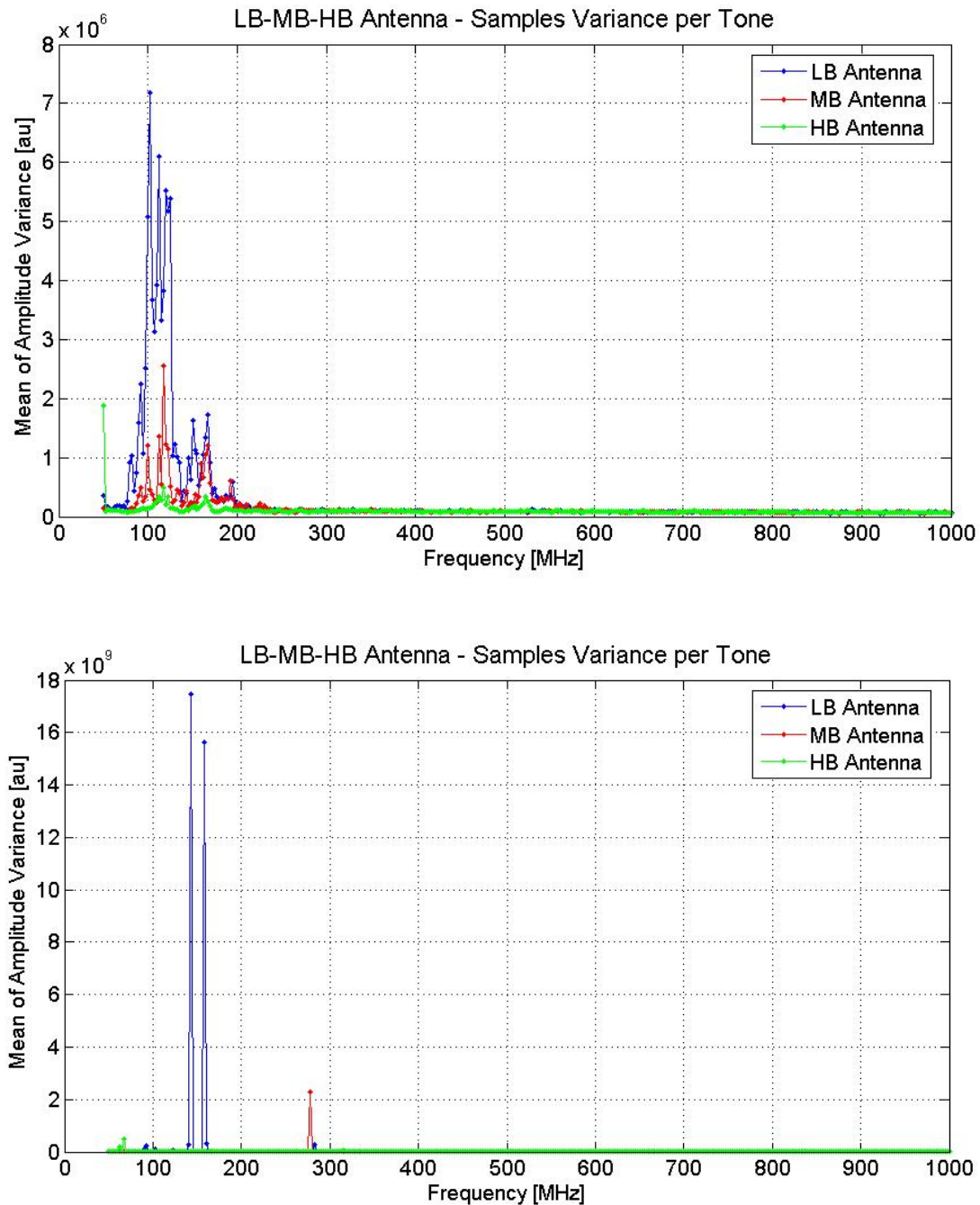
FIG. 27 – The variance of the tones in the site of Laferla Cross (upper panel) and in the site of the Madliena tower (lower panel).

In Figure 28, the variance of tones for two scans gathered outside the church of Santa Maria is shown. We recorded two calibration B-Scans to check whether the graph of the variance of the tones was strongly

dependent on the position of the B-Scan; the two B-Scans were at about 20 m of distance from each other and not parallel to each other, moreover they were on two different sides of the building. As can be seen, the results are not the same, and indeed the level of the disturbance changes of one order of magnitude, but the most disturbed frequencies are the same. In particular, in both cases there is a peak around 100 MHz and another one around 200 MHz We were then informed that there is a radio station near the church, transmitting with a carrier of 99 MHz, which explains the peaks. Apart from this, the measurements prove the reliability of the method, because the most disturbed frequencies are essentially related to the area and not to the particular B-Scan.

In Figure 29, the variance of the tones recorded in the co-cathedral of St. John is shown. We first measured the variance shown in the upper panel of the figure; then, we saw the transceiver devices used by the staff of the co-cathedral (which nowadays is also a museums) and we gathered a second calibration, along the same measurement line and after switching on a transceiver. The carrier of the transceiver is at 446 MHz, and coherently, a localized disturbance is visible at this frequency in the lower panel of Figure 29. We can see that the disturbance due to the transceiver is at a much higher level than the previously recorded one, which was, instead, of the same level as the disturbance recorded in the Madliena tower (also in this case, in fact, we were indoor, in a historical building with thick and partially isolating walls). We decided to calibrate the reconfiguration of the GPR on the basis of the possible interferences from the transceivers. In the previous case studies, we set $F = 10$ for the low and the medium frequency antennas in the sites of Laferla, Madliena tower and Santa Maria church, and we used $F = 1$ for the high frequency antennas in those cases. In the co-cathedral, instead, we set $F = 10$ for all the antennas. The prolongation factor of the integration time for each tone is shown in Figure 30.

In Figure 31, the same observation line was walked through two times, without and with reconfiguration, in the site of Laferla. Analogous results are shown in Figure 32 for the site of Madliena tower and in Figure 33 for the site of Santa Maria church. Finally, the same comparison was performed in the co-cathedral of St. John and relevant results are presented in Figure 34. We notice some effects of the reconfiguration in the sites of Laferla and St. John, whereas in the sites
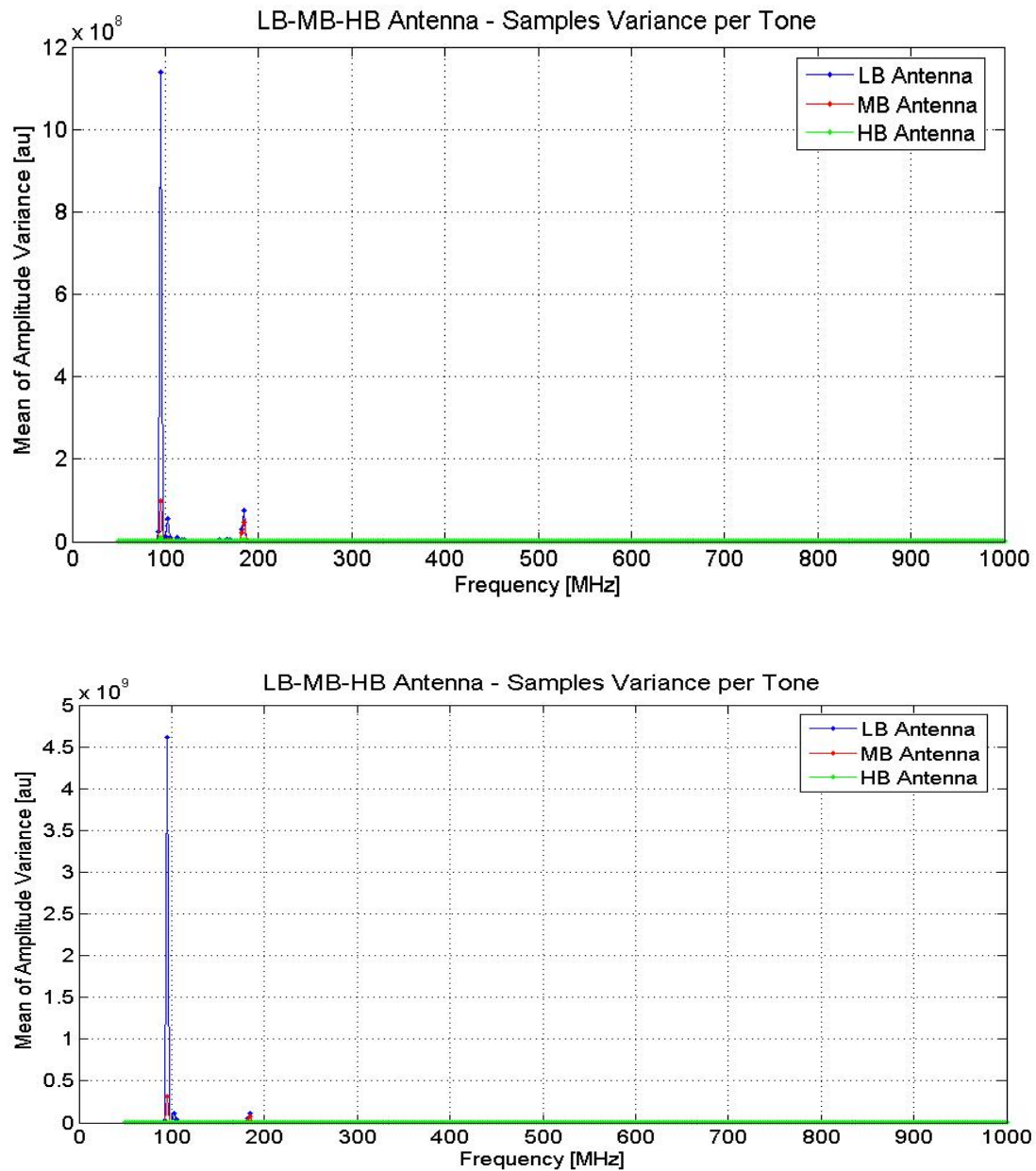
FIG. 28 – Variance of the tones measured along two B-Scans outside the church of Santa Maria.

of Santa Maria and Madliena Tower, the effects are not appreciable on the shown scale. With regard to the site of Madliena tower, this is easily understood because of the isolating walls. Outside Santa Maria church, there was a stronger interference than inside Madilena tower, but this mostly regarded the low frequency antennas, whereas we are now

analysing at medium-frequency antenna results. In particular, if we have another look at the curves shown in Figures 27 and 28, we can appreciate that the level of interference was in any case weaker at Santa Maria church than at Laferla, and also that the level of interference at Santa Maria church was stronger for the low-frequency antennas, whereas the variance of the tones of the medium-frequency antennas has an appreciable peak at about 290 MHz in the site of Laferla.

5.   CONCLUSIONS

In this report we have presented the main results achieved during the Short-Term Scientific Mission (STMS) entitled "Use of GPR and standard geophysical methods to explore the subsurface," funded by COST Action TU1208. We performed measurements in various sites of geological and/or cultural interest in the island of Malta.

Integrated Ground Penetrating Radar (GPR) and passive seismic surveys were carried out. The reconfiguration of the integration times of the harmonic components, an advanced feature recently implemented in a stepped-frequency GPR prototype, was tested on field data. With regard to this last point, the work is in progress and further tests will be done in the future to optimize and thoroughly characterize the performance of the system and the effectiveness of the reconfiguration of the integration times.

Let us underline that the reconfiguration of the integration times is a totally new feature of our GPR system. The algorithm for setting the reconfiguration on the basis of data gathered in the field is specifically related to an upgrade of the system, which was possible thanks to previous studies performed during the STMS carried out by Dr. Loredana Matera in Trondheim (Norway) in June 2014 [2]. That STSM was also funded by COST Action TU1208 and was hosted at the headquarters of 3d-radar, a well-known manufacturer of commercial stepped frequency systems.

We also wish to mention that the fruitful cooperation between IBAM-CNR and the University of Malta started thanks to the COST Action TU1208, with the STSM presented in this paper. We subsequently had the opportunity to strengthen our cooperation by organizing together an international training school, still funded by TU1208, held in Malta in January 2016. We then worked together again during a second TU1208

STSM, in March 2017 [20, 21]. The two institutions are now planning to present a project proposal together, in the framework of bilateral bands explicitly dedicated to Italian-Maltese collaborations.
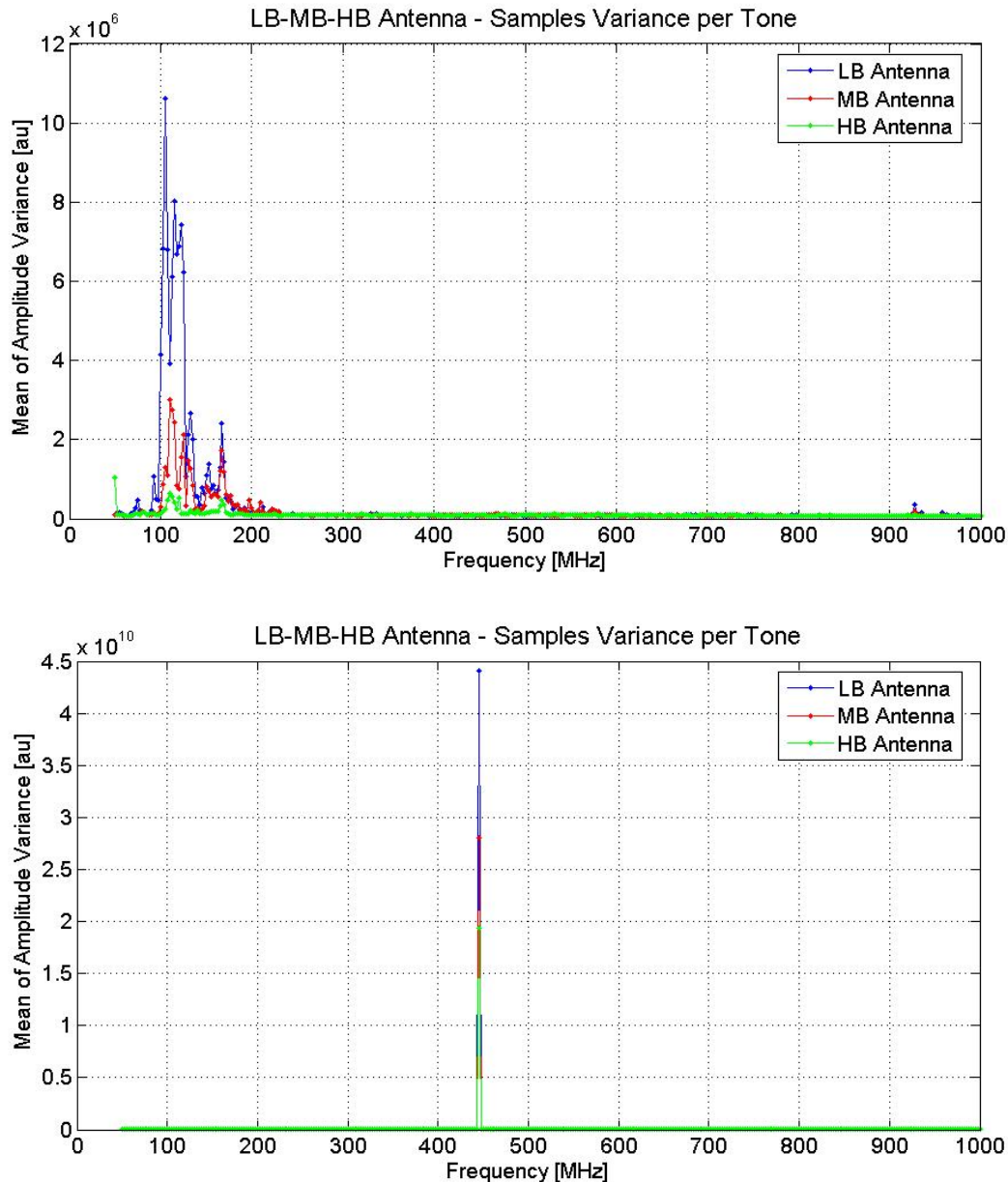
FIG. 24 – Variance of the tones in St. John co-cathedral. Upper panel: interferences gathered with the transceivers of the staff switched off. Lower panel: interferences gathered with the transceivers switched on.

Laferla

Madliena tower

Santa Maria church

St John co-cathedral
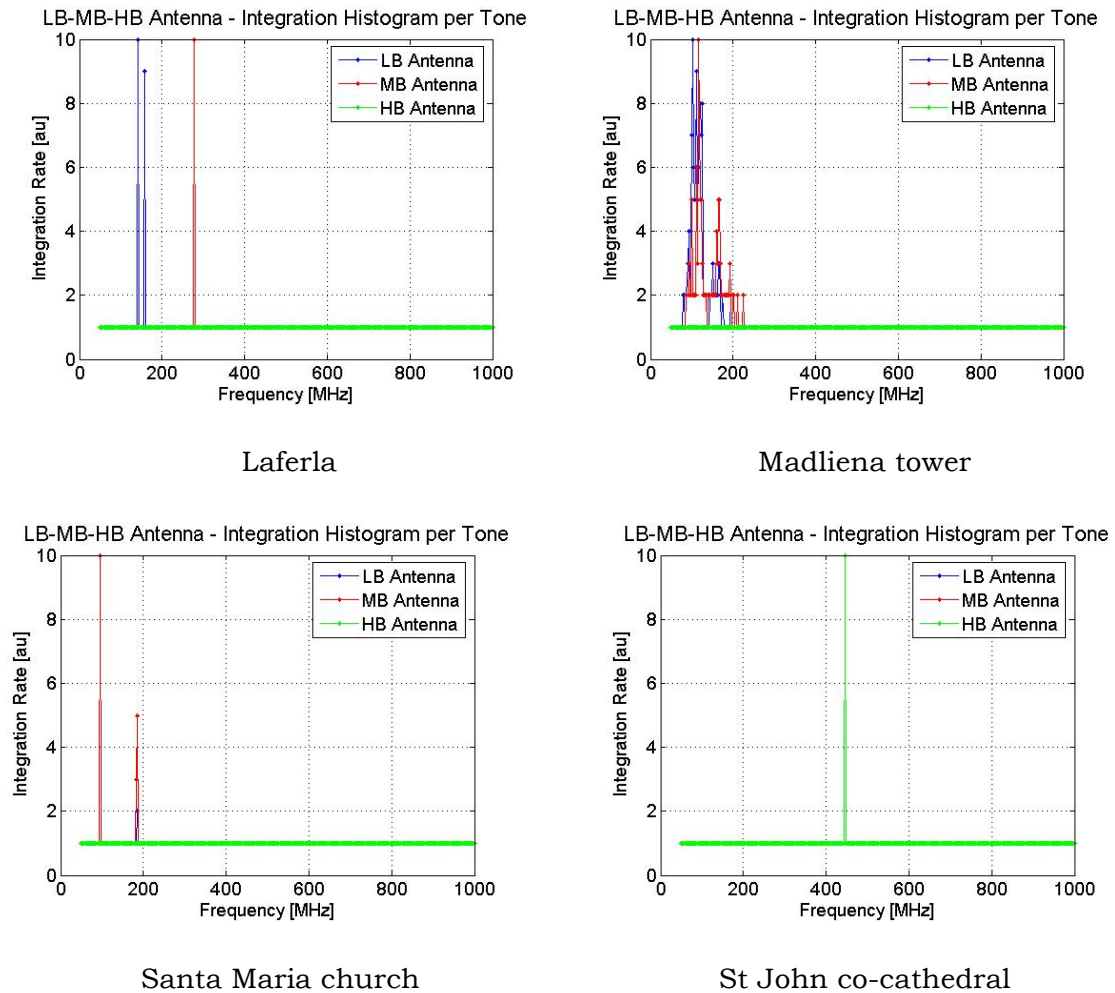
FIG. 30 – Prolongation of the integration times for each couple of antennas and for each investigated site.

ACKNOWLEDGEMENTS
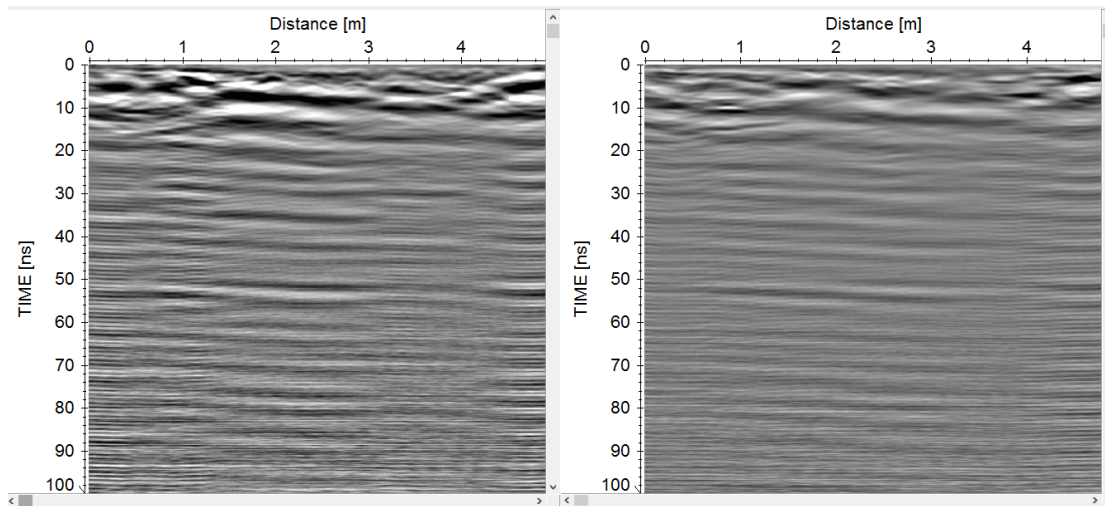
FIG. 31 – Non-reconfigured (left hand side) and reconfigured (right hand side) B-scan. Site of Laferla Cross.
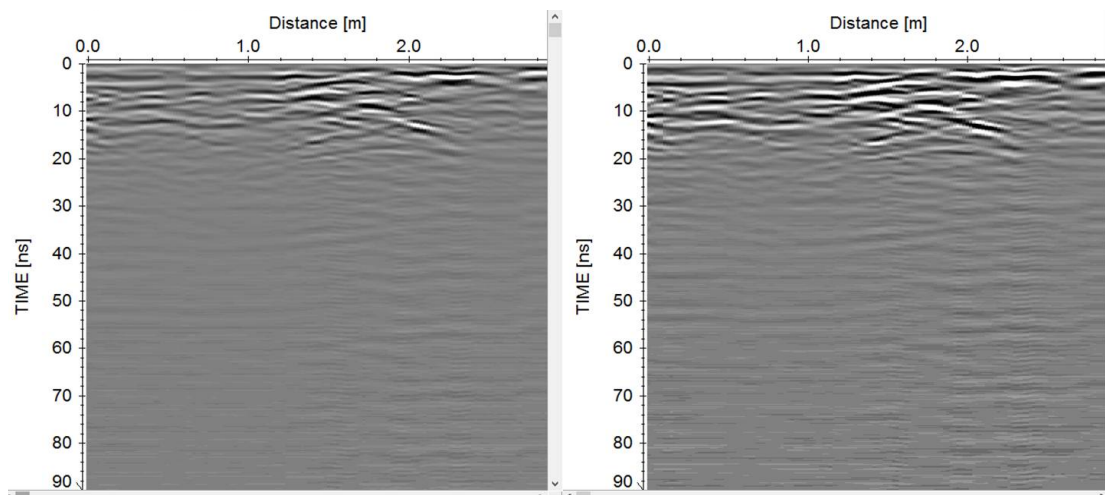
FIG. 32 – Nonreconfigured (left hand side) and reconfigured (right hand side) Bscan. Site of Madliena Tower.

REFERENCES

[1]   R. Persico and G. Prisco, "A Reconfigurative Approach for SF-GPR Prospecting," IEEE Transactions on Antennas and Propagation, vol. 56, n.8, pp. 2673–2680, 2008.

[2]   L. Matera and J. Sala, "Tests, comparison and improvement plans for an innovative reconfigurable stepped-frequency GPR," book chapter in Short-Term Scientific Missions - Year 2, L. Pajewski and M. Marciniak, Eds.; Publishing House: Aracne; Rome, Italy, May 2015; ISBN 978-88-548-8488-5.
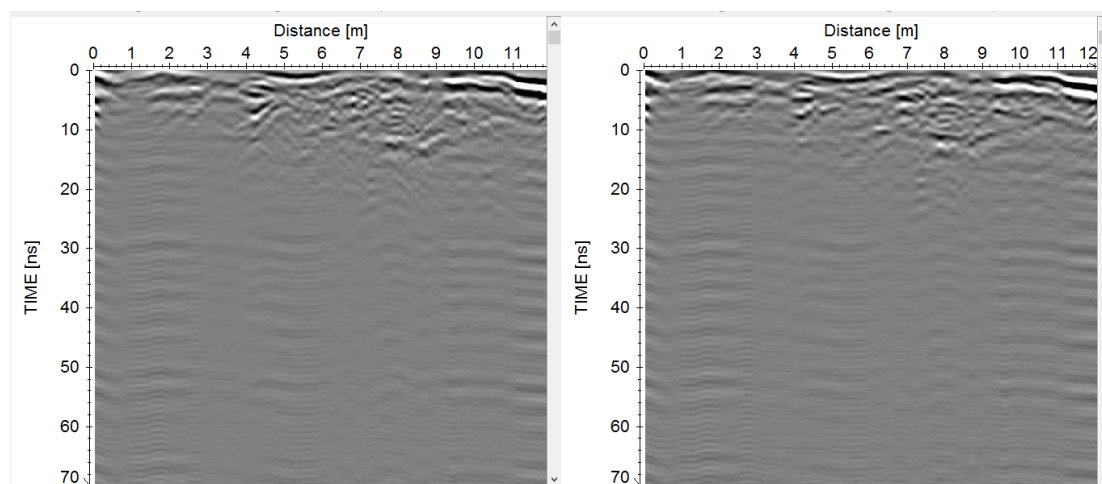
FIG. 33 – Non-reconfigured (left hand side) and reconfigured (right hand side) B-scan. Site of Santa Maria Church.
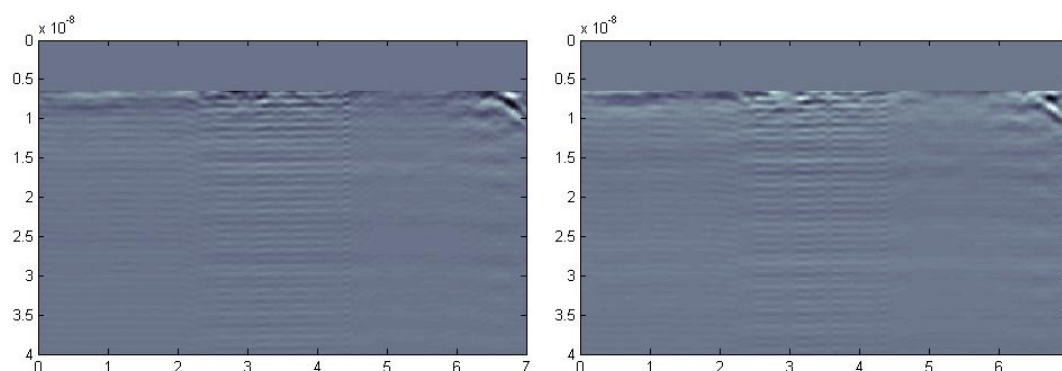
FIG. 34 – Non-reconfigured (left hand side) and reconfigured (right hand side) B-scan. Site of the co-cathedral of St. John.

[3]   R. Persico, M. Ciminale, and L. Matera, "A new reconfigurable stepped frequency GPR system, possibilities and issues; applications to two different Cultural Heritage Resources," Near Surface Geophysics, vol. 12, pp. 793–801, 2014.

[4]   P. Y. Bard, "Guidelines for the implementation of the H/V spectral ratio technique on ambient vibrations: measurements, processing, and interpretations," SESAME European Research Project, WP12, deliverable D23.12, 2004, available at sesame-fp5.obs.ujf-grenoble.fr/Deliverables2004.

[5]   M. Nogoshi and T. Igarashi, "On the amplitude characteristics of microtremor (part 2)," Journal of Seismology of the Society of Japan, vol. 24, pp. 26–40, 1971.

[6]   Y. Nakamura, "A method for dynamic characteristics estimation of subsurface using microtremor on the ground surface," Quarterly Report of Railway Technical Research Institute (RTRI), vol. 30(1), pp. 25–33, 1989.

[7]   S. Bonnefoy-Claudet, F. Cotton, and P. Y. Bard, "The nature of noise wavefield and its applications for site effects studies: a literature review," Earth-Sci. Rev., vol. 79(3), pp. 205–227, 2006.

[8]   H. M. Pedley, M. R. House, and B. Waugh, "The geology of Malta and Gozo. Proceedings of the Geologists' Association," vol. 87, pp. 325–341, 1976.

[9]   M. Pedley, M. Hughes-Clarke, and P. Galea, P., "Limestone Isles in a Crystal Sea — The Geology of the Maltese Islands," Publishers Enterprises Group Ltd, San Gwann, Malta, 2002.

[10]   P. Galea, S. D'Amico, and D. Farrugia, "Dynamic characteristics of an active coastal spreading area using ambient noise measurements (Anchor Bay, Malta)," Geophysical Journal International, vol. 199, pp. 1166–1175, 2014.

[11]   F. Panzera, S. D'Amico, A. Lotteri, P. Galea, and G. Lombardo, "Seismic site responce of unstable steep slope using noise measurements: the case study of Xemxija bay area, Malta," Natural Hazard and Earth System Science, vol. 12, pp. 3421–3431, 2012.

[12]   G. Gigli, W. Frodella, F. Mugnai, D. Tapete, F. Cigna, R. Fanti, and L. Lombardi, "Instability mechanisms affecting cultural heritage sites in the Maltese Archipelago," Natural Hazards and Earth System Science, vol. 12, pp. 1883–1903, 2012.

[13]   F. Panzera, S. D'Amico, P. Galea, G. Lombardo, M.R. Gallipoli, and S. Pace, "Geophysical measurements for site response investigation: preliminary results on the island of Malta," Bollettino di Geofisica Teorica ed Applicata, vol. 54(2), pp. 111–128, 2013.

[14]   A. Vella, P. Galea, and S. D'Amico, "Site frequency response characterisation of the Maltese islands based on ambient noise H/V ratios," Engineering Geology, vol. 163, pp. 89–100, 2013.

[15]   R. Persico, Introduction to Ground Penetrating Radar, Inverse Scattering and Data Processing, Wiley, 2014.

[16]   K. J. Sandmeier, Reflexw 3.0 manual - Sandmeier Software, Karlsruhe, Germany, 2003.

[17]   F. Soldovieri, G. Prisco, and R. Persico, "Application of Microwave Tomography in Hydrogeophysics: some examples," Vadose Zone Journal, vol. 7(1), pp. 160–170, 2008.

[18]   L. Mertens, R. Persico, L. Matera, and S. Lambot, "Smart automated detection of reflection hyperbolas in complex GPR images with no a-priori knowledge on the medium," IEEE Transctions on Geoscience and Remote Sensing, vol. 54(1), pp. 580–596, 2016.

[19]   N. Masini, R. Persico, E. Rizzo, A. Calia, M.T. Giannotta, G. Quarta, and A. Pagliuca, "Integrated Techniques for Analysis and Monitoring of Historical Monuments: the case of S.Giovanni al Sepolcro in Brindisi (Southern Italy)," Near Surface Geophysics, vol. 8(5), pp. 423–432, 2010.

[20]   R. Persico, S. D'Amico, E. Rizzo, L. Capozzoli, and A. Micallef, "Ground Penetrating Radar investigations in sites of cultural interest in Malta," Ground Penetrating Radar, vol. 1(1), pp. 38–62, 2018.

[21]   R. Persico, S. D'Amico, E. Rizzo, L. Capozzoli, and A. Micallef, "Electrical resistivity tomography investigations in Mgarr (Malta)," Ground Penetrating Radar, vol. 1(1), pp. 63–74, 2018.

Ground Penetrating Radar investigations in sites of cultural interest in Malta

Raffaele Persico[1], Sebastiano D'Amico[2], Enzo Rizzo[3],
Luigi Capozzoli[3] & Aaron Micallef[2]

[1] Institute for Archaeological and Monumental Heritage of the National Research
Council (IBAM-CNR), Lecce, Italy
R.PERSICO@IBAM.CNR.IT

[2] University of Malta, Faculty of Science, Msida, Malta
SEBASTIANO.DAMICO@UM.EDU.MT, AARON.MICALLEF@UM.EDU.MT

[3] Institute of Methodologies for Environmental Analysis of the National Research
Council (CNR-IMAA), Tito Scalo – Potenza, Italy
ENZO.RIZZO@IMAA.CNR.IT, LUIGI.CAPOZZOLI@IMAA.CNR.IT

Abstract

This paper presents the results of a series of geophysical surveys carried out in Malta. In particular, we used a reconfigurable stepped-frequency Ground Penetrating Radar (GPR) prototype to inspect the Argotti Garden in Floriana, looking for ancient buried cisterns, and the floor of the Nymphaeum inside the garden, to assess its conditions prior to restoration works. We subsequently used a commercial pulsed GPR system to assess the walls of the co-cathedral of St. John, in Valletta, and the walls of a building of the University of Malta, in Msida. All measurements were performed during a Short-Term Scientific Mission (STSM) funded by the COST (European Cooperation in Science and Technology) Action TU1208 "Civil engineering applications of Ground Penetrating Radar." Of course the work performed during the STSM consisted also in the processing and interpretation of the gathered data.

Keywords: Ground Penetrating Radar; Cultural heritage; Detection of buried structures; Inspection of walls; Estimation of propagation velocity and relative permittivity.

1. Introduction

A Short-Term Scientific-Mission (STMS) entitled "Integrated geophysical investigations of sites of cultural interest in Malta" was recently funded by COST (European Cooperation in Science and Technology), in the framework of the COST Action TU1208 "Civil engineering applications of

Ground Penetrating Radar." Raffaele Persico, Luigi Capozzoli and Enzo Rizzo visited Sebastiano D'Amico and Aaron Micallef in Malta, from March 5th to March 18th, 2017, and they jointly investigated a series of sites of cultural interest.

The initial plan was to survey the following archaeological and historical sites: the Argotti Botanical Garden in Floriana and the Nymphaeum inside the garden, the co-cathedral of St. John in Valletta, and the Palace de la Salle, still in Valletta. In the latter site, the degradation of frescoes did not allow performing the scheduled investigations. Some results obtained in the co-cathedral of St John, where a few walls were investigated, looked rather obscure and difficult to be interpreted; for comparison purposes, further tests were performed on similar walls in the University of Malta, in Msida. The walls of the co-cathedral and those of the university building were both nominally made of globigerina. Therefore, although we could not perform the planned measurements in the Palace de la Salle, we dealt with the inspection of the walls in the university, which was not initially scheduled, and the total number of case studies did not change. In this paper, all results obtained during the STSM are presented. The work performed during the STSM consisted also in the processing of the recorded data and their interpretation.

In the Argotti Botanical Garden (Section 2), four Ground Penetrating Radar (GPR) profiles (B-Scans) were collected by using a stepped-frequency reconfigurable GPR prototype. Additionally, we processed and interpreted some data previously gathered in the same garden, by a different team, by using a commercial pulsed GPR system. In the Nymphaeum and its surroundings (Section 3), a grid of short GPR profiles was acquired by using the stepped-frequency reconfigurable GPR prototype.

We collected five GPR profiles on the walls of the co-cathedral of St. John in Valletta (Section 4) and sixteen GPR profiles on the walls of the University of Malta, in Msida (Section 5).

2. THE ARGOTTI BOTANICAL GARDEN IN FLORIANA

The Argotti Botanical Garden of Malta has an historical relevance. It is found in an area where the Knives constructed large cisterns for gathering the water for the needs of the island (in particular for Valletta

and for the settlements around Valletta). Some of these cisterns are visible and we have seen one of them in the Botanical Garden; it is deemed that other cisterns are present in the garden. The cisterns are expected to expand at a depth of 5 to 6 meters, where they become hundredths cube meter large, as big demijohns. In order to identify them, we exploited a stepped frequency reconfigurable ground penetrating radar, initially designed and realized within the project AITECH (http://www.aitechnet.com/ibam.html), funded by the Puglia Region, and more recently improved in the framework of the COST Action TU1208. We gathered four B-Scans in the Botanical Gardens, looking for the cisterns, as shown in Figure 1.
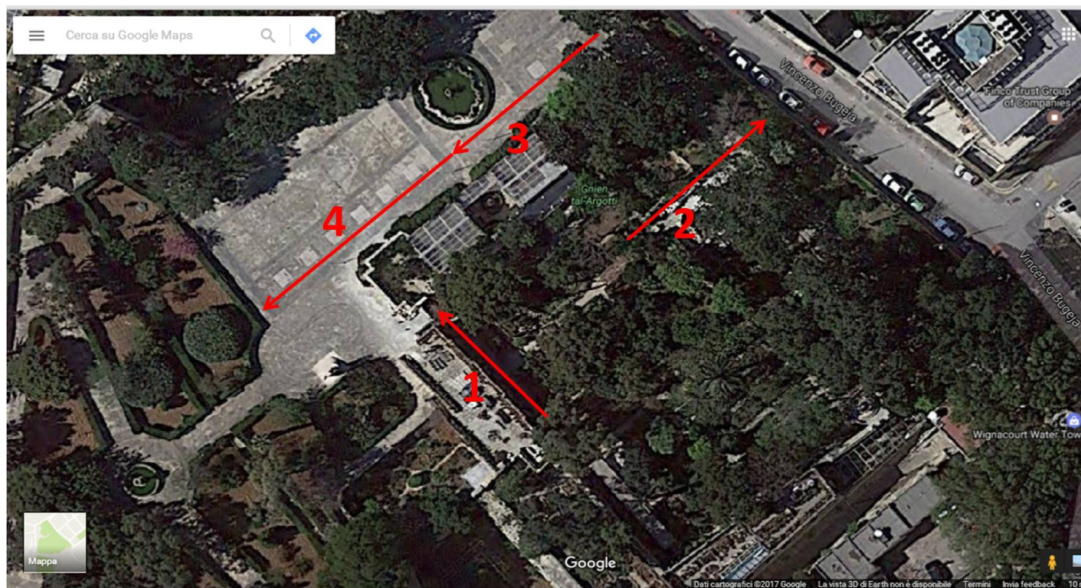
FIG. 1 - Map of the B-Scans gathered in the Argotti Garden.

The B-Scans were labelled as BScan1, BScan2, BScan3 and BScan4. The presence of plants in the garden prevented from prospecting more completely the area. To be precise, BScan3 and BScan4 were gathered outside the garden, where a large area was available; unfortunately we did not have the permissions for acquiring more data and for prospecting the entire area.

As a preliminary step, we repeated BScan1 twice, in order to check whether there was a meaningful electromagnetic interference. This task was possible thanks to some advanced features recently implemented in

the reconfigurable GPR. We do not describe in detail the exploited algorithm, because this was developed during a previous STSM: for more information please see [1-3]. Here, we just wish to say that the data showed no significant interference problems in the cases at hand.

All data presented in Figures 2-4 were recorded by the low frequency antennas of the reconfigurable GPR, with a central frequency of about 120 MHz: the targets of interest, in the case at hand, were large and possibly quite deep; therefore, this band was the most promising one.

The data processing included: zero timing, background removal, gain application versus depth, a slight one-dimensional filtering, and visualization of the first 50 ns of the signal. Then, the data were migrated.

The most interesting anomalies in Figures 2 to 5 are circled in red. We did not identify clear traces of possible buried cisterns.
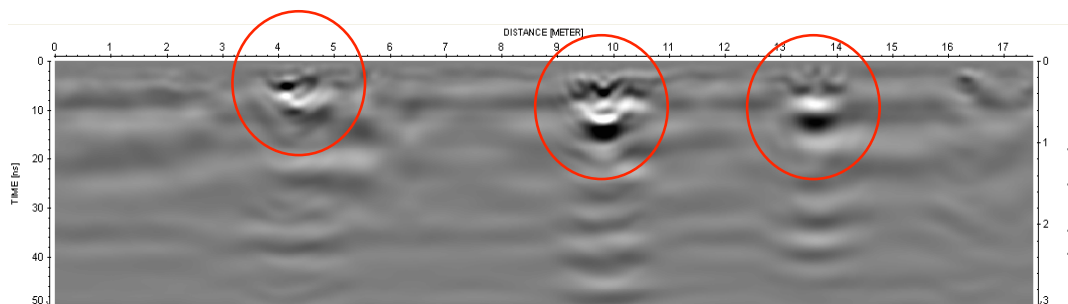
FIG. 2 - Elaboration of BScan1.

What a GPR can probably see is the upper part of a cistern, closer to the mouth, or closer to a point that used to be the mouth. Anomalies ascribable to cisterns would probably appear rather small, compared to the cistern size. This is because the bottom of the cistern is too far and consequently the radiated energy is lost in scattering phenomena. Moreover, we cannot exclude the possibility that some cisterns could be partially filled up with loose materials. In that case, we would not have a buried empty cavity as large as the cistern used to be at the time of the Knives.

Further to gather our own data, we had at our disposal some data previously gathered by a local company by using a commercial GPR system manufactured by MALÅ equipped with a 150 MHz antenna. We did not have more information about their data. In particular, we did

not know the precise localization of the B-Scans, although we knew that they were collected in the same area as our B-Scans 3 and 4 (Figure 1). The processing of the data was similar to that preformed for our data, with some different specific data (and antenna) driven parameters. The results are presented in Figures 6 to 9.

Also in the data collected by the company, a direct evidence of the cisterns cannot be found. Some superficial anomalies are hardly visible, indicated by red arrows. It is evident that a strong phenomenon of antenna ringing occurred and the quality of the images is lower.
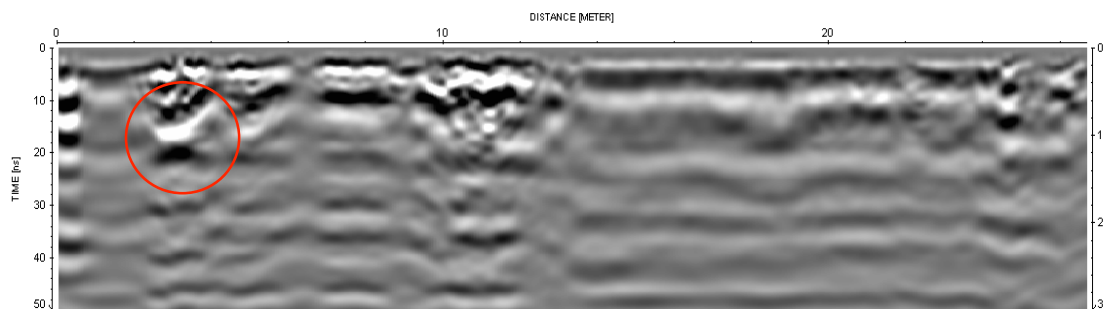
FIG. 3 - Elaboration of BScan2.
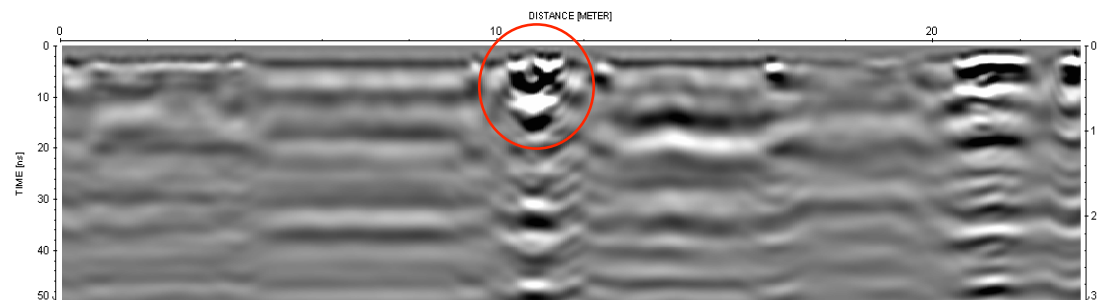
FIG. 4 - Elaboration of BScan3.
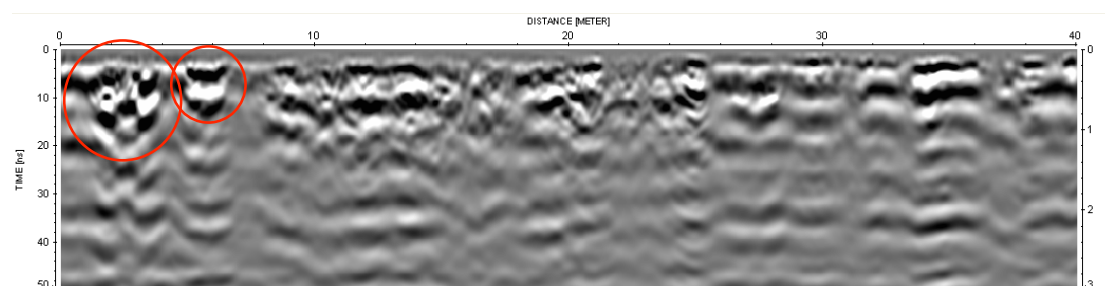
FIG. 5 - Elaboration of BScan4.
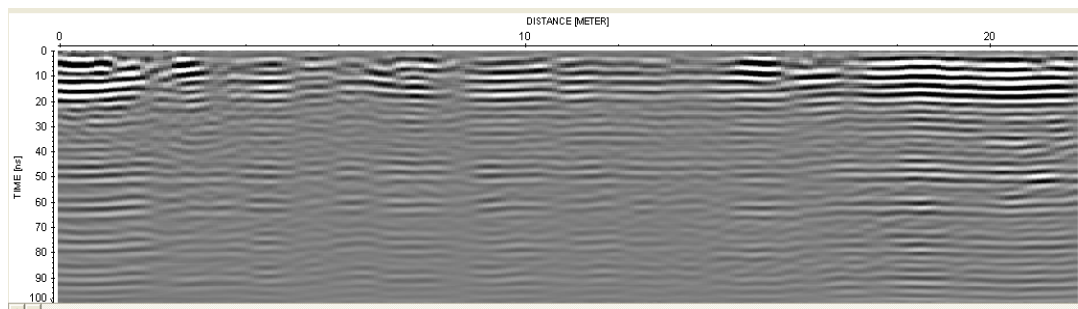
FIG. 6 - First B-Scan gathered with a commercial system.
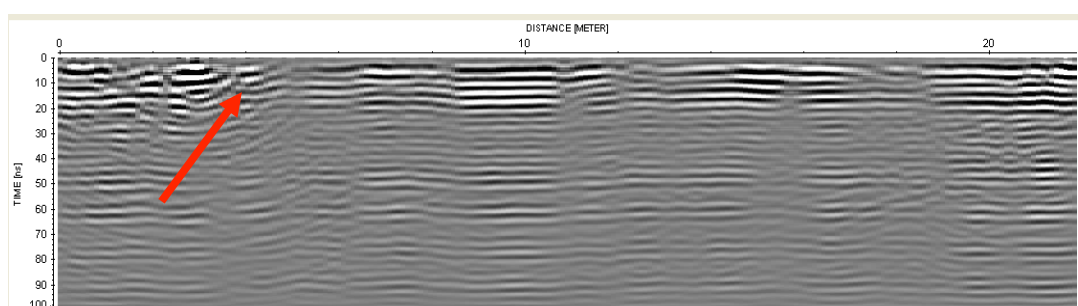
FIG. 7 - Second B-Scan gathered with a commercial system.
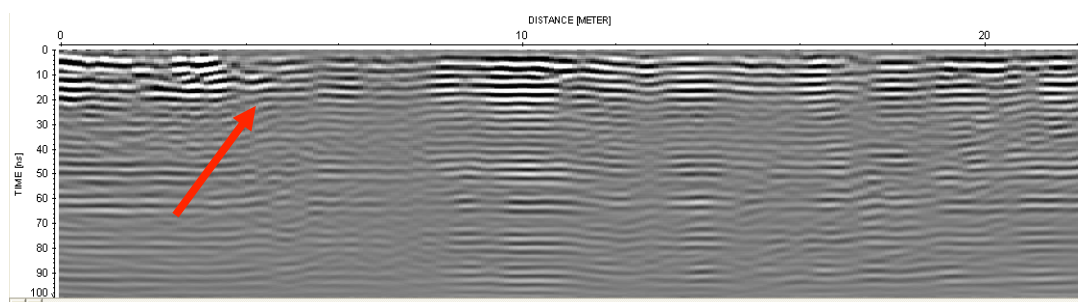
FIG. 8 - Third B-Scan gathered with a commercial system.
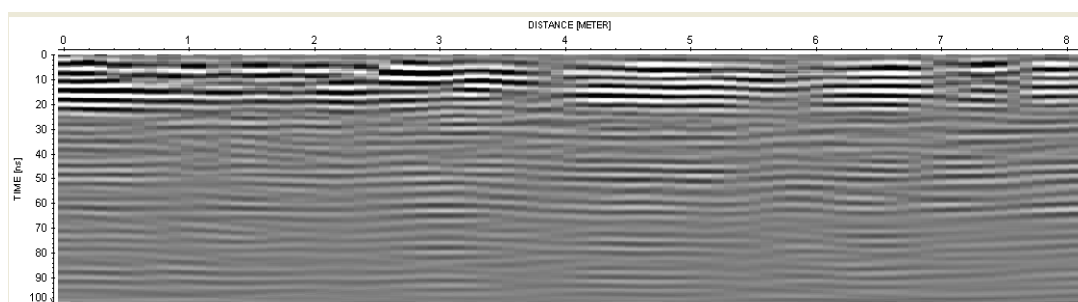
FIG. 9 - Fourth B-Scan gathered with a commercial system.

The problem of finding the cisterns is of interest for the local cultural authorities. As a conclusion of our preliminary study, we communicated them that an integrated prospecting could help to achieve more information about the subsurface and the presence of cisterns. In particular, permission for gathering a sufficient number of GPR profiles in the area adjacent to the gardens is necessary, in particular we need to acquire a grid of profiles in order to realize horizontal images of the ground, at different depths (slices). This will help to discriminate if some anomalies can be ascribable to the top of cisterns. Moreover, and above all, a three dimensional geoelectrical prospecting would be more suitable for this kind of investigation than a GPR survey, given the depth and strong resistivity of the anomalies looked for (if big cavities were present). Last but not least, the geoelectrical prospecting should be slightly invasive, in the sense that the electrodes should be knocked beyond the asphalt layer, which therefore should be removed in some (very small) regions and then restored after the investigation. Non-invasive electrodes exist, which can be placed over the surface, however in this case they would not work because the asphalt is electrically insulating.

3.   THE NYMPHAEUM OF THE ARGOTTI BOTANICAL GARDEN IN FLORIANA

Within the Argotti Garden there is a Nymphaeum of artistic and historical relevance. Nowadays, it is not perfectly preserved and needs restoration works. In order to perform in a safe way such works, and in particular in order to put the scaffoldings in a non-dangerous way (for the possible presence of cavities under the floor), it was of interest to perform a GPR prospecting. So, we gathered a grid of profiles within the Nymphaeum, by using our reconfigurable stepped-frequency GPR system. We also prospected part of the path that brings to the Nymphaeum. As the signal returned by the two areas was quite different, two different processing procedures were applied, in order to emphasize the internal and external anomalies.

The first processing, for data gathered inside the Nymphaeum, was composed by zero timing at 0.8 ns, background removal on all the traces, gain function with linear amplification factor equal to 1, exponential amplification factor equal to 2, and saturation at 10000. Then, a background filtering followed, with moving averaging on 26

traces. Finally, a Kirchhoff migration on 25 traces with a propagation velocity of 0.12 m/ns was performed.

After the processing, horizontal slices were retrieved. The profile spacing was 20 cm and high frequency antennas were used (their band overall covers the 500 MHz to 1000 MHz range), because this time we were looking for shallower and smaller targets. In Figures 10 to 14, some slices are shown relative to this processing, aimed to emphasize the anomalies below the floor of the Nymphaeum; the GPR data are superimposed to the map of the Nymphaeum (axes are in meters).

The more superficial slices tell us that the main anomalies are located in the part of the Nymphaeum closer to the entrance. Those anomalies might be due to previous foundations, else to a different composition or density of the subsoil. From the data, we excluded the presence of superficial cavities.
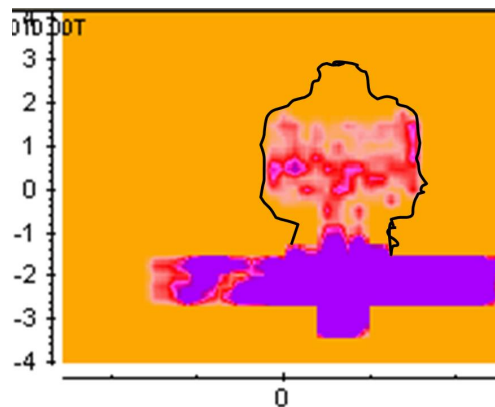
FIG. 10 - Slice at about 12 cm depth.
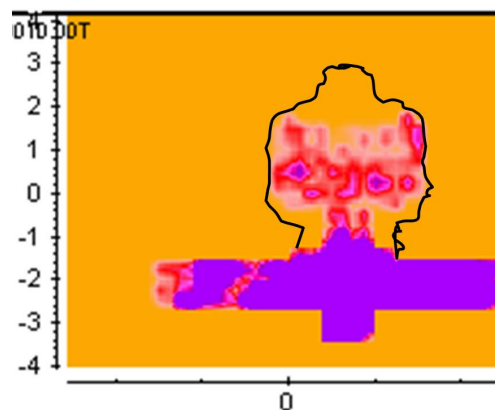
FIG. 11 - Slice at about 24 cm depth.
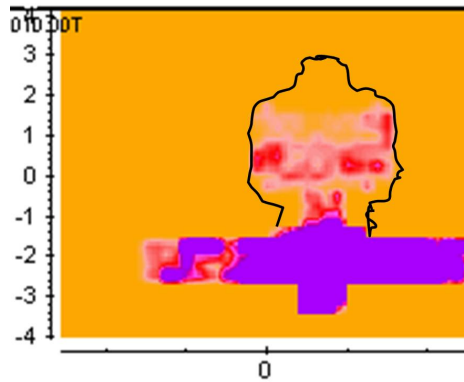
FIG. 12 - Slice at about 36 cm depth.
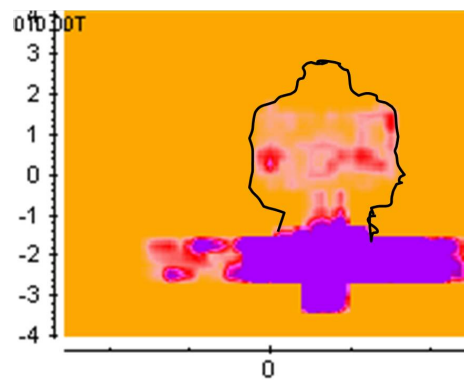
FIG. 13 - Slice at about 48 cm depth.
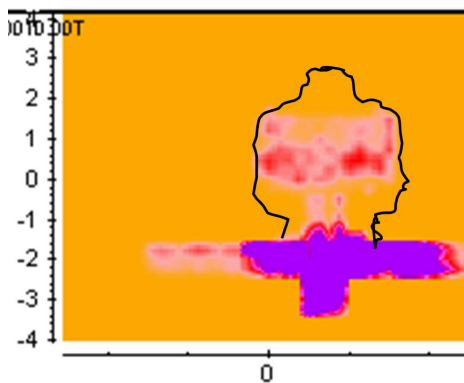
FIG. 14 - Slice at about 60 cm depth.

We tried a slightly different processing, to better emphasize the anomalies outside the Nymphaeum. The new processing was composed by a time cut at 70 ns, zero timing at -8 ns, background with running averaging on 51 traces, a gain function with parameters 1 and 1 for the linear and exponential amplification respectively, and with saturation at

10000. Then a Butterworth filter in the band 50-1000 MHz was applied and finally a Kirchoff migration on 17 traces with propagation velocity estimated equal to 0.09 m/ns. The results are presented in the slices of Figures 15 to 17.
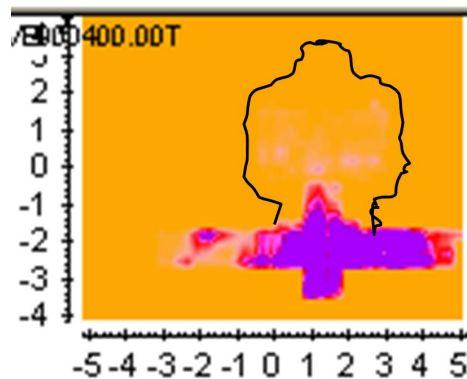
FIG. 15 - Slice at about 18 cm - second processing procedure.
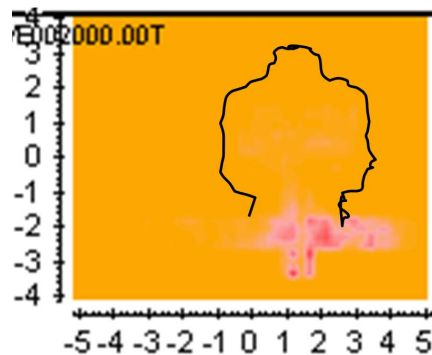
FIG. 16 - Slice at about 90 cm - second processing procedure.
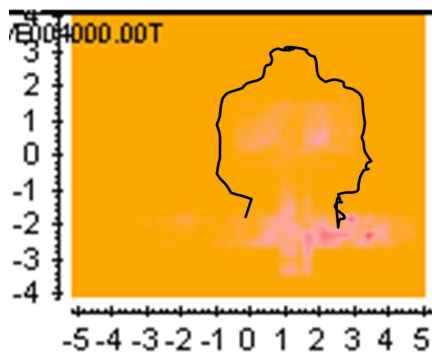
FIG. 17 - Slice at about 180 cm - second processing procedure.

Outside the Nymphaeum we did not identify any meaningful buried anomaly, we just observed very different reflection characteristics before the Nymphaeum and immediately after the entrance of the Nymphaeum. This suggests that the concrete path is made of different materials than the concrete floor in the Nymphaeum; quite probably it was realized in a different period. Alternatively, some works interested in the past only part of the path, thus causing the different electromagnetic response.

4.   WALLS OF THE CO-CATHEDRAL OF ST. JOHN IN VALLETTA

The co-cathedral of St. John is one of the most important monuments in Malta. This is the cathedral were the Grand Masters of Knives used to be buried. It is a masterpiece of Baroque style and hosts important frescoes, floor mosaics and paintings. Our objective was to investigate whether it was possible to retrieve some physical properties of the walls of the cathedral and detect possible internal fractures, meaningful gradients of moisture, or even possible structures inside the walls, hidden and walled during the past centuries.

In this case we made use of a commercial pulsed GPR system, RIS HI Mode manufactured by IDS Ingegneria dei Sistemi, equipped with a 2000 MHz nominal central frequency antenna.

The first pursued goal was to evaluate the relative dielectric permittivity of the walls. The relative permittivity ε_r of a wall built with a non-magnetic material can be easily calculated from GPR data as follows. If p is the thickness of the wall and t is the instant when the echo coming from the other side of the wall is observed (with respect to the side where we put the antenna on the wall), then the propagation velocity c of the electromagnetic waves in the wall can be estimated as:

$$c = 2p/t \qquad (1)$$

where the presence of the factor 2 is due to the fact that the radiated pulse has to reach the other side of the wall and back-propagate to the GPR antenna. Implicit assumptions to use this formula are: the frequency dispersion is neglected, the electromagnetic wave is assumed to be substantially 'TEM' (transverse electromagnetic) with respect to the air-wall interface, and the wall is assumed to be composed of a homogeneous material. As we are assuming that the wall material is nonmagnetic, the propagation velocity of the waves in the wall is linked

to the propagation velocity of the waves in air ($c_0 = 3 \cdot 10^8$ m/s) by the well-known relationship:

$$c = c_0/\sqrt{\varepsilon_r} \tag{2}$$

By exploiting (1) and (2), it is easy to obtain:

$$\varepsilon_r = \left(\frac{tc_0}{2p}\right)^2 \tag{3}$$

where t was measured with a GPR and p was measured with a common tape meter.

It may happen that the other side of the wall is not visible, e.g., because the wall is too thick and the losses too intense. It may also happen the wall is stratified and in this case it is not immediate to recognize, among several flat reflectors identifiable in the signal, which one can be ascribed to the other side of the wall. A metal sheet put on the other side of the wall can be useful to enhance the relevant reflection.

When the other side of the wall is not visible, the propagation velocity in the wall can be estimated from the diffraction hyperbolas visible in the data, if any. In particular, if a target is small with respect to the central wavelength of the emitted pulse, then, at a position x, the return time t of the pulse reflected by a target is linked to the propagation velocity c by the following equation:

$$t = \frac{2}{c}\sqrt{(x - x_0)^2 + \left(\frac{ct_0}{2}\right)^2} \tag{4}$$

where x_o is the abscissa of the axis of the small target and t_o is the minimum return time, measured when the GPR passes over the target. Equation 4 describes a hyperbola in the plane (x, t). The hyperbola is parametric in c and can be graphically matched with a trial hyperbola having the same vertex (x_o, t_o) and larger or narrower prongs depending on the chosen trial value of c. More details about this procedure can be found in the literature [4].

Coming back to our investigations in the co-cathedral of St. John, we performed a measurement on the wall of the chapel of the Oratory. The wall was quite thick: the other accessible side was about 5 meters distant. It was therefore difficult to see the other side of the wall with the antenna at disposal; we hoped to find some non-homogeneities in the wall, which would have permitted us to apply the hyperbola

procedure described above and estimate an average value of the relative permittivity in the medium at hand. But, the results presented in Figure 18 show revealed that the wall is very homogeneous, therefore we could not perform any permittivity evaluation.

After a processing composed by zero timing at 4 ns, background removal, gain application versus depth and Butterworth filtering in the band 50 MHz - 3500 MHz, we observed that the signal just sank progressively in the noise versus the depth. No meaningful internal fracture, no meaningful gradient of moisture and no walled feature were detected. The scan of the wall was performed from the floor level up, and we just identified some flat reflection in the lower part, maybe due to the plaster.
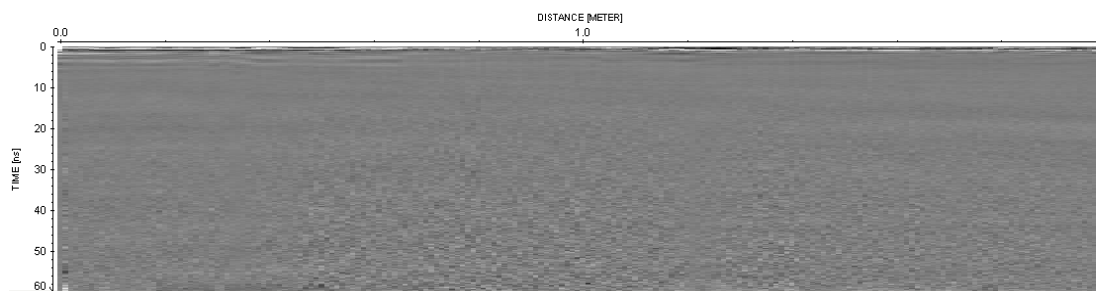
FIG. 18 - Processed B-Scan gathered on the wall of the chapel of the oratory.

Then, we prospected another wall, which was only 25 cm thick, in a corridor of the Oratory. We repeated the measurements twice, the second time putting a flat metal (copper) sheet on the other side of the wall, in order to carry out a comparison of the reflections achieved with and without the metal sheet. The length of the metal sheet was about 1 m, its width was about 50 cm and its thickness was 5 mm. The reflection from the metal sheet, if visible, would enable to estimate the propagation velocity of the electromagnetic waves in the wall (and we might assume the same propagation velocity in all the walls of the cathedral, although we do not know whether they are all made with the same material). The results are shown in Figure 19. The B-Scans were gathered in the bottom up direction, starting from the floor level. Unfortunately, the other side of the wall was not visible, which this time was absolutely not expected. This means that the walls of the cathedral are highly lossy. Moreover, also in this case the wall appears to be rather homogeneous.

The processing procedure was similar to the previous case, with just some small data driven difference. This holds also with regard to the next B-Scans that we are going to show.
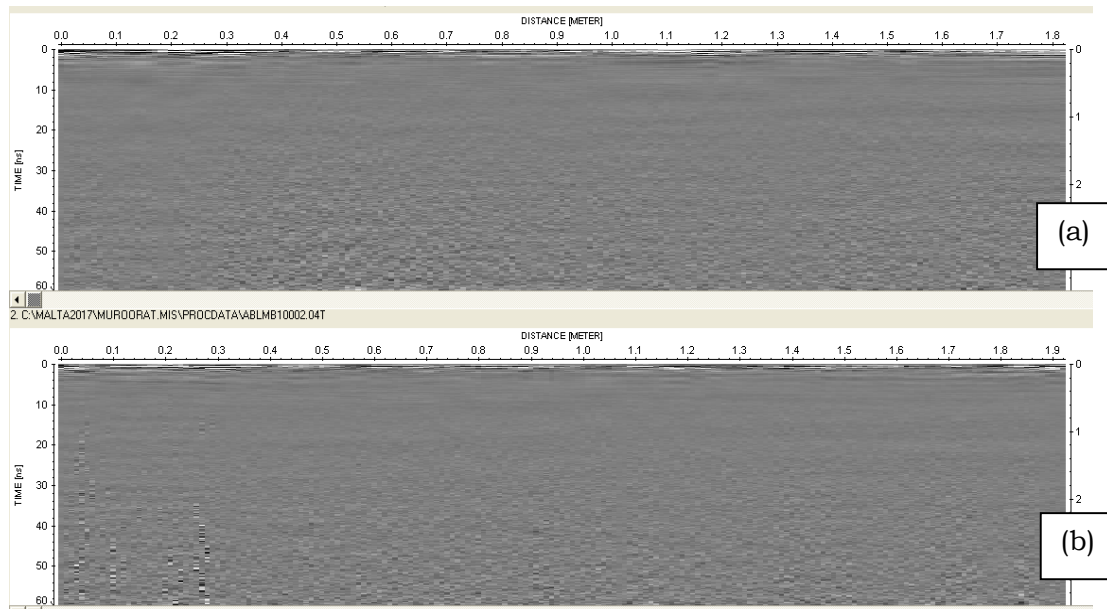
FIG. 19 - (a) B-Scan gathered on a 25-cm thick wall, in the co-cathedral of St. John and (b) B-Scan gathered on the same wall, with a metallic sheet on the opposite side of the wall.

We continued our investigation in the co-cathedral and found an ashlar along the stairs that lead to the "Bartolotti Chapel," probably of the same kind of the ashlar exploited for restoring works. Incidentally, the Bartolotti chapel was below the Oratory and was closed to the public. We repeated our measurements on the ashlar twice, the second time placing the copper sheet behind the ashlar; results are presented in Figure 20. The signal was not very clear, because the reduced size of the ashlar caused the presence of multiple reflections coming from several directions, which amplitudes were much higher than in the previous cases. Nonetheless, this time the effect of the copper sheet was visible in the radargram and we have indicated it with a black arrow in Figure 20(b): the copper sheet made the reflection from the other side of the ashlar stronger and masked the deeper echoes. The reflection does not look perfectly parallel to the air-ashlar interface, because the shape of the external surface of the ashlar was not perfectly flat. As the reflection

coming from the other side appeared to be at about 6 ns, we estimated a velocity of propagation of 6 cm/ns. This means that the relative permittivity is approximately equal to 25: such value is compatible with the humid environment, which makes humid (and lossy) the stones.
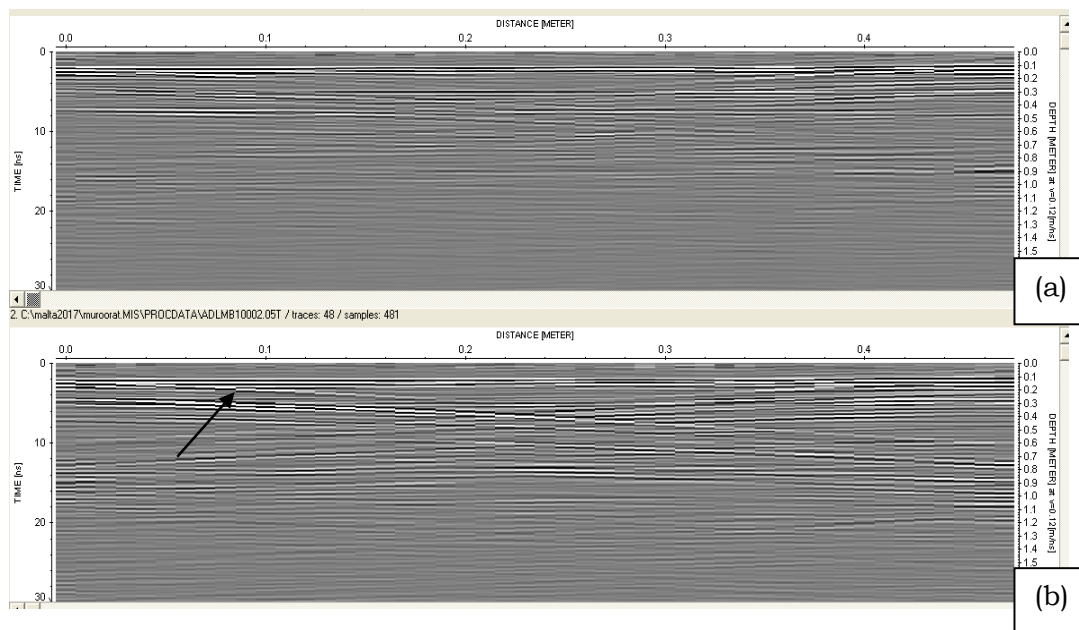
FIG. 20 - (a) B-Scan gathered on a 14-cm thick ashlar in the co-cathedral of St. John and (b) B-Scan gathered along the same path with a metallic sheet behind the ashlar.

We also performed a few more measurements on other walls, but the results were not clear, we therefore deem that they are not worth being presented.

5. GLOBIGERINA WALLS IN THE UNIVERSITY OF MALTA

Due to the poorness of the results achieved on the walls of the co-cathedral of St. John, we looked for a crossed comparison with some other structures. This was mainly done to verify whether the results obtained in the co-cathedral were reliable, and the walls of the co-cathedral can be really considered lossy and very dense (in an electromagnetic sense), or maybe there was an ill-functioning of the equipment or some trivial errors were done. We therefore decided to perform measurements on the walls of a building of the University of

Malta, made of globigerina – which should be the same material composing the walls of the co-cathedral of St John.

In the University we achieved much clearer results, this confirmed that our equipment was working well and that our data acquisition method was correct. There probably just was a strong difference between the walls of the University and those of the co-cathedral. This may sound strange, because the walls are claimed to be made of the same material, and further studies are needed, in order to better understand the reasons of such differences. We can anticipate that preliminary waveguide measurements performed by the University of Malta on globigerina samples show that the relative permittivity of globigerina changes significantly when the water content varies. Moreover, even if the material of the University and co-cathedral walls were chemically the same, differences in the electromagnetic answer could be generated by a different porosity, which may be due to the different pressure level to which the two structures are subjected; finally, the different temperature in the two buildings may also have an effect (but this is expected to be a less influent factor).

One of the measurements was done at the first floor of department of physics of the University of Malta, on a 23-cm thick wall. The GPR system was the same IDS RIS HI Mode that was used in the co-cathedral, equipped with the same 2000 MHz antenna. Results are reported in Figure 21: in particular, in (a) we show the reflection generated by the other side of the wall (that in the case at hand was clearly visible), whereas in (b) three diffraction hyperbolas are matched. The processing was performed with the commercial software Reflexw. In Figure 21(b), a background removal was applied to the data in order to make more evident the (presumably) small reflectors that generated the diffraction hyperbolas. From Figure 21(a), we measured that the flat reflection occurred after 3.17 ns: with this timing and with formula (3), we estimated a propagation velocity in the wall of 14.51 cm/ns and a relative permittivity $\varepsilon_r = 4.27$.

Then, we put a copper sheet behind the wall and repeated the measurements. The results are presented in Figure 22. The presence of the metal sheet is made evident by the stronger reflection generated at the opposite side of the wall and also by the 'tail' occurring in the signal when the antenna passes beyond the maximum abscissa of the copper plate. Such tail is indicated by an arrow in Figure 22(a). In Figure 22(b)

we repeated the measurements recorded without the metal sheet to facilitate the comparison.
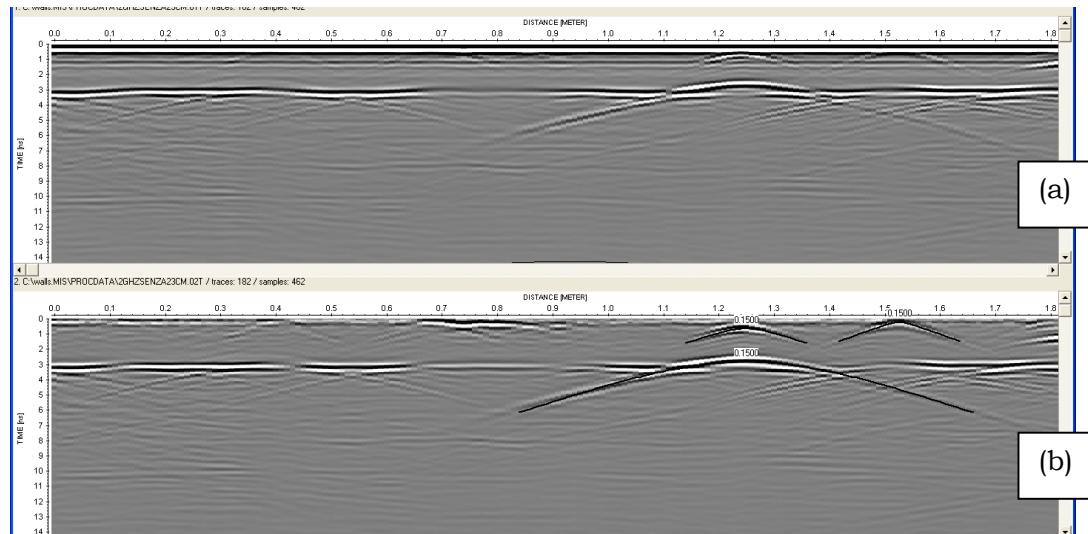
FIG. 21 - (a) GPR data recorded on a 23-cm thick wall, by using a 2000-MHz antenna; (b) the same signal as in (a), after background removal and with three diffraction hyperbolas matched.
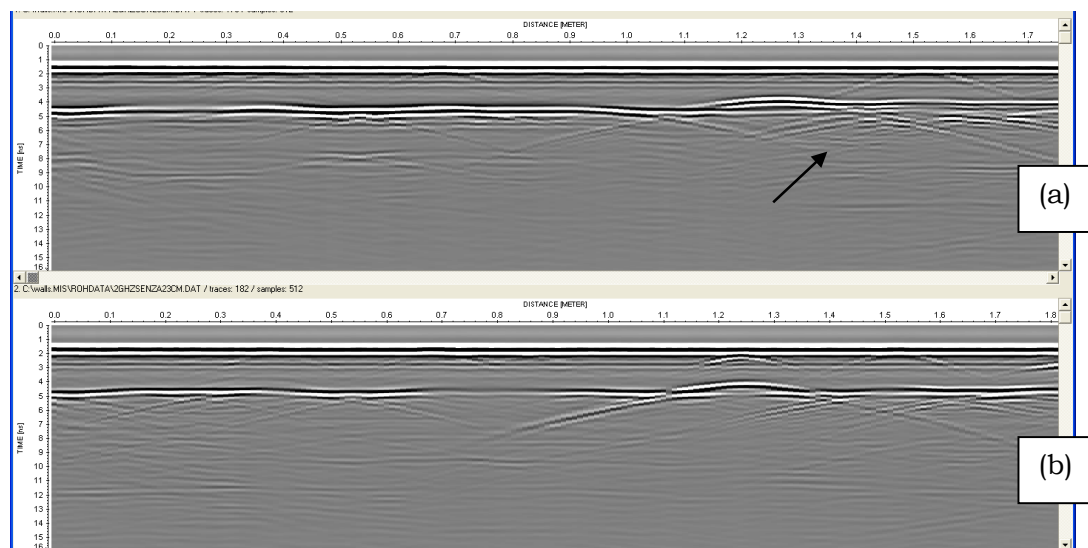
FIG. 22 - (a) Data recorded on the same wall as in Fig. 21, with a metal sheet behind the wall; (b) data recorded without the metal sheet, for comparison.

The same measurements, with and without metal sheet, were repeated by using an antenna with nominal central frequency at 900 MHz. The

results are shown in Figure 23. The tail of the metal sheet is even more evident, but there is a loss of resolution that makes the antenna hardly suitable for the case at hand. In particular, in this case we cannot see evident diffraction hyperbolas reliably ascribable to small targets. From the return time of the flat reflector, we measured a return time of 3 ns and consequently a propagation velocity of 15.33 cm/ns and a relative permittivity $\varepsilon_r = 3.83$. The measurements at 2000 MHz look more reliable, because with the antenna at 900 MHz the resolution is of the same order as the return time.
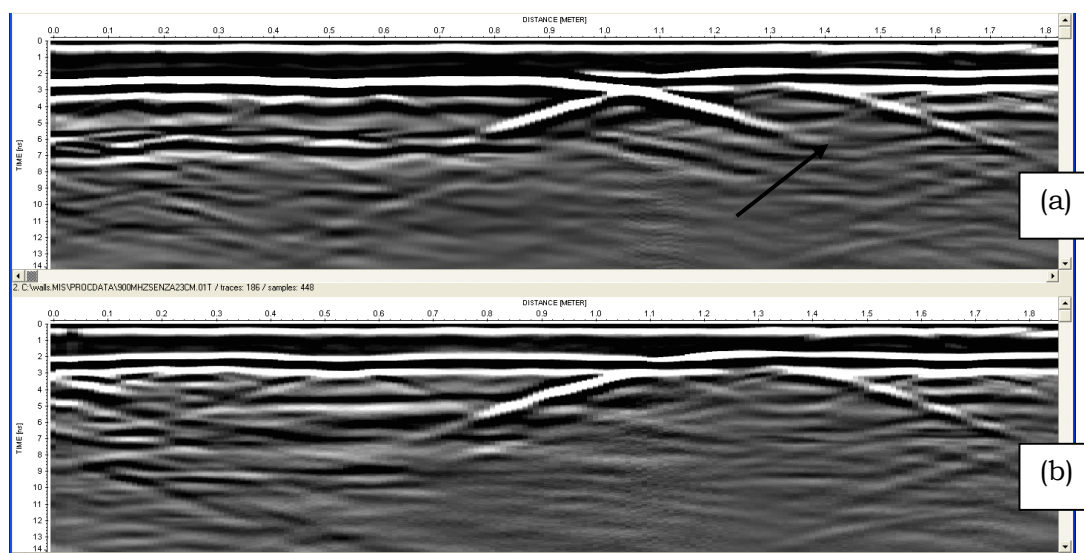
FIG. 23 - GPR data recorded on the same wall as in Fig. 21, by using a 900-MHz antenna, (a) with a metal sheet behind the wall and (b) without metal sheet. The arrow indicates the tail left by the metal sheet in the signal when the antenna went beyond it.

Then, we performed measurements on a wall at the ground floor of the same building, inside the department. This wall was 61 cm thick. Figure 24 shows the results obtained with the antenna at 900 MHz. In this case we measured a return time of 8 ns, corresponding to a propagation velocity of 15.25 cm/ns and to a dielectric permittivity $\varepsilon_r = 3.87$. We performed the measurements on the same wall also with the 2000-MHz antenna. The results are presented in Figure 25. It can be observed, both from Figure 25 and Figure 26, that the wall was not perfectly homogeneous. In particular, it contained three well visible anomalies, which may be related to internal reinforcement bars. From the data of Figure 25(a), we noticed that the reflection time from the

most reflective point was t = 8.3 ns, yielding to a propagation velocity of 14.70 cm/ns and a relative permittivity ε_r = 4.17. From the radargram recorded without the sheet (Figure 25(b)) we retrieved t = 8.24 ns, with a propagation velocity of 14.81 cm/ns and a relative permittivity ε_r = 4.11.
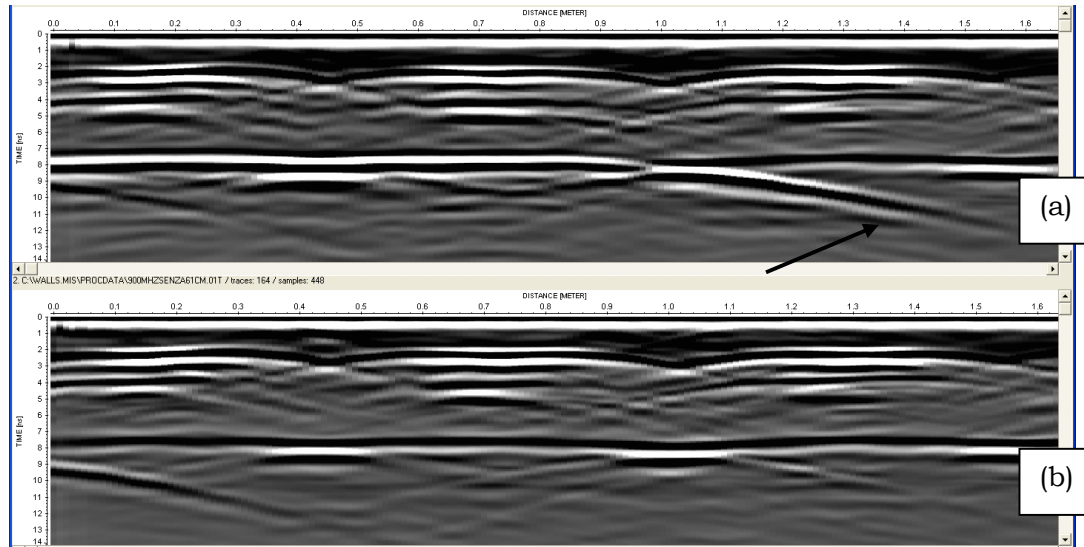
FIG. 24 – GPR data recorded on a 61-cm thick wall, with a 900-MHz antenna (a) with a metal sheet behind the wall, (b) without metal sheet. The arrow indicates the tail left by the metal sheet in the signal when the antenna went beyond it.

After that, we performed measurements on a pillar outside the department. The cross section of the pillar was a square, with an area of 45×45 cm^2. A first radargram was recorded on one side of the pillar, by using the 2000 MHz antenna (see Figure 26). The far side of the wall was hardly visible and the metal sheet did not leave any tail after its end. This indicated that the wall was probably more lossy than the walls inside the building, but we were not able to estimate the losses at this stage. In the data collected without metal sheet we observed two flattish reflections and this could generate ambiguity, whereas in the signal recorded with the metal sheet we observed only one flattish reflector, which masked the other one and made more reliable the relative-permittivity estimation. From these data, we measured t = 6.18 ns, a propagation velocity of 14.56 cm/ns and a relative permittivity ε_r = 4.24 without the metal sheet, and t = 6.3 ns, a propagation velocity of 14.29 cm/ns and a relative permittivity ε_r = 4.41 with the metal sheet.
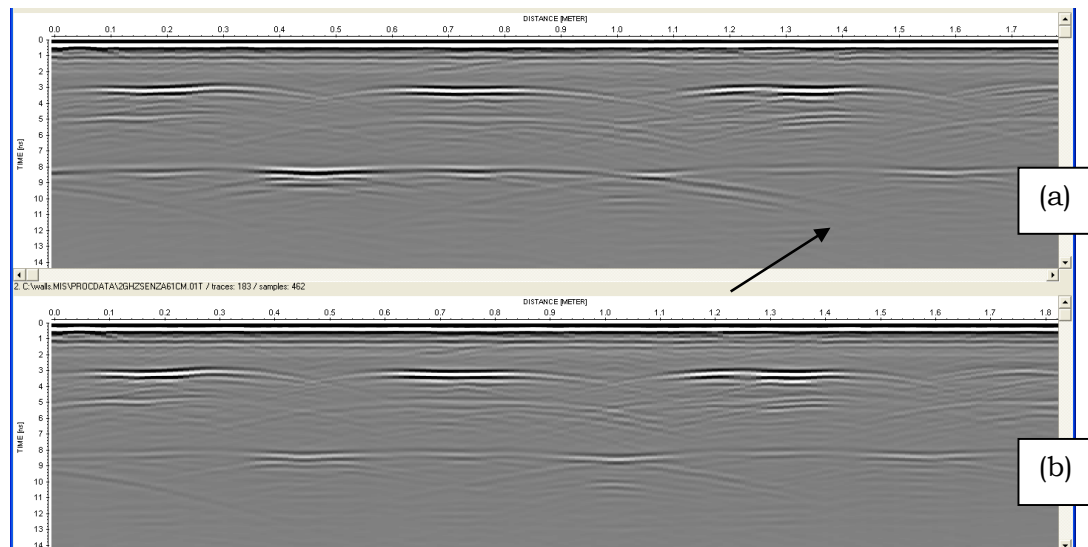
FIG. 25 - (a) GPR data recorded on a wall 61 cm thick with an antenna working at 2000 MHz and with a metal sheet behind the wall; (b) same as in (a), without the metal sheet. The arrow indicates the tail left by the metal sheet in the signal when the antenna went beyond it.
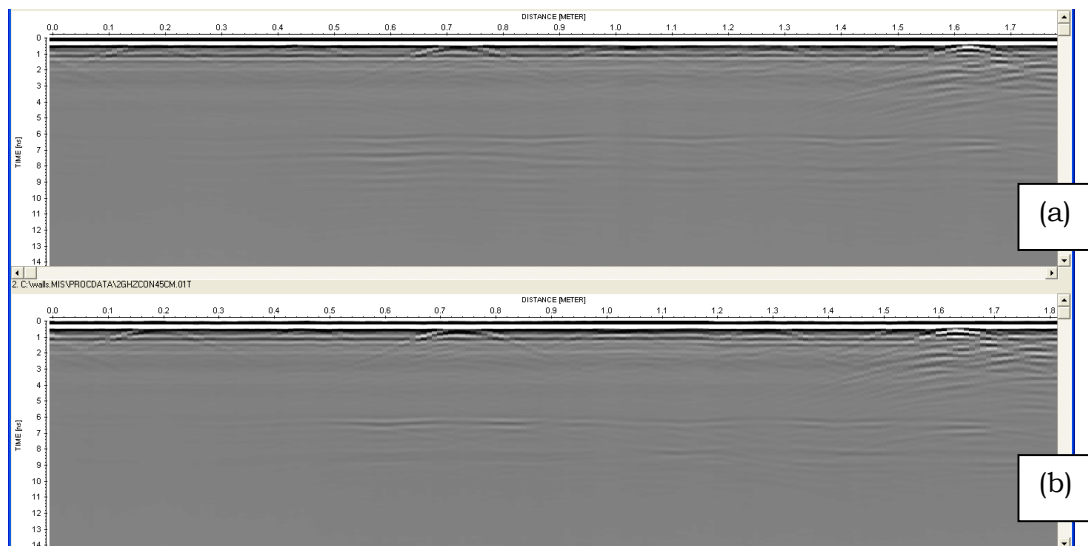
FIG. 26 - GPR data on a wall 45 cm thick, recorded with an antenna at 2000 MHz (a) without metal sheet behind the wall and (b) with the metal sheet.

We repeated the measurements with the same antenna on the two orthogonal sides of the same pillar. The results are presented in Figure 27. The data of Figure 27 are better than those of Figure 26, because

the antennas were more centred with respect to the pillar, which was not possible in the previous case because of the presence of a railing. In Figure 27(b) we can observe (even if hardly) the tail of the metal sheet. The permittivity estimation did not change significantly, with respect to the estimation done on the basis of the results shown in Figure 26. This indicated that the material was not anisotropic, at least not along the cross plane.
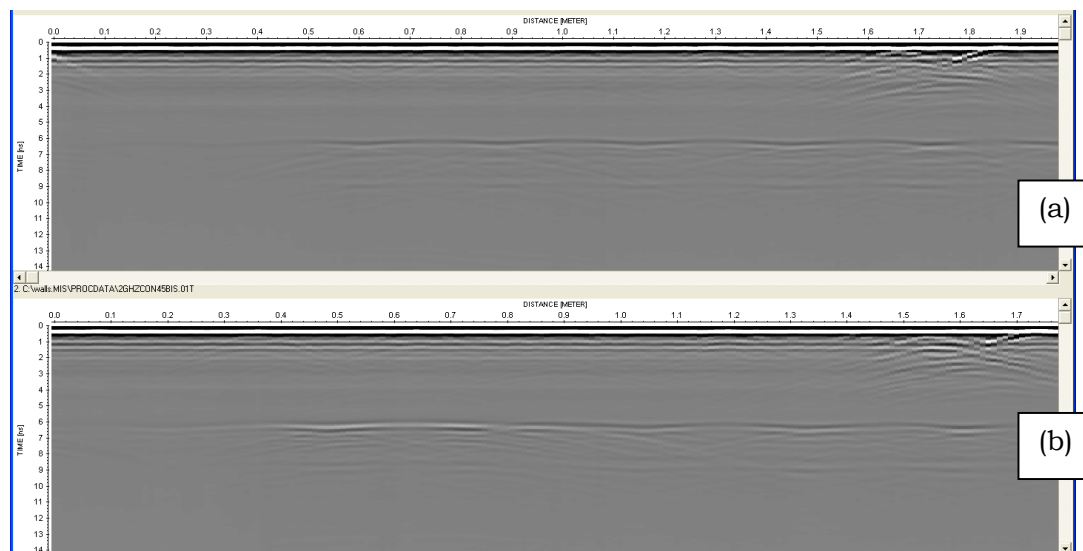
FIG. 27 – GPR data recorded on a wall 45 cm thick by using a 2000 MHz antenna, on the orthogonal sides of the pillar with respect to Figure 26, (a) without metal sheet behind the wall and (b) with the metal sheet.

Finally, we repeated the measurements on the same side of the pillar as in Fig. 27, but with the 900-MHz antenna. The recorded radargrams are presented in Figure 28. Now the metal sheet is well visible, because of the deeper penetration of the signal, and also the tail of the sheet is quite clear. The estimations based on the results in Figure 28 give: $t = 6$ ns, a propagation velocity of 15 cm/ns, and a relative permittivity $\varepsilon_r = 4$.

The discrepancies between the results achieved at 900 MHz and 2000 MHz may be partly ascribed to the frequency dispersion properties of the material. But mostly, they are ascribable to the worse resolution achievable with the 900 MHz antenna. The metal sheet might appear slightly longer or shorter in the various measurements: this is due to the fact that the odometer may slide without rotating in some cases, but this does not invalidate, of course, the achieved results.

In conclusion, we considered three walls of different thickness made of the same material and found in different areas of the same University building, and the material turned out to be different in terms of electromagnetic properties.
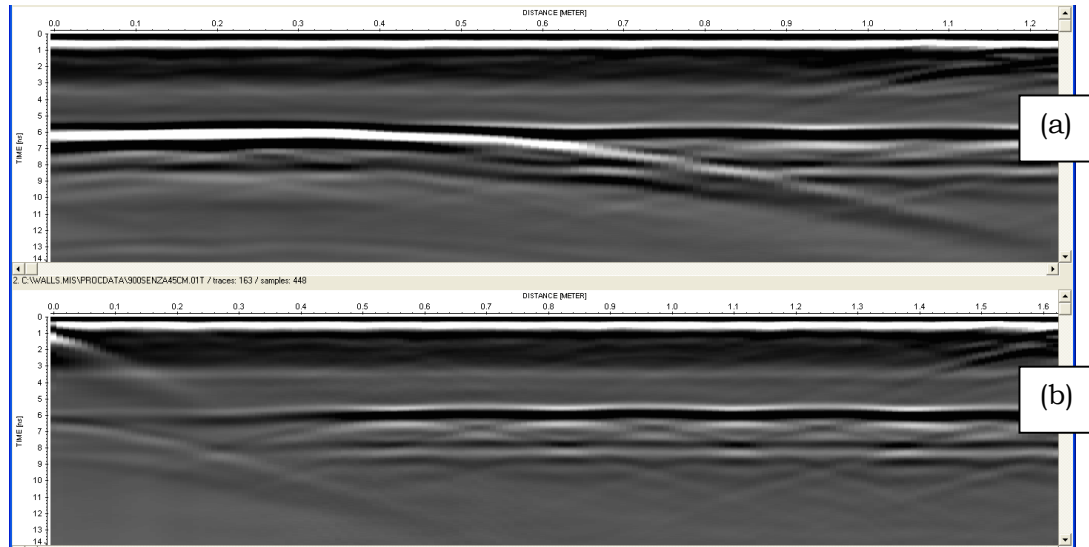
FIG. 28 – GPR data recorded on a wall 45 cm thick with an antenna at 900 MHz and (a) with a metal sheet behind the wall, (b) without metal sheet.

6.   CONCLUSIONS

In this paper we presented the results of a series of Ground Penetrating Radar (GPR) surveys carried out in Malta, in sites of historical and cultural interest.

We first used a reconfigurable stepped-frequency GPR prototype to inspect the Argotti Garden in Floriana, looking for ancient buried cisterns, but we could not find them, mainly because we were authorised to gather just a limited number of profiles. Further investigations are needed and permission for gathering a grid of profiles is necessary, in order to get horizontal images of the ground, at different depths, which will help to discriminate whether some anomalies can be ascribable to the top of the sought cisterns. Moreover, and above all, we think that a three dimensional geoelectrical prospecting may provide better results, for this kind of investigation, than a GPR survey, given the depth and strong resistivity of the anomalies looked for.

We then assessed the floor of the Nymphaeum inside the garden, to check its conditions prior to restoration works and verify whether cavities were present in the subsurface. We collected a grid of profiles by using our reconfigurable stepped-frequency GPR prototype. We found some anomalies close to the entrance of the Nymphaeum and excluded the presence of superficial cavities. We also observed that the floor of the Nymphaeum is made of a different material than the path leading to its entrance.

We subsequently used a commercial pulsed GPR system to assess the walls of the co-cathedral of St. John, in Valletta. The main purpose of our study was to detect internal fractures, meaningful gradients of moisture, or even possible structures inside the walls, hidden and walled during the past centuries. However, the walls turned out to be highly lossy and so the data that we recorded were obscure and difficult to be interpreted. We performed additional measurements on the walls of a building of the University of Malta, in Msida, which are made of the same material as the walls of the co-cathedral, for comparison. This allowed us to better understand the electromagnetic properties of the material at hand. We estimated the propagation velocity of the electromagnetic waves in the walls of the University building and their relative permittivity.

ACKNOWLEDGEMENTS

REFERENCES

[1]   R. Persico and S. D'Amico, "Use of Ground Penetrating Radar and standard geophysical methods to explore the subsurface," Ground Penetrating Radar, vol. 1(1), pp. 1-37, 2018.

[2]   R. Persico, D. Dei, F. Parrini, and L. Matera, Mitigation of narrow band interferences by means of a reconfigurable stepped frequency GPR system, Radio Science, pp. 1322–1331, 2016.

[3]   R. Persico and G. Leucci, Interference Mitigation Achieved with a Reconfigurable Stepped Frequency GPR System, Remote Sensing, vol. 8(11), pp. 926–936, 2016.

[4]   R. Persico, Introduction to Ground Penetrating Radar: Inverse Scattering and Data Processing, Wiley, 2014.

Electrical resistivity tomography investigations in Mgarr (Malta)

Raffaele Persico[1], Sebastiano D'Amico[2], Enzo Rizzo[3],
Luigi Capozzoli[3] & Aaron Micallef[2]

[1] Institute for Archaeological and Monumental Heritage of the National Research Council (IBAM-CNR), Lecce, Italy
R.PERSICO@IBAM.CNR.IT

[2] University of Malta, Faculty of Science, Msida, Malta
SEBASTIANO.DAMICO@UM.EDU.MT, AARON.MICALLEF@UM.EDU.MT

[3] Institute of Methodologies for Environmental Analysis of the National Research Council (CNR-IMAA), Tito Scalo – Potenza, Italy
ENZO.RIZZO@IMAA.CNR.IT, LUIGI.CAPOZZOLI@IMAA.CNR.IT

Abstract

This paper presents the results of electrical resistivity tomography (ERT) investigations carried out in Mgarr, Malta. All measurements were performed during a Short-Term Scientific Mission (STSM) funded by the COST (European Cooperation in Science and Technology) Action TU1208 "Civil engineering applications of Ground Penetrating Radar." The work performed during the STSM consisted also in the processing and interpretation of the gathered data.

Keywords: Electrical resistivity tomography; Hydrogeology.

1. Introduction

A Short-Term Scientific-Mission (STMS) entitled "Integrated geophysical investigations of sites of cultural interest in Malta" was recently funded by COST (European Cooperation in Science and Technology), in the framework of the COST Action TU1208 "Civil engineering applications of Ground Penetrating Radar" activities. Raffaele Persico, Luigi Capozzoli and Enzo Rizzo visited Sebastiano D'Amico and Aaron Micallef in Malta, from March 5th to March 18th, 2017, and they jointly investigated a series of sites of cultural interest. During the STSM, electrical resistivity tomography (ERT) measurements were carried out near the village of Mgarr, on the western coast of Malta. The objective of this paper is to present the results of that ERT campaign.

Overall, seven ERT profiles were gathered. Our main purpose was to perform a hydrogeological study of the carbonate rocks close the sea. In particular, we aimed at obtaining information concerning the groundwater seepage in the eroding valley of Gnejna Bay, a popular tourist destination about 1 km from Mgarr, which is an area of both naturalistic and cultural interest. Initially, we planned to use both ERT and a Ground Penetrating Radar (GPR), but we soon recognised that the scenario was not suitable for GPR investigations, because the surface to be inspected was too rough, and it was not possible to properly push the GPR over it. Therefore, we performed a geoelectrical investigation, only. As is well known, ERT acquisitions allow a much deeper penetration than GPR, although they cannot provide the same resolution.

In Section 2 we describe the geological setting of our measurements, in Section 3 we shortly resume our data acquisition and elaboration approaches, in Section 4 we present and interpret the results, and finally, in Section 5 the conclusions of our study are drawn.

2.   GEOLOGICAL SETTING

The Island of Malta lies in the central Mediterranean Sea, 100 km south of Italy and 290 km east of Tunisia. The Maltese Islands are predominantly composed of marine sedimentary rocks (Figure 1). The Maltese sedimentary rocks result from the compaction of fragments of rocks, remains of marine plants, animals and chemicals under the sea water level. The deposition and accumulation of such materials went on for millions of years; they derived from the sea (limestone), or from the land (blue clay) – in the latter case they were brought to the sea by the rain, wind and other agents. The rock formations forming the Maltese Islands are (see Figure 2, from top to bottom): the Upper Coralline Limestone, the Greensand, the Blue Clay, the Globigerina Limestone, and the Lower Coralline Limestone [1].

From a hydrogeological point of view, the Upper and Lower Coralline Limestone function as the main aquifer rocks, while the Globigerina Limestone functions locally as an aquifer transmitting water from the surface into the main groundwater bodies along the fractures. The Upper Coralline Limestone aquifers are called perched aquifers, due to the underlying impermeable Blue Clay formation [2].
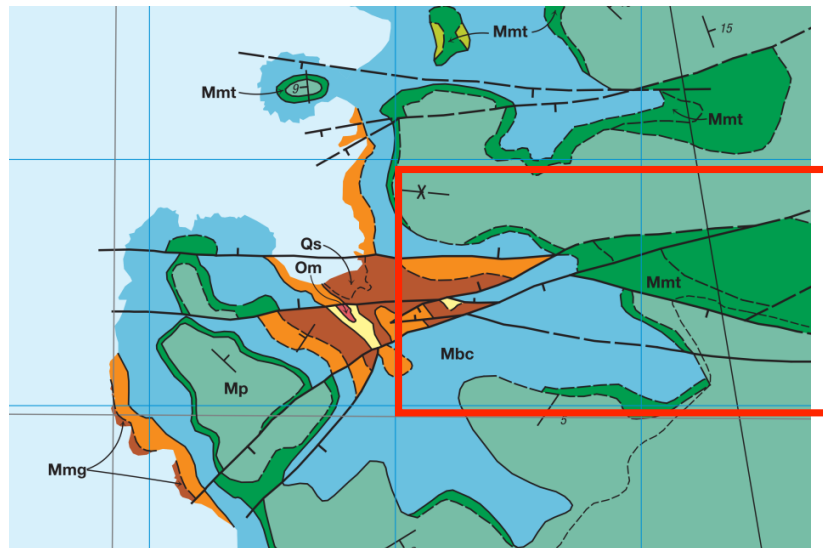
FIG. 1 - Excerpt of the Geological Map of Maltese Islands (the red square shows the investigated area, Gnejna Valley). Mp (green light colour) and Mnt (green dark colour) indicate Upper Coralline Limestone; Mbc (blue colour) is Blue Clay; Mug (orange colour) and Mmg (brown colour) indicate Globigerina Limestone; Om is a top member of Lower Coralline Limestone and Qs is modern beach sand.
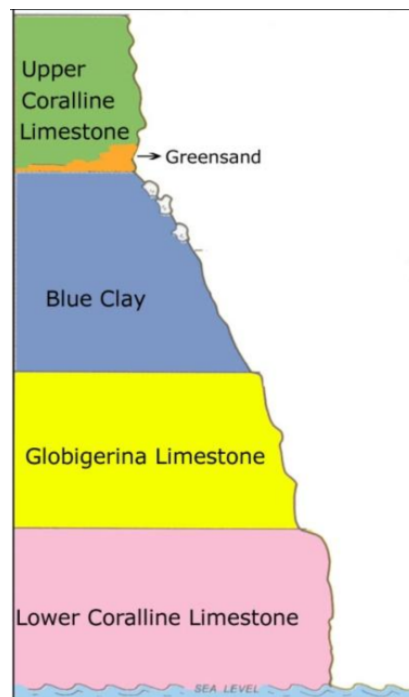
FIG. 2- The rock formations in the Maltese Islands.

3. GEOELECTRICAL METHODOLOGY AND DATA ELABORATION

The electrical resistivity method is essentially based on the measurement of a drop of potential (dV) due to a current injection (A) by a pairs of electrodes fixed in the ground. The electrical resistivity is the measured physical parameter, coming from the Ohm's law. The typical instrument is a high-resolution resistivity meter, which energizes the electrodes positioned on the ground with appropriate criteria and simultaneously measures the resistivity of the soil at various depths. The electrical resistivity basically quantifies how strongly a given material opposes the flow of electric current. A low resistivity indicates a material that readily allows the flow of electric current.

The ERT method allows obtaining the distribution of the pseudo-electrical resistivity in the subsoil, which estimation can be obtained by using various settings for the current and potential electrodes. Actually, different electrode configurations are possible (Dipole-Dipole, Wenner, Schlumberger, and more); in general, the choice is made based on the sensitivity of the employed device, the expected vertical and horizontal variations of the resistivity, the desired depth of investigation, the horizontal data coverage and the length of the signal. The pseudo-resistivity values are then elaborated in terms of real resistivity and depth, by means of suitable inversion software. The objective of the inversion procedure is to compute the 'best' set of resistivity values, which satisfy both the measured dataset and some a priori constraints, in order to stabilize the inversion and obtain the final image.

In the present work, the pseudo-resistivity data were analysed and converted in real resistivity values by using the inversion software ZondRes2D (Zond geophysical software), which is a tool for a 2.5-dimensional interpretation of ERT data. The first step was to prepare the data for the inversion. The second step was to select the inversion type and parameters. In order to transform the resistivity pseudo-section into a model representing the distribution of the electrical resistivity in the subsurface, we used the Marquardt method. This is a classic inversion algorithm that exploits the least-square method with regularization by damping parameter [3]. After that, we performed the Occam inversion: this algorithm gives the contrast subsurface model, and is an inversion by least-square method with the use of a smoothing operator and an additional contrast minimization [4]. All the resistivity

data were inverted taking into account the topography of the inspected region.

We recorded seven ERT profiles (denominated T1, T2, T3, T4, T4a, T4b, and T5) at Gnejna Valley (Figure 3), in five different sites. Only in one site, east of the erosion, we recorded three ERT profiles along the same line (T4, T4a, and T4b), but with different electrode spacing (10 m, 5 m and 2.5 m, respectively) in order to evaluate the electrical resistivity distribution with high resolution on the shallow geological formation (Upper Coralline Limestone).

The measurements were done with Syscal instruments (manufactured by the French company Iris), with 48 channels; the electrode spacing was 10 m, in order to obtain profiles 470 m long. Only three ERT acquisitions were performed with a shorter spacing: 5 m for T4a, as already mentioned, and for T5; 2.5 m for T4b, as said before. The geoelectrical method used for all the profiles was the Wenner-Schlumberger technique, which permitted to obtain a good resolution for both vertical and horizontal heterogeneities.
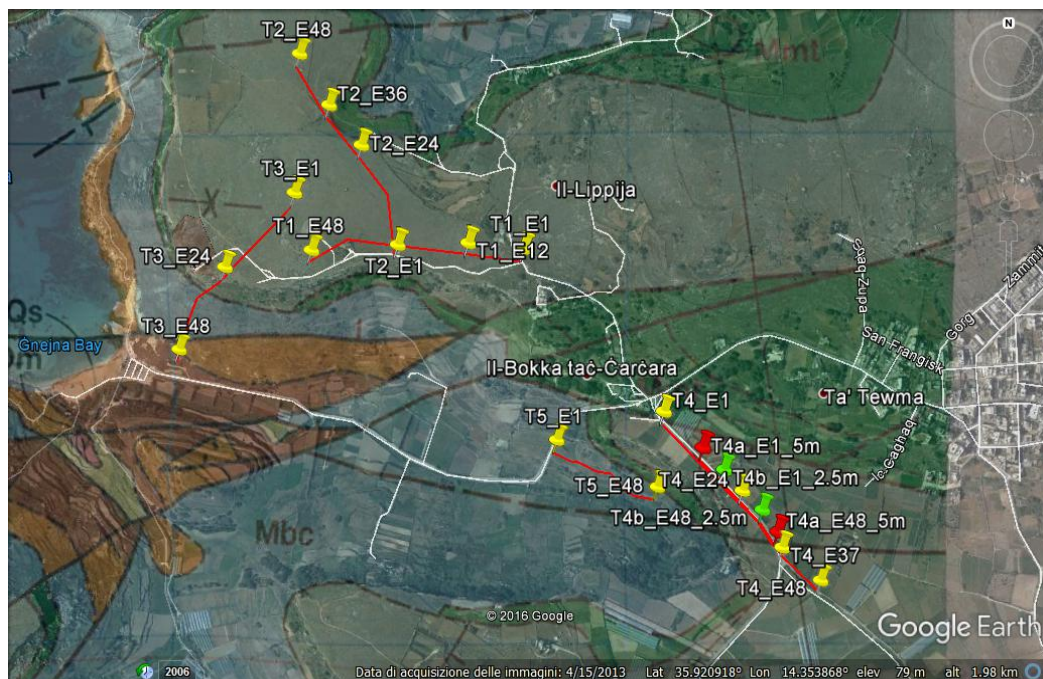
FIG. 3 – ERT profiles on a Google Earth image (with an overlay of the Geological Map). The red lines are the profiles and the pins are the specific electrodes indicated by labels.

4.   RESULTS AND INTERPRETATION

The T1 profile was recorded on the top of the coast, north of Gnejna Valley, where the Upper Coralline Limestone outcrops. Figure 4 shows the pseudo-resistivity distribution (from 3 Ωm to 2700 Ωm) after the first elaboration step. In Figure 5 a map of the inverted electrical resistivity is presented, as a function of the profile coordinate x and of the depth of investigation, with a range of values from 10 Ωm to 2000 Ωm; this image shows the presence of four Electrical Layers (ELs):

- EL1: A shallow high-resistivity layer (> 800 Ωm), with a depth from 10 m to 20 m.
- EL2: A deep highly conductive layer (< 50 Ωm), 50 m - 70 m thick.
- EL3: A layer with electrical resistivity between 200 Ωm and 600 Ωm, located between the shallow high-resistivity layer and the conductive one; it has a thickness of about 5 m.
- EL4: A deep highly resistive layer (> 200 Ohm*m), observed from x = 0 to x = 150 m and from x = 350 m to the end of the profile.

According to our geological/hydrogeological interpretation, EL1 may be associated with Upper Coralline Limestone, EL2 with Blue Clay, EL3 with Upper Coralline Limestone with water (shallow aquifer), and finally, EL4 may be associated with saturated Globigerina Limestone.

The T2 profile was recorded at the same site as T1, perpendicular to it. Figure 6 presents the pseudo-resistivity distribution (from 7 Ωm to 4000 Ωm) after the first elaboration step. In Figure 7 the map of the inverted electrical resistivity is reported, which ranges from 10 Ωm to 2000 Ωm; the same ELs as in T1 are present, but with different thicknesses:

- EL1: A shallow high-resistivity layer (> 800 Ωm), with a depth from 10 m to 40 m.
- EL2: A deep highly conductive layer (< 50 Ωm), 20 - 70 m thick.
- EL3: A layer with electrical resistivity between 200 Ωm and 600 Ωm, located between the shallow high resistivity layer and the conductive layer; the thickness is about 10 m.
- EL4: A deep highly resistive layer (> 200 Ωm), observed from x = 240 to the end of the profile.

Our geological/hydrogeological interpretation is analogous to that given for T1.

FIG. 4 - Pseudo-resistivity values acquired along the ERT profile T1. The blue triangles correspond to the electrodes. The pseudo-resistivity values are from 2 Ωm to 2700 Ωm (from green to red).

FIG. 5 - The elaborated ERT profile T1.

T3 was recorded from the top coast to the beach of Gnejna Valley. Figure 8 shows the pseudo-resistivity distribution (from 7 Ωm to 4000 Ωm) after the first elaboration step. Figure 9 shows the inverted electrical resistivity, which ranges from 10 Ωm to 2000 Ωm; the same ELs as in T1 are present, but with different thicknesses:

- EL1: A shallow high-resistivity layer (> 800 Ωm), with a depth from 10 m to 30 m, visible only from $x = 0$ to $x = 250$ m.
- EL2: A deep highly conductive layer (< 50 Ωm), located below EL1 until $x = 250$ m and shallow from $x = 250$ m to the end of the profile.
- EL3: A layer with electrical resistivity between 200 Ωm and 600 Ωm. This layer is visible only below EL1 and has a thickness of about 10 m.
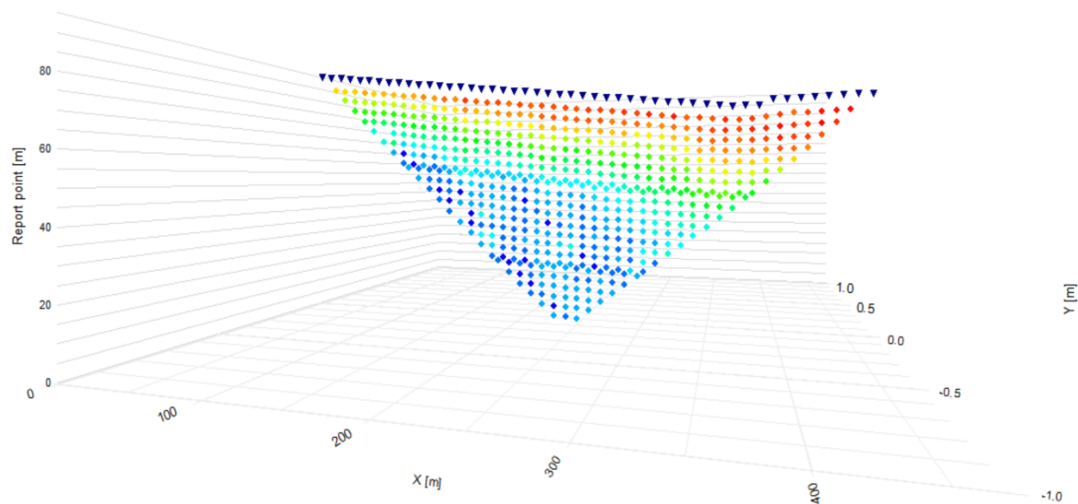
FIG. 6 - Pseudo-resistivity values acquired along the ERT profile T2. The blue triangles correspond to the electrodes. The pseudo-resistivity values are from 7 Ωm to 4000 Ωm (from blue to red).
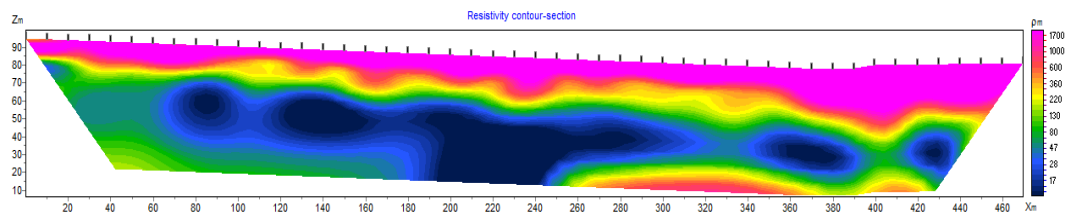
FIG. 7 - The elaborated ERT profile T2.

- EL4: A deep highly resistive layer (> 200 Ωm), observed from x = 100 m to x = 150 m and from x = 320 m to the end of the profile.

Our geological/hydrogeological interpretation is analogous to that given for T1.

T4 was recorded on the east part of the top coast of Gnejna Valley. Figure 10 shows the pseudo-resistivity distribution (from 2 Ωm to 1100 Ωm) after the first elaboration step. Figure 11 shows the inverted electrical resistivity with a range between 10 Ωm to 2000 Ωm. This map is similar to those presented before, but it has a peculiarity. In fact, in this case the observed ELs are:

- EL1: A shallow high resistivity layer (>800 Ωm) with a depth around 10 – 30 m and visible only from x = 0 to x = 380 m.
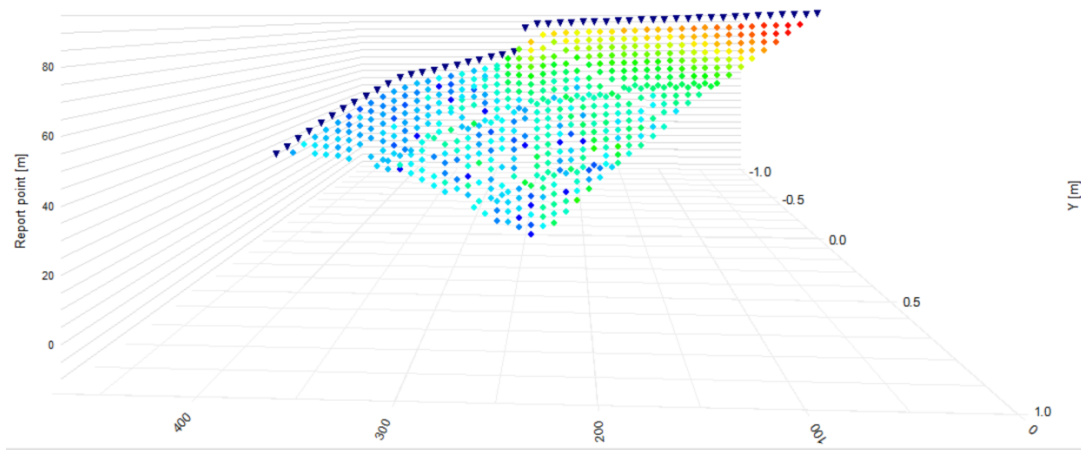
FIG. 8 - Pseudo-resistivity values acquired along the ERT profile T3. The blue triangles correspond to the electrodes. The pseudo-resistivity values are from 7 Ωm to 4000 Ωm (from blue to red).
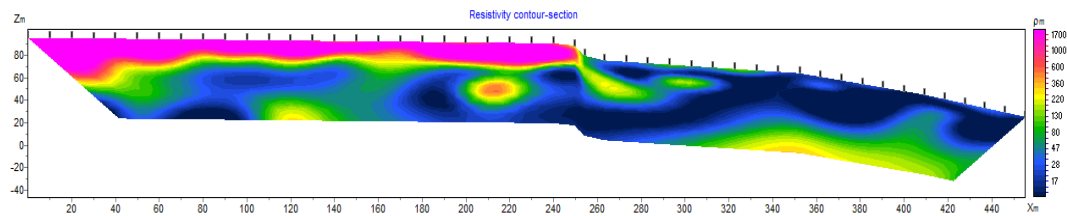
FIG.9 - The elaborated ERT profile T3.

- EL2: A deep highly conductive layer (< 50 Ωm) located below EL1 until x = 350 m.
- EL3: An electrical layer with electrical resistivity values between 600 Ωm to 200 Ωm, visible only below EL1 and with a from a few meters to around 10 m.
- EL5: A highly resistive layer (> 1000 Ωm) that covers the entire image from x = 350 to the end of the profile.
- EL6: A layer inside EL5, with electrical resistivity values < 100 Ωm.

Our geological/hydrogeological interpretation is the following: EL1 should be associated with Upper Coralline Limestone; EL2 is a Blue Clay formation; EL3 is Upper Coralline Limestone with water (shallow aquifer); EL5 should be associated with Upper Coralline Limestone and has a huge thickness because the vertical structure at x = 350 m is a

fault, as is visible on the geological map of the region as well; finally, EL6 should be a purchase aquifer, or a shallow layer of clay sediments, or else water leakage from the surface.

Along the T4 profile, we carried out additional measurements: the T4a and T4b profiles, with different electrode distances, i.e., 5 m and 2.5 m, respectively. This setting allowed increasing the resolution, so that we could obtain more information concerning the shallow aquifer in the Upper Coralline Formation.

Figure 12 shows the ERT maps of profiles T4a and T4b. These images highlight the presence of the Upper Coralline Formation and its main characteristics in this area, and the wide fracturing zones.
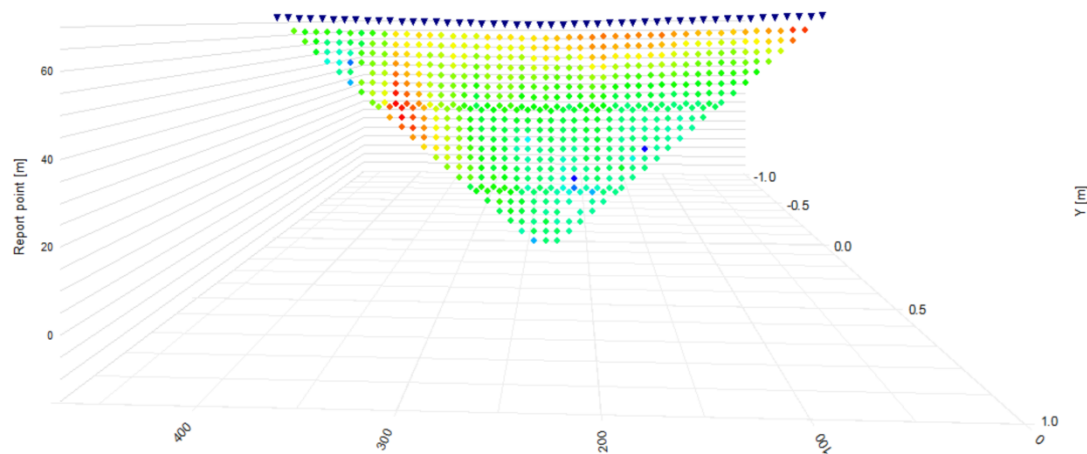
FIG. 10 - Pseudo-resistivity values acquired along the ERT profile T4. The blue triangles correspond to the electrodes. The pseudo-resistivity values are from 2 Ωm to 4000 Ωm (from blue to red).
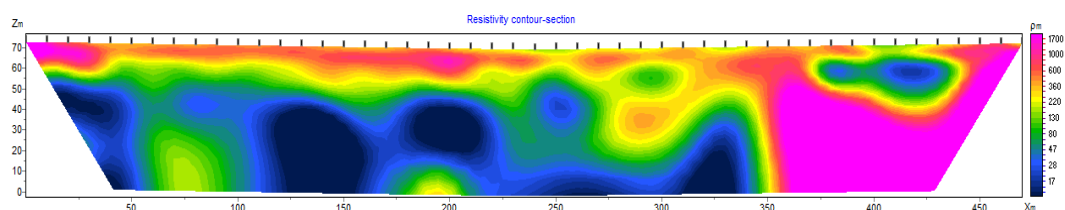
FIG. 11 - The elaborated ERT profile T4.

The ERT profile T5 was recorded along Gnejna Valley. Figure 13 shows the pseudo-resistivity distribution (from 3 Ωm to 14 Ωm) after the first elaboration step. Figure 14 shows the inverted electrical resistivity data with a range between 5 Ωm and 100 Ωm. The observed ELs are:

- EL2: A very conductive layer (< 20 Ωm).
- EL4: A deep highly resistive layer (> 20 Ωm).

Our geological/hydrogeological interpretation is as follows: EL2 should be associated to Blue Clay and EL4 to saturated Globigerina Limestone.
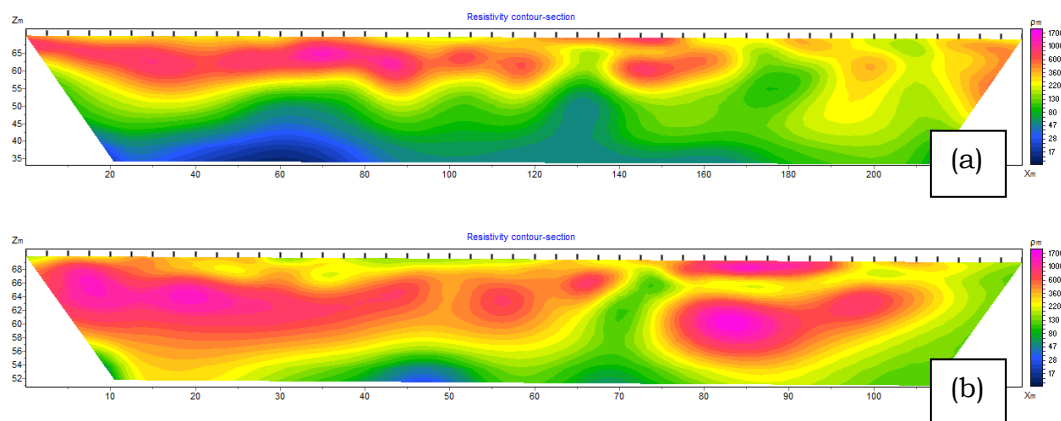
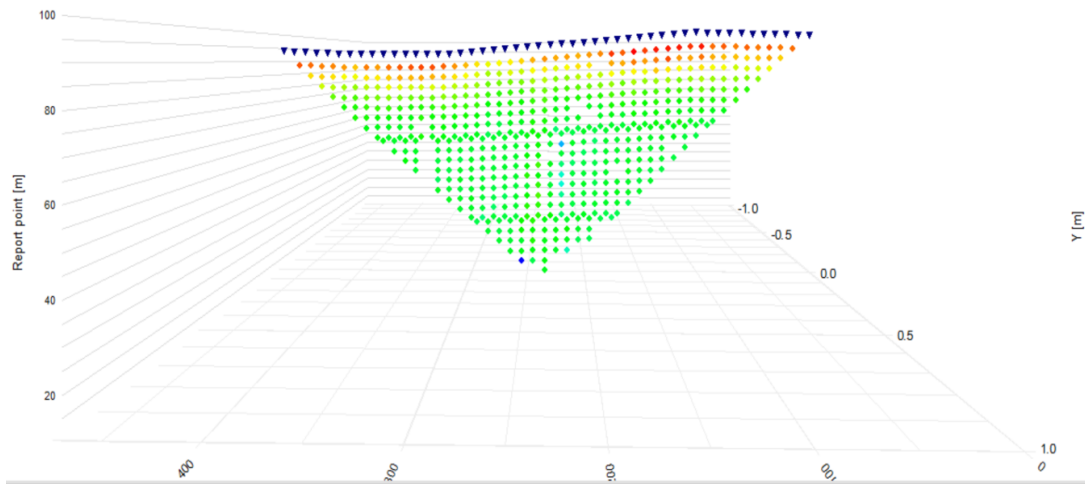**FIG. 12** - The elaborated ERT profiles T4a (a) and T4b (b).
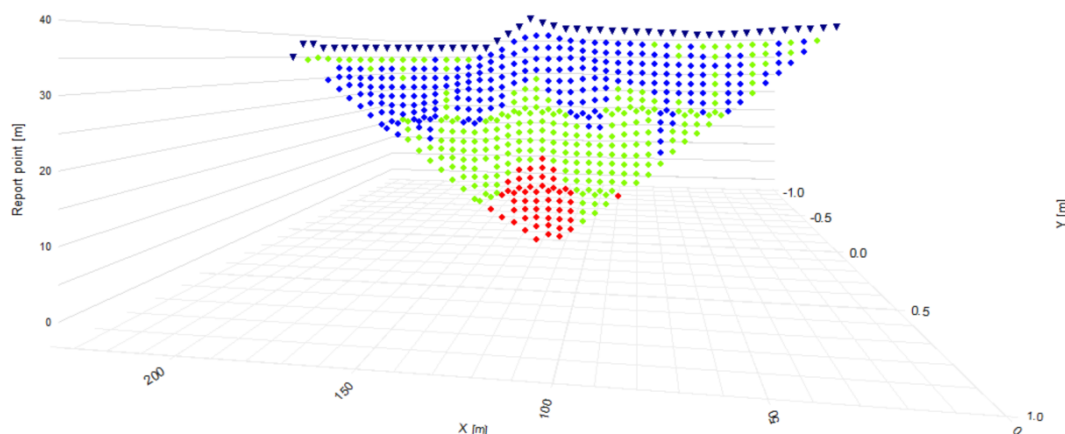
FIG. 13 - The pseudo-resistivity values acquired along the ERT profile T5. The blue triangles correspond to the electrodes. The prseudo-resistivity values are from 3 Ωm to 14 Ωm (from blue to red).
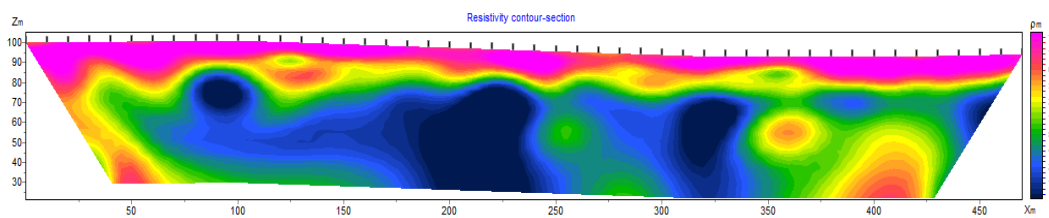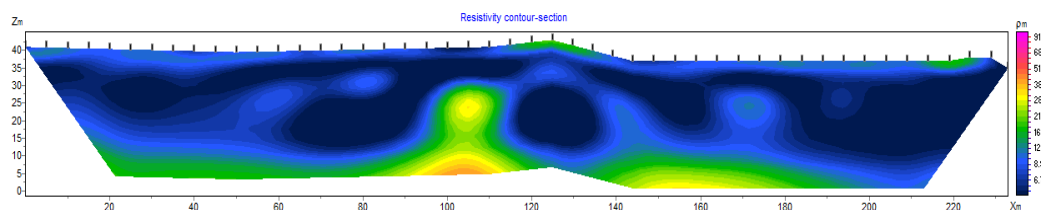
FIG. 14 - The elaborated ERT profile T5.

5.   CONCLUSIONS

In this short paper we presented and interpreted the results of electrical resistivity tomography (ERT) measurements recently performed in Malta, near the village of Mgarr. Overall, seven ERT profiles were recorded.

The results of our study contribute to the hypothesis that the groundwater is a key geomorphic agent in the formation of terrestrial and submarine theatre-headed valleys, in the carbonate bedrock of the Maltese Islands. The data acquired during this experimental campaign can also be useful to assist future ERT or GPR surveys in the region.

REFERENCES

[1]   A. Camilleri, C. Formosa and K. Sillato, n.d. Maltese Rock Formation. [Online] Available at: http://maltageo.tripod.com/html/rock_formation.html.

[2]   Malta Resources Authority (MRA) Report, 2004. Initial Characterisation of the Groundwater Bodies within the Maltese Water Catchment District under the Water Policy Framework Regulations

[3]   S. C. Constable, R. L. Parker, and G.C. Constable, "Occam's inversion: a practical algorithm for generating smooth models from electromagnetic sounding data," Geophysics, vol. 52, pp. 289-300, 1987.

Open access | www.GPRadar.eu/journal
Volume 1 | Issue 1 | January 2018   *73*   Published in Rome, Italy
by TU1208 GPR Association

https://doi.org/10.26376/GPR2018003

[4]   D. W. Marquardt, "An algorithm for least squares estimation of nonlinear parameters," ournal of the Society for Industrial and Applied Mathematics, vol. 11, pp. 431-441, 1963.

Non-destructive tests for railway evaluation: Detection of fouling and joint interpretation of GPR data and track geometric parameters

Mercedes Solla[1] & Simona Fontul[2]

[1] Defense University Center, Spanish Naval Academy, Marín, Spain
merchisolla@cud.uvigo.es

[2] National Laboratory For Civil Engineering (LNEC), Lisbon, Portugal
simona@lnec.pt

Abstract

This paper deals with railway assessment by using Ground Penetrating Radar, eventually combined with Falling Weight Deflectometer and Light Falling Weight Deflectometer. All measurements were performed during a Short-Term Scientific Mission (STSM) funded by the COST (European Cooperation in Science and Technology) Action TU1208 "Civil engineering applications of Ground Penetrating Radar." In particular, the tasks addressed were: 1. Detection of track defects at infrastructure level (voids and cracking); 2. Measurement of layer thickness; and, 3. Evaluation of the fouling level of ballast.

Keywords: Ground Penetrating Radar; Railways; Detection of track defects; Measurement of layer thickness; Fouling evaluation; Falling Weight Deflectometer.

1. Introduction

A Short-Term Scientific-Mission (STMS) entitled "Non-destructive tests for railway evaluation: detection of fouling and joint interpretation of GPR data and track geometric parameters" was funded in 2015 by COST (European Cooperation in Science and Technology), in the framework of the COST Action TU1208 "Civil engineering applications of Ground Penetrating Radar" activities. Mercedes Solla visited Simona Fontul in Lisbon, Portugal, from June 1st to June 30th, 2017, and they jointly carried out a series of experiments concerned with the non-destructive assessment of railways. The objective of this paper is to present the results obtained during the STSM.

Railways, as all infrastructures, have to behave properly during their life cycle. A regular maintenance policy has to be established, to guarantee high safety standards [1]. At the same time, costs and traffic interruptions have to be limited. Nowadays, track monitoring mainly consists in measuring parameters related to the track layout and rail wearing. During maintenance operations, some track components are replaced while others can remain the same, such as the substructure [2, 3]. The customary monitoring procedure does not detect the real causes of rail deficiency, which may be due to the presence of ballast pockets, fouled ballast, poor drainage, subgrade settlements or transitions problems [4-6]. A more thorough analysis of the conditions of both the railway platform and substructure is crucial to reduce maintenance costs and increase operational safety levels.

Non-destructive testing techniques can be effectively employed for railway assessment. The main purpose of the STSM was to study how Ground Penetrating Radar (GPR) can be used to inspect the infra- and super-structure of railways. In particular, the tasks addressed were: 1. Detection of track defects at infrastructure level (voids and cracking); 2. Measurement of layer thickness; and, 3. Evaluation of the fouling level of ballast.

Two different GPR systems were used and compared, in terms of their capability to detect defects in the subgrade (at platform level) and estimate the dielectric permittivity of concrete asphalt for sub-ballast. In particular, the available equipment included: a ground-coupled GPR manufactured by MALÅ (brought to Lisbon from the University of Vigo, Spain) and an air-coupled system manufactured by GSSI (available at the National Laboratory For Civil Engineering, in Lisbon). The MALÅ system was a ProEx control unit equipped with 1-GHz and 2.3-GHz antennas. The GSSI system was a SIR-20 control unit equipped with 1-GHz and 1.8-GHz antennas. The accuracy of different inspection procedures was evaluated, to determine the best way to proceed for assessing railways with GPR.

2. MATERIALS

2.1 TASK 1: DETECTION OF TRACK DEFECTS AT INFRASTRUCTURE LEVEL

The experimental activities were carried out in the test site shown in Figure 1. Metal plates located in the subgrade were very useful for data

interpretation and for the calibration of the air-coupled antenna (see the schemes reported in Figure 2). The soil employed to realise the road base is classified by the Unified Soil Classification System as clay of low plasticity, or lean clay. In the gradation test, 66% of such material passes the No. 200 sieve. The Atterberg limits are: plastic limit 19.9% and liquid limit 46.5%, which lead to a plasticity index of 26.6.

FIG. 1 – Photos showing the test site at LNEC and GPR data acquisition with ground- and air-coupled antennas.
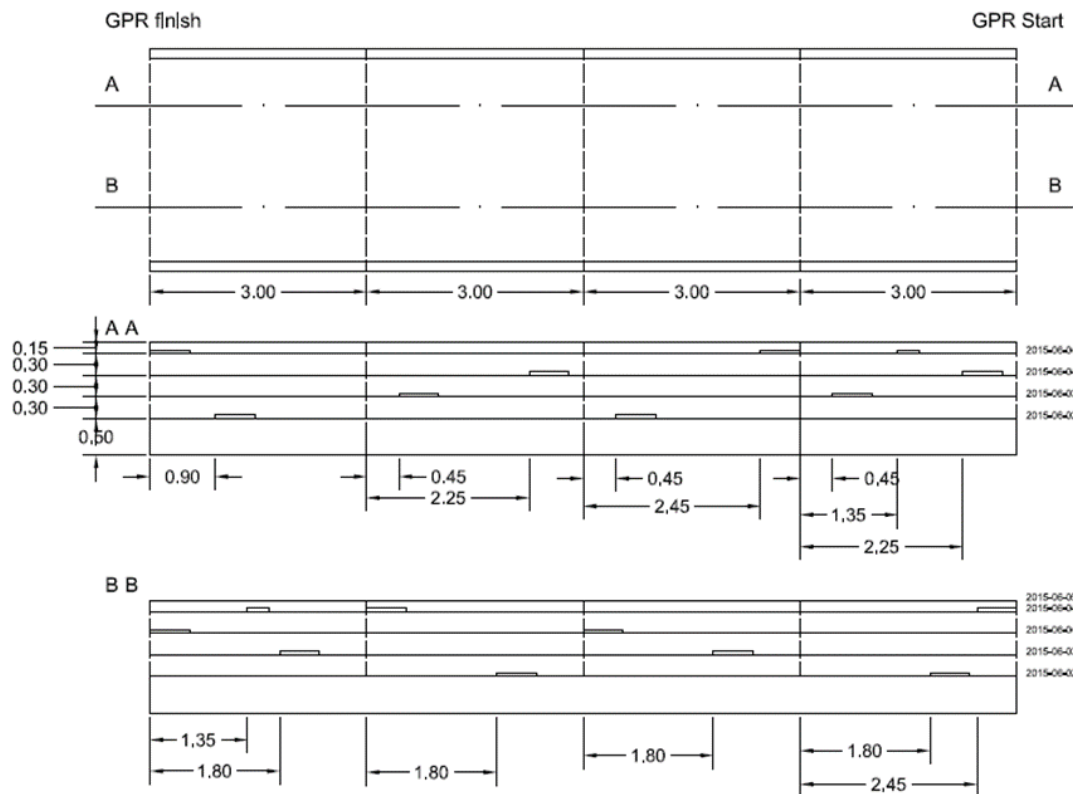
FIG. 2 – Map of the inspected area and configuration of metal plates disposed in the subgrade.

2.2   TASK 2: MEASUREMENT OF LAYER THICKNESS

The experimental activities were carried out in the test site shown in Figure 3. Three different railway substructures are present in this test pit structure. They were suitably modified to serve the purposes of this study. In particular, the test site is divided into two sections: one of them has a square area of 4.0 m × 4.0 m and a depth of 2.80 m, with concrete floor and walls (concrete pit section); the other section is rectangular with a 4.0 m × 6.0 m area and a 2.60-m depth. In order to ensure a homogeneous subgrade, the existing materials were excavated and replaced with new ones. As shown in Figure 4, three different infrastructure solutions were implemented (Cells 2 to 4), where various non-conventional railway substructures using asphalt sub-ballast were constructed, instead of conventional structures using granular sub-ballast.

FIG. 3 – Test site at LNEC, for task 2.
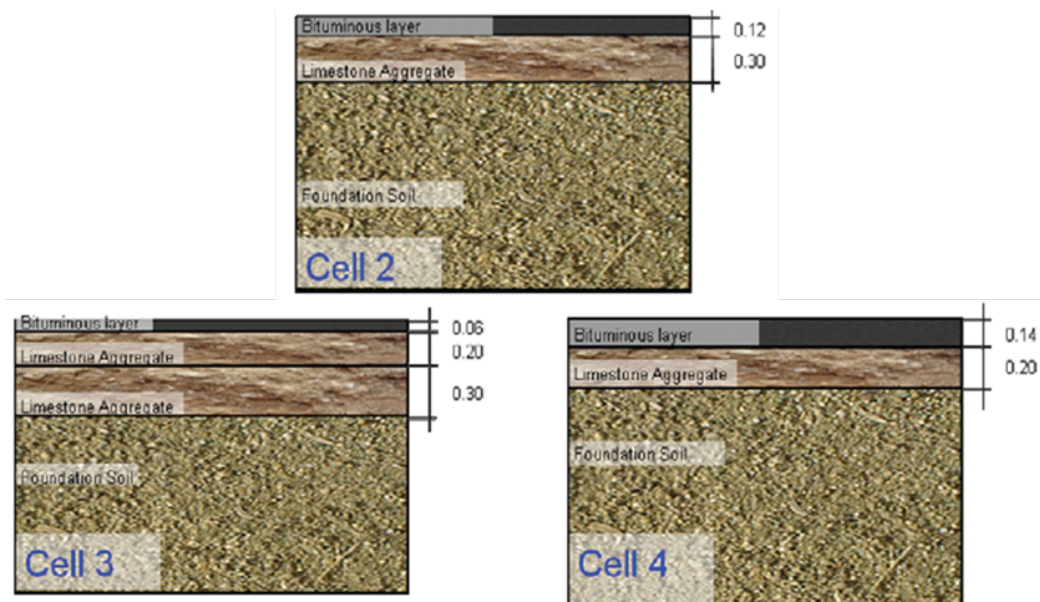
FIG. 4 – Test-site sections of the three Cells.

2.3   TASK 3: EVALUATION OF THE FOULING LEVEL OF BALLAST.

Different conditions of ballast were simulated to study how they affect the measured GPR signal. In particular, data gathered on new ballast

were compared to data gathered on old or used ballast. Moreover, the influence of fouling conditions as well as of water content was studied.

Firstly, two specimens (Boxes 1 and 2) were built and the dielectric constant was estimated for both the new and used (old) ballast (see Figure 5). The material was compacted with a VIBRO-VERKEN system by applying a weigh of 57 Kg with 2850 pulses/min for a total of 2 min. To calibrate the dielectric constants of ballast, each box has two points with controlled height (see Table 1). Moreover, aluminium foil was introduced at the bottom of the boxes to reflect the signal in order to facilitate the thickness measurement.

FIG. 5 – Boxes containing new (left) and used (right) ballast.

Then, two specimens (Boxes 3 and 4) were built to study the influence of fouling and water content on the dielectric constant. New ballast was included in Box 3 and used ballast in Box 4. To simulate fouling, a layer of soil with high level of clays was merged every two consecutive layers of ballast (see Figure 6).

The specimen built to simulate 7.5% of fouling (Box 3) was composed of: 1 layer of ballast + 1.5 kg of soil + 1 layer of ballast + 1.5 kg of soil + 1 layer of ballast + 1.5 kg of soil + 1 layer of ballast + 1.5 kg soil + 1 layer of ballast; the average total height of the specimen resulted equal to about 18 cm.

The specimen built to simulate 15% of fouling (Box 4) was composed of: 1 layer of ballast + 3 kg of soil + 1 layer of ballast + 3 kg of soil + 1 layer of ballast + 3 kg of soil + 1 layer of ballast + 3 kg of soil + 1 layer of ballast. The average total height of the specimen resulted equal to about 18 cm.

These two specimens were compacted, same as Boxes 1 and 2, and their final configuration is described in Table 1.

TABLE 1 – MAIN PROPERTIES OF THE SPECIMENS:
TYPE OF BALLAST, FOULING AND WATER CONTENT.

Specimen	Characteristics	Control points		Fouling	Water content
		1	2		
Box 1	New ballast	17 cm	18 cm	0%	----
Box 2	Used ballast	17 cm	18 cm	0%	----
Box 3	New ballast	17 cm	18 cm	7.5 %	5.5%
					10%
					14%
Box 4	Used ballast	17 cm	17 cm	15%	5.5%
					10%
					14%

FIG. 6 – Distribution of soil between two consecutive layers of ballast.

The initial water content of the soil was measured. A sample of soil was dried for one day at 104º, which resulted in 5.5% of water content. The wet and dried weights of the sample were 245.38 g and 231.76 g, respectively. Different water contents were then considered: as described in Table 2, different quantities of water were scattered in the Boxes 3 and 4 (see Figure 7) to reach water content levels of 10% and 14%. The purpose of such tests was to simultaneously study the effect of fouling and water content. Better results can be obtained by using larger boxes.

TABLE 2 – PROPERTIES OF SPECIMENS USED TO SIMULTANEOUSLY ANALYSE FOULING AND WATER CONTENT EFFECTS.

Specimen	Characteristics	Fouling	Water content	Water [kg]
Box 1	New ballast	0%	----	----
Box 2	Used ballast	0%	----	----
Box 3	New ballast	7.5%	5.5%	----
			10%	0.54
			14%	+0.48
Box 4	Used ballast	15%	5.5%	----
			10%	0.27
			14%	+0.24

FIG. 7 – Introduction of water in the specimens.

3. METHODS

3.1 TASK 1: DETECTION OF TRACK DEFECTS AT INFRASTRUCTURE LEVEL

When using the ground-coupled system, data were recorded with a trace-interval of 0.01 s. Marks were taken when collecting data, to subsequently correlate them with those measured by the air-coupled system.

When using the air-coupled system, data were recorded with a trace-interval of 1.0 cm.

Additionally, a Falling Weight Deflectometer (FWD) (see Figure 8 – upper panel) was used to evaluate the bearing capacity of the subgrade. The thicknesses obtained from GPR data were combined with deflections measures with FWD, to produce the structural models of the subgrade layers. For a given thickness, the deflection values is higher if the elastic moduli of the subgrade is lower, which could be interpreted as an anomalous zone and can be due to cracking, interlayer debonding or construction failures.

Light Falling Weight Deflectometer (LFWD) measures were also performed (see Figure 8 – lower panel), to add more information and further validate the interpretation of the damaged areas identified by GPR and FWD.

Finally, in order to corroborate the joint interpretation of GPR-FWD-LFWD data, drill cores were extracted in the detected damaged areas (see Figure 9).

3.2 TASK 2: MEASUREMENT OF LAYER THICKNESS

The purpose of the tests was to analyse the accuracy of the GPR systems used in this STSM for thickness measurement. Different GPR systems and antenna configuration were employed (see Figure 10). Different methodologies were considered to gather data and characterize the asphalt (first bituminous layer in Figure 4).

The ground-coupled system was equipped with antennas having central frequencies of 1 GHz and 2.3 GHz. During data acquisition, the antennas were moved along the surface line and data were recorded in both static and dynamic modes.

The air-coupled system was equipped with antennas having central frequencies of 1 GHz and 1.8 GHz. The antennas were at about 45-50 cm from the inspected surface. Also in this case, data were acquired in both static and dynamic modes.

Table 3 resumes the data acquisition settings.

FIG. 8 – Upper panel: Portable FWD. Lower panel: LFWD.

FIG. 9 – Extraction of drill cores.

TABLE 3 – CONFIGURATIONS USED FOR DATA ACQUISITION.

Antennas		**Ground-coupled**		**Air-coupled**	
Frequency [GHz]		**1.0**	**2.3**	**1.0**	**1.8**
Time windows [ns]		43	14	20	12
Samples/scan		500	292	1024	1024
Trace-interval	Dynamic mode [cm]	0.02	0.02	0.02	0.02
	Static mode [s]	0.02	0.02	---	---
	Static mode [Scans/s]	---	---	60	60

The static data were used to calibrate the velocity of propagation of the GPR signal in asphalt; the dynamic data allowed for a comparison between methodologies. For each system, two different GPR lines were acquired by distance in all the cells (see Figure 4). The static data were gathered at two control points on each profile line. After surveying, drill cores were extracted through the bituminous layer at these control points to proceed with calibration (see Table 4).

Two different methodologies were employed to calibrate the velocity of propagation and to measure thicknesses, as described in the following.

FIG. 10 – Data acquisition. Upper panel: ground-coupled system with 1.0 GHz (right) and 2.3 GHz (left) antennas. Lower panel: air-coupled system with 1.0 GHz and 1.8 GHz antennas.

Coring – for both ground-and air-coupled antennas.

Knowing the thickness of the layers (*d*) from coring and the travel time difference (*twt*) to and from the target, the velocity of propagation (*v*) can be derived from Equation (1). Next, the relative dielectric constant (*ε*) can be obtained from Equation (2).

$$d = v \frac{twt}{2} \tag{1}$$

$$\varepsilon = \left(\frac{c}{v}\right)^2 \tag{2}$$

where c is the free-space velocity (0.3 m/ns).

TABLE 4 – THICKNESSES OF THE BITUMINOUS LAYER (AT THE CONTROL POINTS) OBTAINED FROM CORING

Cell	Line	Control point	Thickness [m]
2	3	3.1	0.112
		3.2	0.115
	4	4.1	0.116
		4.2	0.115
3	5	5.1	0.064
		5.2	0.055
	6	6.1	0.055
		6.2	0.053
4	7	7.1	0.133
		7.2	0.134
	8	8.1	0.135
		8.2	0.128

Metal plate – for air-coupled antennas, only.

By knowing the amplitudes of the reflected pulses (with and without the metal plate) and their arrival times, it is possible to estimate the dielectric constant and thickness of a layer.

The first step in the process is determining the dielectric constant. The amplitude of the incident GPR signal and the amplitude of the layer return are necessary for the calculations. In particular, the amplitude of the incident GPR signal can be determined by collecting data over a large flat metal plate, placed on the surface to be inspected, and by measuring the amplitude of the reflected signal. Because metal is a good conductor, it can be considered as a perfect reflector: hence, the amplitude of the reflected signal can be considered equal to the amplitude of the incident signal. The relative dielectric constant of the first layer of the inspected structure is given by:

$$\varepsilon_a = \left[\frac{1+\frac{A_1}{A_m}}{1-\frac{A_1}{A_m}}\right]^2 \tag{3}$$

where A_1 is the amplitude of the reflection from the surface, without metal plate, and A_m is the amplitude of the reflection from a large metal plate.

Next, the amplitude profiles are transformed into layer thickness profiles as follows:

$$d = \frac{c\ twt}{\sqrt{\varepsilon}} \tag{4}$$

where the distance travelled by the radar-wave (d) is equal to the thickness of the layer, c is the speed of light, twt is the two-way travel-time distance between two different reflectors (layers), and ε is the relative dielectric constant obtained from Equation (3).

3.3   TASK 3: EVALUATION OF THE FOULING LEVEL OF BALLAST.

Static measurements were carried out at the control points. Data were gathered by using both the ground- and air-coupled systems, with a trace-interval of 0.01 s. The data acquisition with the ground-coupled system was conducted with the antennas in contact with the ballast, without elevation; the air-coupled antennas, instead, were at about 40 cm from the inspected surface.

4.   RESULTS

4.1   TASK 1: DETECTION OF TRACK DEFECTS AT INFRASTRUCTURE LEVEL

In the following radargrams, red rectangles indicate the metal plates and yellow circles are the possible damaged areas.

Location 1: through the middle of the test site (see Figure 2)

The comparison of the 1.0 GHz data obtained with both ground- and air-coupled antennas, presented in Figures 11 and 12, respectively, demonstrates that the ground-coupled system is capable to provide a better resolution, which allows for a better definition of the anomalous zones. In Figure 13, 1.8 GHz data obtained with the air-coupled system are reported. The 2.3-GHz data obtained with the ground-coupled

system and presented in Figure 14(a) have an even better resolution than the 1.0-GHz data of Figure 11.

FWD measurements were carried out in the same positions where the GPR profiles were recorded, in the middle of the experimental area.
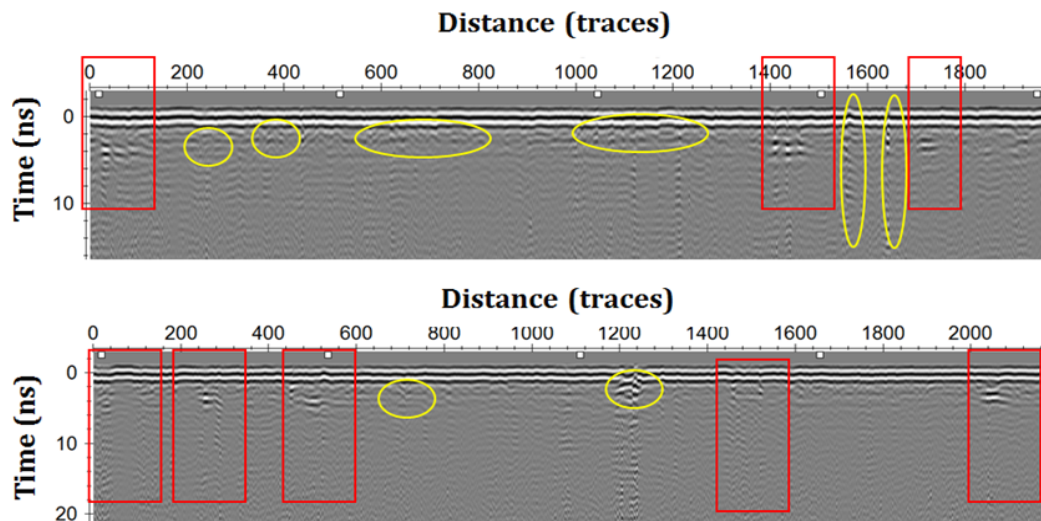
FIG. 11 – 1.0 GHz data obtained with the ground-coupled system.
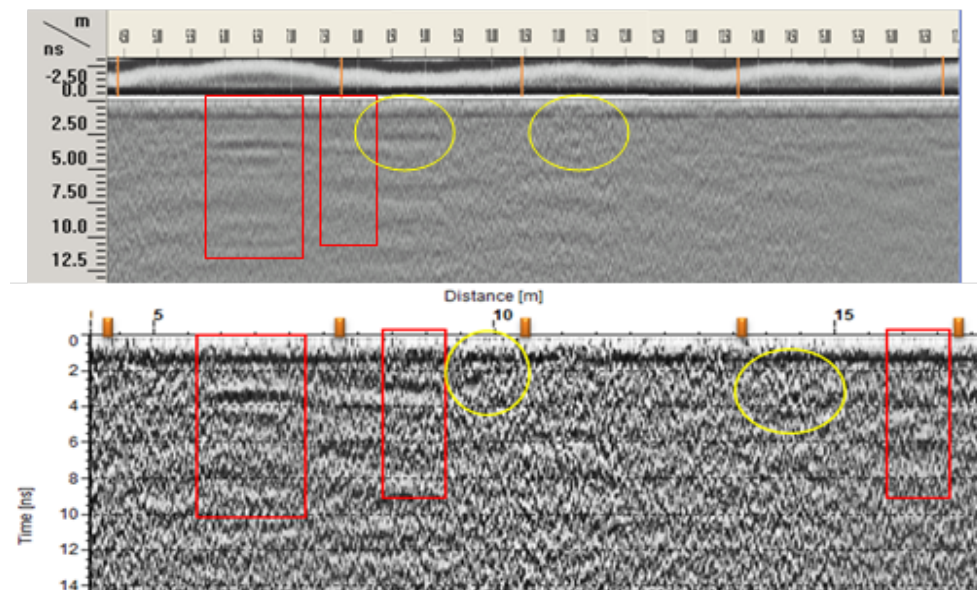
FIG. 12 – 1.0 GHz data obtained with the air-coupled system.
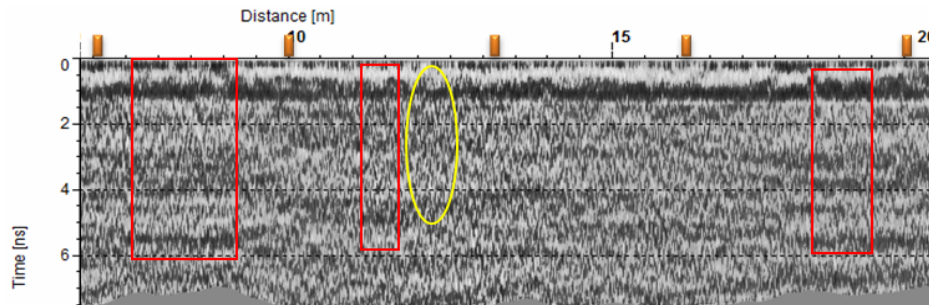
FIG. 13 – 1.8 GHz data obtained with the air-coupled system.
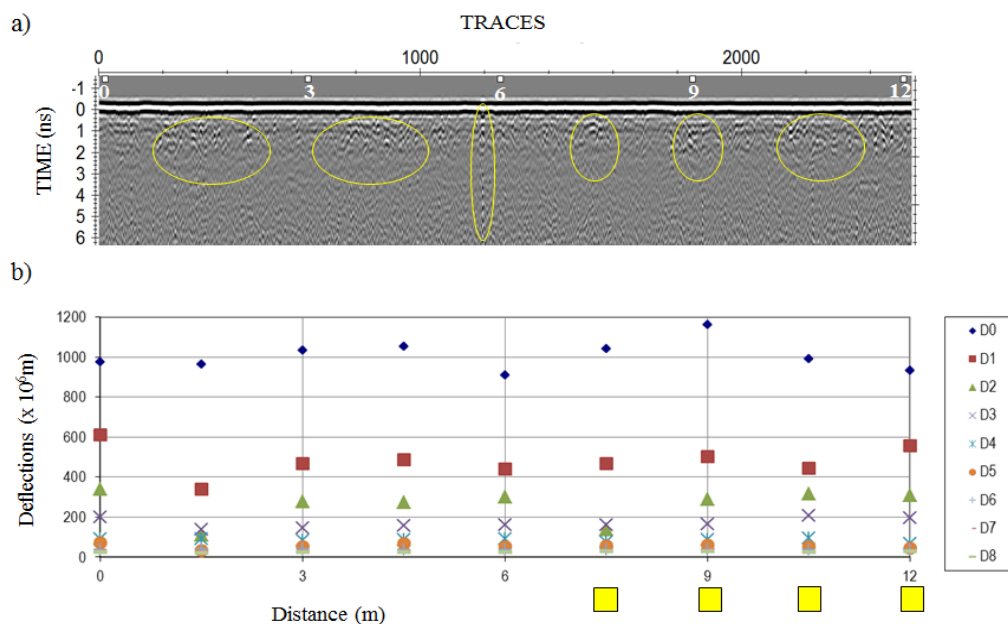
FIG. 14 – (a) 2.3 GHz data obtained with the ground-coupled system, and (b) deflections produced by FWD (yellow squares indicate where drill cores were extracted).

In Figure 14(b), it can be observed that the places representing more noise correspond to FWD results with anomalous deflections. For example, at positions 1.5 m and 7.5 m, there is a difference in deflection trend D3 higher than D2. In almost all the points, see position 9.0 m, there is a small difference between D0 and D1. The anomalies can be due to cracking on the soil top layer (9.0 m) or even in the layer beneath (1.5 m and 7.5 m), or to debonding. The only two positions that present better continuity of the deflections are 0.0 and 12.0 m. This means that

the load transmission is better and so the continuity of the layer is better (or else there is a lower cracking).

By comparing FWD data with 2.3-GHz data in Figure 15(a), it was corroborated the good agreement between the methods when identifying both anomalous deflections and reflections. The anomaly identified at 7.5 m was also detected in the 1.0-GHz data produced by the air-coupled system (Figure 13). This interpretation is more detailed in the graphics reported in Figure 15.
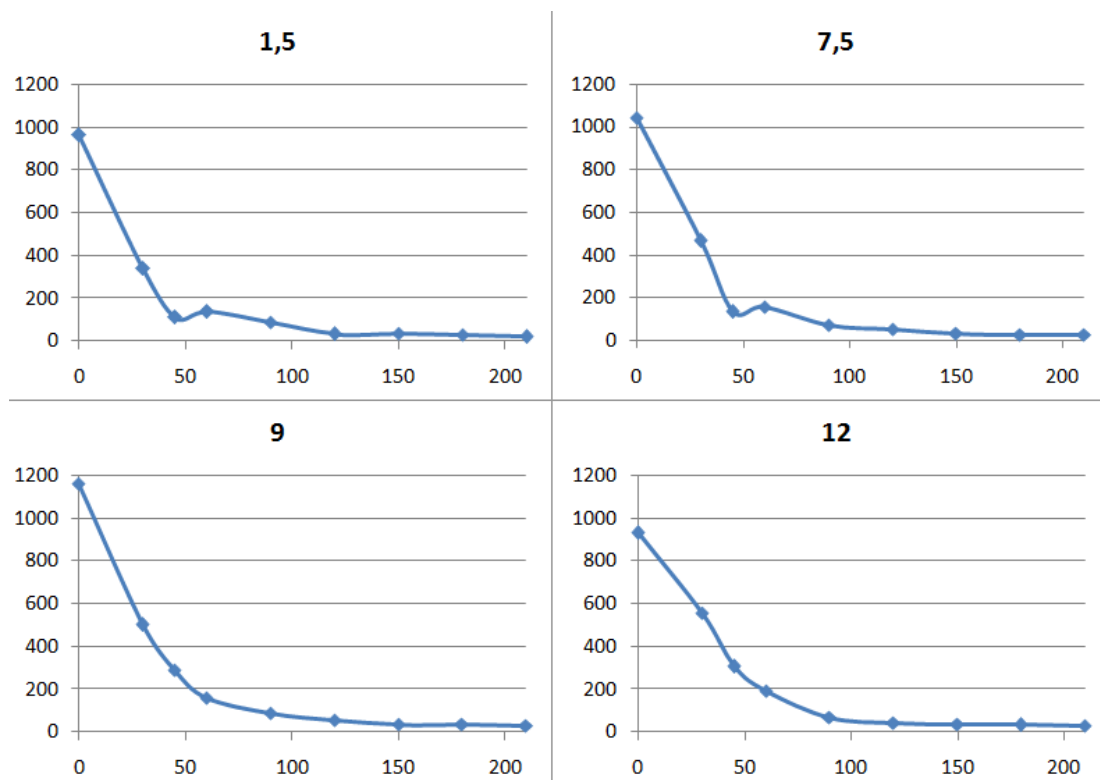
FIG. 15 – Graphics from FWD data, showing the most affected areas.

LFWD measures were performed to further validate the interpretation of the damaged areas achieved from GPR and FWD methods. Figure 16 presents the LFWD data obtained through the middle of the test site, which corroborate the existence of anomalies or damaged zones at 1.5 m, 7.5 m and 9.0 m - 10.5 m positions.

Finally, coring was performed in the areas showing the most apparent anomalies (7.5 m, 9.0 m and 10.5 m). In addition, a drill core was

extracted in a position where no anomalies were detected (12.0 m). The positions of such cores are illustrated by yellow squares in Figure 14(b). Figure 17 shows the drill cores extracted. The core extracted at 7.5 m presents severe cracking in the subgrade, while the one extracted at 9.0 m shows defects between layers (delamination).
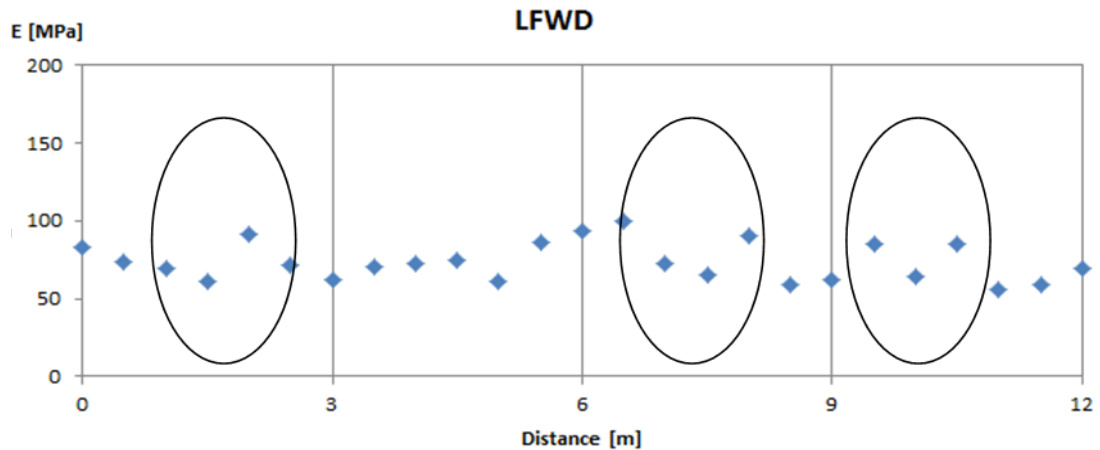
FIG. 16 – Deflections obtained from LFWD.
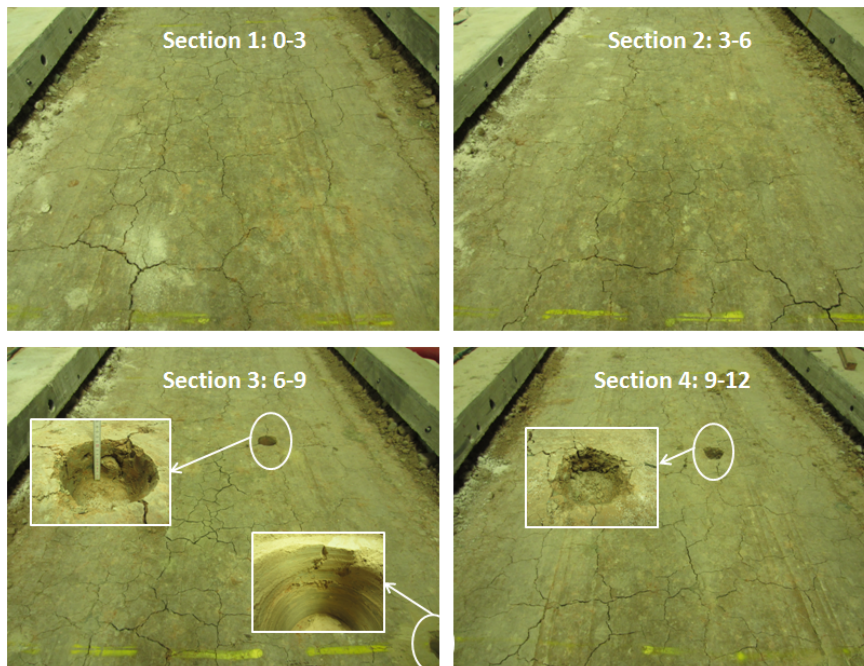
FIG. 17 – Drill cores extracted at positions 7.5 m, 9.0 m and 10.5 m shown in Figure 14.

FIG. 18 – Drill core extracted at 12.0 m, where no anomalies were detected.

Location 2: through the right side of the test site (B in Figure 2)

The GPR results that we obtained are presented in Figures 19-22.

Location 3: through left side of the test site (A in Figure 2)

A selection of GPR results is presented in Figures 23 and 24.

Through this series of experiments, it was demonstrated that ground-coupled systems present clear advantages compared to air-coupled systems: they provide deeper signal penetration and better vertical resolution, thus allowing to detect fine details, such as cracking.
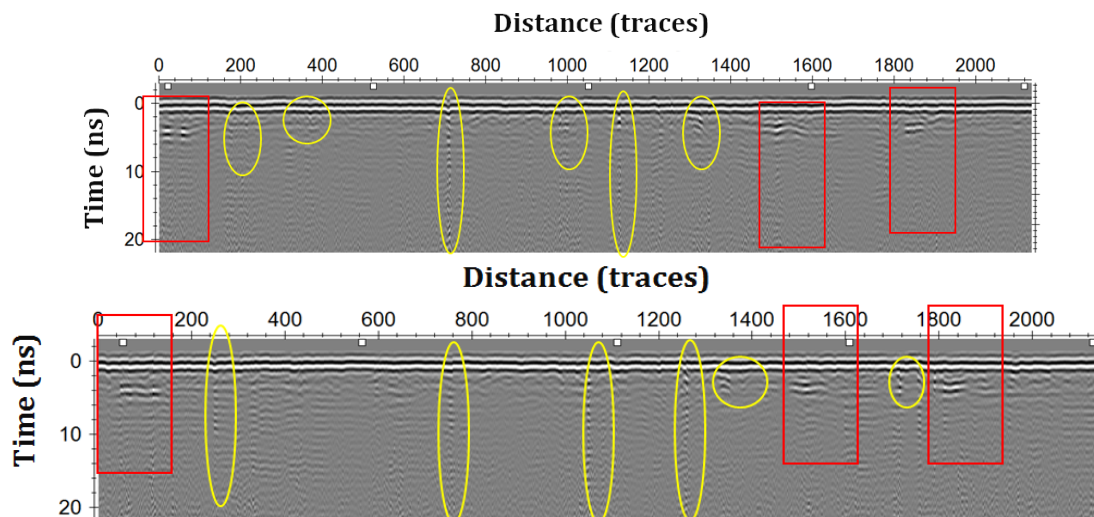
FIG. 19 – 1.0 GHz data obtained with the ground-coupled system.
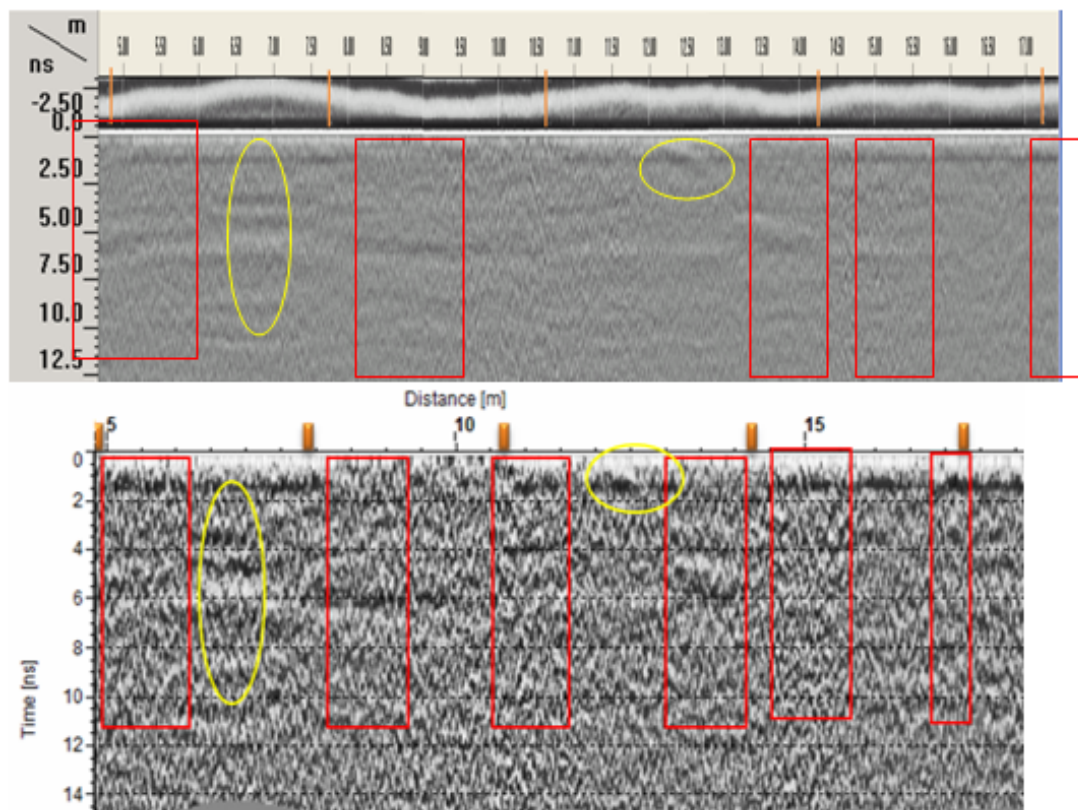
FIG. 20 – 1.0 GHz data obtained with the air-coupled system.
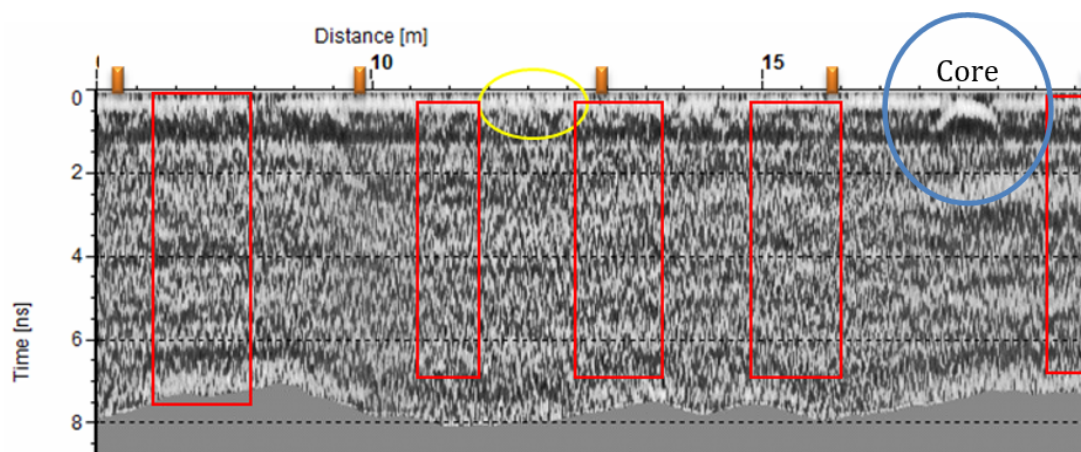
FIG. 21 – 1.8 GHz data obtained with the air-coupled system.
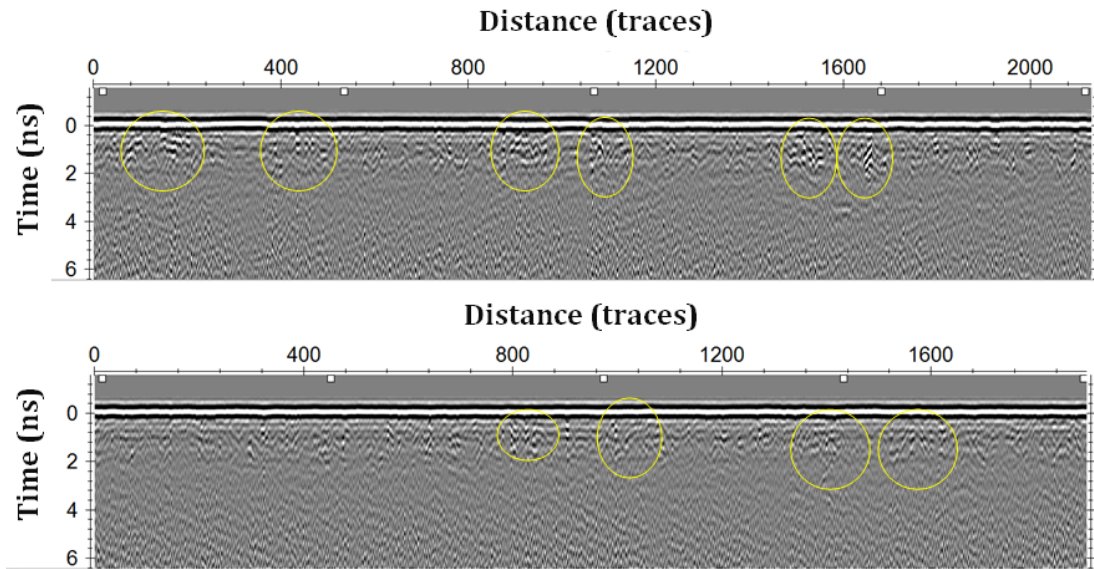
FIG. 22 – 2.3 GHz data obtained with the ground-coupled system.
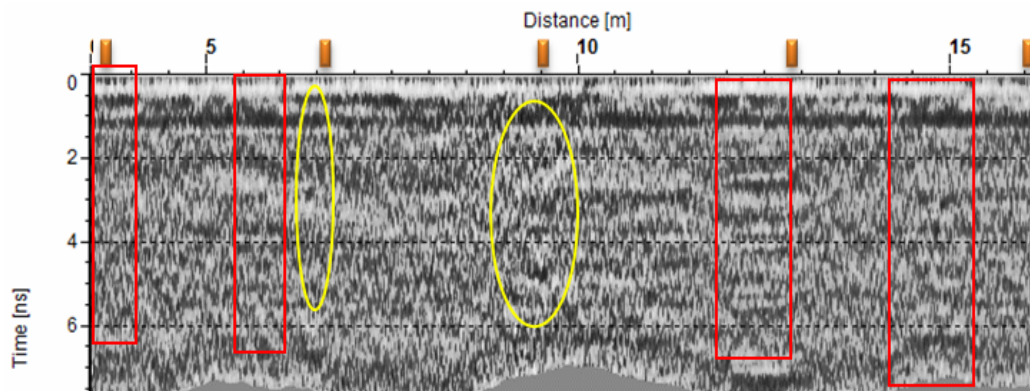
FIG. 23 – 1.8 GHz data obtained with the air-coupled system.
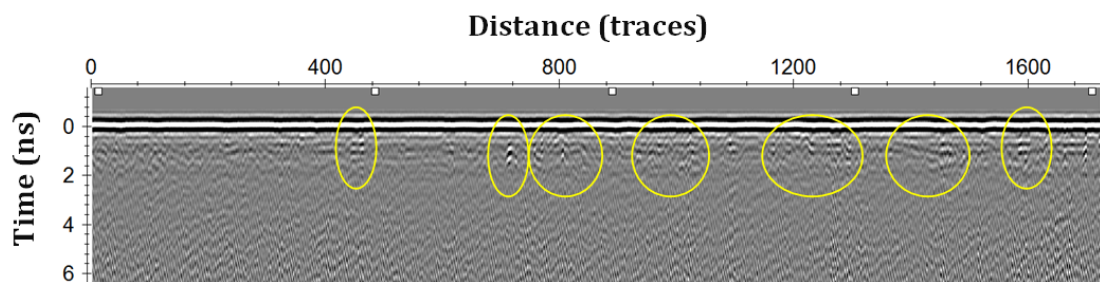
FIG. 24 – 2.3 GHz data obtained with the ground-coupled system.

4.2 TASK 2: MEASUREMENT OF LAYER THICKNESS

Bituminous thicknesses obtained by using the coring method

Tables 5 and6 show the dielectric constants and velocities obtained from the coring method for the first bituminous layer in Figure 4. For both ground- and air-coupled systems, these values were obtained from Equations (1) and (2) and by using the static data acquired at each control point of the three different cells.

Table 5 describes the dielectric constants and velocities of propagation obtained for the ground-coupled system (frequencies of 1.0 GHz and 2.3 GHz). The velocities obtained range from 0.121 m/ns to 0.137 m/ns, resulting in average values of 0.125 m/ns, 0.130 m/ns and 0.133 m/ns for Cells 2, 3 and 4, respectively.

Table 6 presents values obtained with the air-coupled antennas (frequencies of 1.0 GHz and 1.8 GHz). For the GSSI system, the velocities obtained range from 0.112 m/ns to 0.130 m/ns and average velocity values for Cells 2, 3 and 4 of 0.117 m/ns, 0.124 m/ns and 0.12 m/ns, respectively.

By comparing the dielectric constants obtained from both systems, it can be observed that the ground-coupled system provides lower values than the air-coupled system.

Knowing the velocity of propagation of the GPR signal in asphalt, the time-distance (ns) profiles obtained from dynamic data acquisition can be converted into thicknesses profiles (m) by using Equation (1).

Bituminous thicknesses obtained using the metal plate method

Table 7 shows the dielectric constants and velocity values obtained by the amplitude or metal plate method with the air-coupled system. As in the case of the coring method, these values were calibrated at each control point of the three different cells by considering static measurements. The dielectric constants were obtained from Equation (3) and, then, the velocities were derived using Equation (2).

The dielectric constants obtained resulted on the order of the values obtained with the ground-coupled system when using the coring method – see Table 5. The velocities obtained range from 0.120 m/ns to

0.137 m/ns with average values of 0.126 m/ns, 0.131 m/ns and 0.128 m/ns for Cells 2, 3 and 4, respectively.

TABLE 5 – VELOCITIES OF PROPAGATION OBTAINED FROM THE CORING METHOD, FOR THE GROUND-COUPLED SYSTEM.

Cell	Line	Control point	Coring Thickness [m]	Velocity [m/ns]		ε	
				1.0 GHz	2.3 GHz	1.0 GHz	2.3 GHz
2	3	3.1	0.112	0.121	0.124	6.1	5.9
		3.2	0.115	0.128	0.126	5.5	5.7
	4	4.1	0.116	0.123	0.123	5.9	5.9
		4.2	0.115	0.126	0.127	5.7	5.6
3	5	5.1	0.064	0.125	0.130	5.7	5.3
		5.2	0.055	0.129	0.129	5.4	5.4
	6	6.1	0.055	0.129	0.134	5.4	5.0
		6.2	0.053	0.137	0.134	4.8	5.0
4	7	7.1	0.133	0.136	0.133	4.9	5.1
		7.2	0.134	0.125	0.128	5.8	5.5
	8	8.1	0.135	0.137	0.137	4.8	4.8
		8.2	0.128	0.136	0.134	4.9	5.0

TABLE 6 – VELOCITIES OF PROPAGATION OBTAINED FROM THE CORING METHOD, FOR THE AIR-COUPLED SYSTEM.

Cell	Line	Control point	Coring Thickness [m]	Velocity [m/ns]		ε	
				1.0 GHz	1.8 GHz	1.0 GHz	1.8 GHz
2	3	3.1	0.112	0.115	0.118	6.8	6.5
		3.2	0.115	0.118	0.116	6.5	6.7
	4	4.1	0.116	0.112	0.119	7.2	6.4
		4.2	0.115	0.117	0.117	6.6	6.6
3	5	5.1	0.064	0.126	0.129	5.7	5.4
		5.2	0.055	0.115	0.130	6.8	5.3
	6	6.1	0.055	0.117	0.123	6.8	5.9
		6.2	0.053	0.118	0.129	6.5	5.4
4	7	7.1	0.133	0.112	0.123	7.2	5.9
		7.2	0.134	0.118	0.117	6.5	6.8
	8	8.1	0.135	0.124	0.129	5.8	5.4
		8.2	0.128	0.115	0.125	6.8	5.7

TABLE 7 – VELOCITIES OF PROPAGATION AND THICKNESSES OBTAINED BY THE
AMPLITUDE METHOD, FOR THE AIR-COUPLED SYSTEM.

Cell	Line	Control point	ε		Velocity (m/ns)		Thickness (m)	
			1.0 GHz	1.8 GHz	1.0 GHz	1.8 GHz	1.0 GHz	1.8 GHz
2	3	3.1	5.6	5.7	0.126	0.126	0.123	0.119
		3.2	5.6	5.9	0.127	0.124	0.124	0.123
	4	4.1	5.8	6.2	0.125	0.120	0.129	0.118
		4.2	5.4	5.4	0.130	0.129	0.128	0.127
3	5	5.1	5.4	5.2	0.129	0.131	0.065	0.065
		5.2	5.4	5.2	0.129	0.131	0.062	0.055
	6	6.1	5.2	5.1	0.132	0.133	0.062	0.059
		6.2	5.3	5.2	0.130	0.132	0.058	0.054
4	7	7.1	5.9	5.3	0.123	0.130	0.147	0.141
		7.2	5.8	5.4	0.124	0.129	0.141	0.148
	8	8.1	5.7	4.9	0.126	0.135	0.137	0.142
		8.2	5.9	4.8	0.123	0.137	0.137	0.140

Next, thicknesses were obtained from Equation (4). Table 8 presents the
thicknesses obtained from the amplitude method. The thicknesses
obtained by the amplitude method (T_{AM}) were compared to the actual
thicknesses obtained from coring (ground truth). The error (%) was
evaluated as the difference between both thicknesses obtained from
each calibration method, at the same control point, and normalized to
the coring measures (T_{COR}) (Equation (5)). A maximum error of 12.7%
was obtained.

$$error\ (\%) = \frac{|T_{AM} - T_{COR}|}{T_{COR}} \cdot 100 \tag{5}$$

Figure 25 presents a comparison between the thicknesses obtained
from both coring and amplitude methods for the GSSI air-coupled
system with the 1.0 GHz antenna. The data represented are the ones
acquired by using the dynamic mode. For the profile line obtained by
the amplitude method, the velocity was calculated for each trace using
Equations (3) and (4). On the other hand, for the coring method, the
average velocities obtained in VII were assumed (0.117 m/ns, 0.124
m/ns and 0.12 m/ns for Cells 2, 3 and 4, respectively).

Although the maximum error in Table 8 was obtained – at this
frequency – for Cell 3, we think that such difference could represent an
isolated result because the complete profiles obtained from the two

TABLE 8 – THICKNESSES OBTAINED BY THE AMPLITUDE METHOD AND COMPARISON
WITH THE THICKNESSES OBTAINED BY CORING.

Cell	Control point	Thickness (m)			Comparison "*amplitude vs coring*"			
		Amplitude method		Coring	Difference (m)		Error (%)	
		1.0 GHz	1.8 GHz		1.0 GHz	1.8 GHz	1.0 GHz	1.8 GHz
2	3.1	0.123	0.119	0.112	0.011	0.007	9.8	6.2
	3.2	0.124	0.123	0.115	0.009	0.008	7.8	6.9
	4.1	0.129	0.118	0.116	0.013	0.002	11.2	1.7
	4.2	0.128	0.127	0.115	0.013	0.012	11.3	10.4
3	5.1	0.065	0.065	0.064	0.001	0.001	1.5	1.5
	5.2	0.062	0.055	0.055	0.007	0.000	12.7	0.0
	6.1	0.062	0.059	0.055	0.007	0.004	12.7	7.3
	6.2	0.058	0.054	0.053	0.005	0.001	9.4	1.9
4	7.1	0.147	0.141	0.133	0.014	0.008	10.5	6.0
	7.2	0.141	0.148	0.134	0.007	0.014	5.2	10.4
	8.1	0.137	0.142	0.135	0.002	0.007	1.5	5.2
	8.2	0.137	0.140	0.128	0.009	0.012	7.0	9.4
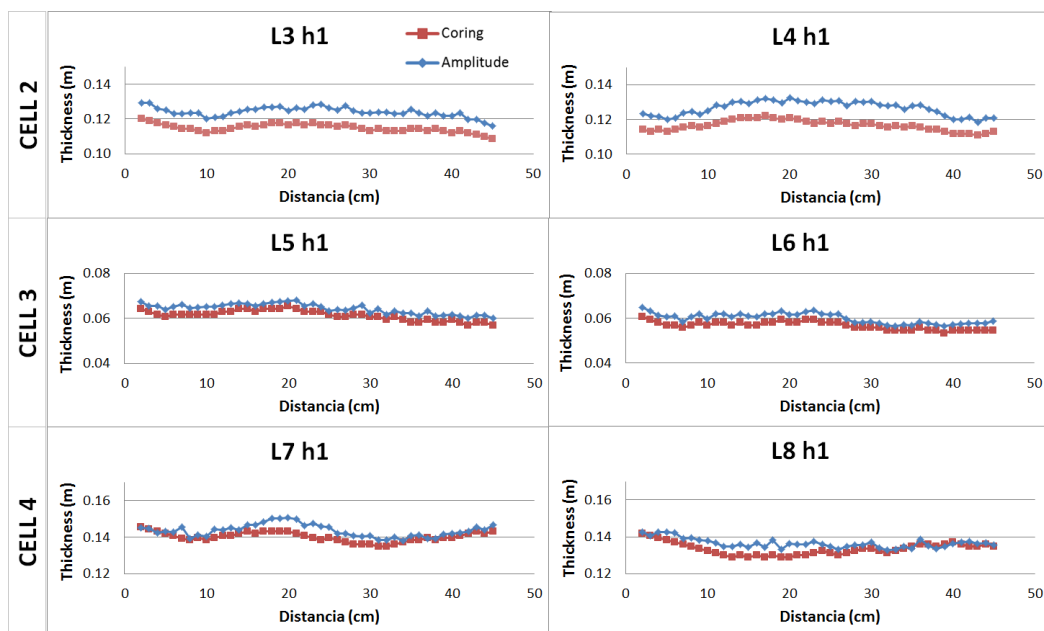
FIG. 25 – Comparison between the thicknesses obtained from both coring and
amplitude methods for the GSSI air-coupled system with the 1.0 GHz antenna.

methods show the best correlation. The maximum differences for thicknesses observed in Lines 3 and 4 are 11.0 mm and 14.0 mm, respectively. For Lines 5 and 6, the maximum differences are 3.0 mm and 4.0 mm, respectively, and for both Lines 7 and 8 the maximum differences are 8.0 mm.

4.3   TASK 3: EVALUATION OF THE FOULING LEVEL OF BALLAST.

Ballast fouling and moisture content are major issues in railway assessment usually leading to settlements of the railway. They can be easily evaluated by GPR as the dielectric value of the ballast increases with the presence of water [1]. This change is particularly relevant on contaminated ballast as the fine soil particles are more susceptible to the increase of water content of the material due to the decrease of drainage capabilities [7].

Some laboratory tests were developed during the STSM presented in this paper, to evaluate the dielectric constants for different levels of fouled ballast (0, 7.5% and 15%). The effect of water content on the dielectric constant was also evaluated, and different water contents were considered: 5.5%, 10% and 14%. For the evaluation, two different GPR systems, with air- and ground-coupled antennas working at different frequencies and manufactured by different companies, were used – same as in the previous sections.

Firstly, the influence of the ballast condition on the dielectric constant was analysed. Table 9 displays the results obtained. Significant differences were not observed between the dielectric constants obtained for new (Box 1) and used (Box 2) ballast, the used ballast gave slightly higher values compared to the new material.

Table 10 shows the results obtained when simulating a fouling ballast of 7.5%, as well as the influence of water content. Different levels of water content were simulated: 5.5%, 10% and 14% - as already mentioned. As expected, the comparison of fouling ballast 0% -Table 9, 7.5% - Table 10 and 15% - Table 11, with 5.5% of water content, has demonstrated that dielectric values increase with the increasing of fouling conditions.

The dielectric constant also increases with the water content. However, the analysis of all the values obtained has revealed that values are more sensitive to the fouling level rather than with the water content. Thus,

Open access | www.GPRadar.eu/journal
Volume 1 | Issue 1 | January 2018

100

Published in Rome, Italy
by TU1208 GPR Association

https://doi.org/10.26376/GPR2018004

the increasing of fouling reflected in a major dielectric constant variation. Different tendencies were found between the different equipment used, and the dielectric constants obtained with a frequency of 1.0 GHz were slightly lower than those obtained with higher frequencies of 1.8 GHz and 2.3 GHz. This behaviour was observed for both air- and ground-coupled antennas. Similar differences were found in [8] between the frequencies of 500 MHz and 900 MHz.

TABLE 9 – DIELECTRIC CONSTANTS OBTAINED FOR NEW (BOX 1) AND OLD (BOX 2) BALLAST WITH 0% FOULING AND 5.5% OF WATER CONTENT.

			Dielectric constant			
			Air-coupled		Ground-coupled	
Fouling (%)	Control point	Box	1.0 GHz	1.8 GHz	1.0 GHz	2.3 GHz
0	1.1	1	4.87	4.64	4.01	3.87
0	1.2	1	4.62	4.55	3.58	3.74
0	2.1	2	5.3	4.7	4.2	3.9
0	2.2	2	4.6	4.7	3.8	3.6

TABLE 10 – DIELECTRIC CONSTANTS OBTAINED FOR NEW BALLAST (BOX 3) SIMULATING 7.5% FOULING AND CONSIDERING DIFFERENT WATER CONTENTS OF 5.5, 10 AND 14%.

				Dielectric constant			
				Air-coupled		Ground-coupled	
Fouling (%)	Water (%)	Control point	Box	1.0 GHz	1.8 GHz	1.0 GHz	2.3 GHz
7.5	5.5	3.1	3	5.5	5.0	4.2	4.5
7.5	5.5	3.2	3	5.1	4.8	4.4	3.7
7.5	10	3.1	3	5.8	5.0	4.6	4.9
7.5	10	3.2	3	5.1	5.0	4.7	4.6
7.5	14	3.1	3	6.2	5.8	5.2	5.1
7.5	14	3.2	3	5.2	5.2	4.7	4.6

TABLE 11 – DIELECTRIC CONSTANTS OBTAINED FOR OLD BALLAST (BOX 4) SIMULATING 15% FOULING AND CONSIDERING DIFFERENT WATER CONTENTS OF 5.5, 10 AND 14%.

| | | | | Dielectric constant | | | |
| | | | | Air-coupled | | Ground-coupled | |
Fouling (%)	Water (%)	Control point	Box	1.0 GHz	1.8 GHz	1.0 GHz	2.3 GHz
15	5.5	4.1	4	6.5	5.9	5.4	4.6
15	5.5	4.2	4	6.0	5.5	5.3	4.3
15	10	4.1	4	6.9	6.5	5.8	5.1
15	10	4.2	4	6.7	6.1	5.9	4.9
15	14	4.1	4	7.1	7.2	6.1	5.7
15	14	4.2	4	7.1	6.8	5.9	5.1

Additionally, the dielectric constants obtained for the increasing fouling conditions and water content, with a central frequency of 1.0 GHz, were different for the two radar systems. The results obtained with the MALÅ system were slightly lower than those obtained with the GSSI system. Although a similar behaviour was observed in Task 2, when estimating asphalt thicknesses, the difference could be also caused by the limited size of the boxes (0.65 m long, 0.2 m high and 0.4 m wide). The transmitted signal could be affected by boundary effects, which are obviously much more significant when the antenna is suspended (air-coupled antennas).

CONCLUSIONS

In this work, we performed a series of experiments to study the Ground Penetrating Radar (GPR) detection of track defects at infrastructure level (voids and cracking) in railways, the measurement of layer thickness, and the evaluation of the fouling level of ballast. We used two different GPR systems, equipped with ground- and air-coupled antennas working at different frequencies. We also combined GPR results with Falling Weight Deflectometer and Light Falling Weight Deflectometer data.

ACKNOWLEDGEMENTS

Open access | www.GPRadar.eu/journal
Volume 1 | Issue 1 | January 2018

102

Published in Rome, Italy
by TU1208 GPR Association

https://doi.org/10.26376/GPR2018004

REFERENCES

[1]   T. R. Sussmann, K. R. Maser, D. Kutrubes, F. Heyns, and E. T. Selig, "Development of Ground Penetrating Radar for railway infrastructure condition detection," Proc. Symposium on the Application of Geophysics to Engineering and Environmental Problems, pp. RBA4–RBA4, 2001.

[2]   C. Esveld, Modern railway track, Zaltbommel, MRT-Productions, 2001.

[3]   E. Berggren, Railway track stiffness: dynamic measurements and evaluation for efficient maintenance, University West, 2009.

[4]   G. Manacorda, D. Morandi, A. Sarri, and G. Staccone, "Customized GPR system for railroad track verification," Proc. Ninth International Conference on Ground Penetrating Radar (GPR 2002), pp. 719–723, 2002.

[5]   S. Fontul, E. Fortunato, and F. De Chiara, "Non-Destructive Tests for Railway Infrastructure Stiffness Evaluation," B.H.V. Topping, Y. Tsompanakis, Stirlingshire, UK, 2011.

[6]   J. P. Hyslip, S. Chrismer, M. LaValley, and J. Wnek, "Track Quality From The Ground Up," Proc. AREMA Conference, Chicago, IL, 2012.

[7]   F. De Chiara, S. Fontul, and E. Fortunato, "GPR Laboratory Tests For Railways Materials Dielectric Properties Assessment," Remote Sensing 6(10), pp. 9712–9728, 2014.

[8]   E. Fortunato, "Renovação de Plataformas Ferroviárias. Estudos Relativos à Capacidade de Carga," Ph.D. Thesis (in Portuguese), Departamento de Engenharia Civil; Porto: Faculdade de Engenharia da Universidade do Porto, 2005.

Open access | www.GPRadar.eu/journal
Volume 1 | Issue 1 | January 2018

103

Published in Rome, Italy
by TU1208 GPR Association

https://doi.org/10.26376/GPR2018004

A practical guide on using SPOT-GPR, a freeware tool implementing a SAP-DoA technique

Simone Meschino[1] & Lara Pajewski[2]

[1] Airbus DS, SAR Systems Engineering, Friedrichshafen, Germany
simone.meschino@gmail.com

[2] Sapienza University of Rome, Department of Information Engineering,
Electronics and Telecommunications, Rome, Italy
lara.pajewski@uniroma1.it

Abstract

This is a software paper, which main objective is to provide practical information on how to use SPOT-GPR release 1.0, a MATLAB®-based software for the analysis of ground penetrating radar (GPR) profiles. The software allows detecting targets and estimating their position in a two-dimensional scenario, it has a graphical user interface and implements an innovative sub-array processing method. SPOT-GPR was developed in the framework of the COST Action TU1208 "Civil Engineering Applications of Ground Penetrating Radar" and is available for free download on the website of the Action (www.GPRadar.eu).

Keywords: Ground Penetrating Radar; Detection and localization of buried structures; Sub-array processing; Direction of arrival algorithms; Matched filter technique.

1. Introduction

SPOT-GPR [1] stands for "Sub-array Processing Open Tool for GPR applications" and is a MATLAB®-based software for the analysis of ground penetrating radar (GPR) profiles, with the main purposes of detecting and localizing targets. The tool comes with a graphical user interface (GUI) and implements an innovative sub-array processing (SAP) method, which exploits smart-antenna and radar algorithms. SPOT-GPR was developed during three Short-Term Scientific Missions (STSMs) funded by European Cooperation in Science and Technology (COST, www.cost.eu) and carried out in the framework of the COST Action TU1208 "Civil Engineering Applications of Ground Penetrating Radar." The software is available for free download on the website of the Action (www.GPRadar.eu).

Open access | www.GPRadar.eu/journal
Volume 1 | Issue 1 | January 2018

104

Published in Rome, Italy
by TU1208 GPR Association

https://doi.org/10.26376/GPR2018005

The input of the software is a GPR profile (otherwise called 'B-scan' or 'radargram' by the GPR community). This is partitioned in sub-radargrams, with just a few traces ('A-scans') per sub-radargram. The multi-frequency information enclosed in each trace is exploited and a dominant direction of arrival (DoA) [2] of the electromagnetic field is calculated for every sub-radargram. All the estimated DoAs are triangulated and a pattern of crossings is obtained, which is more densely populated around target locations. Such pattern is filtered, in order to remove a noisy background of unwanted crossings, and is then processed by applying a statistical procedure. Finally, the number of targets and their positions are predicted. For DoA estimation, SPOT-GPR uses the MUltiple SIgnal Classification (MUSIC) [3] algorithm, in combination with the matched filter technique [4]. A description of the method implemented in SPOT-GPR, including detailled information about its advantages and limits, is found in [1].

SPOT-GPR was successfully tested on GPR synthetic radargrams, generated by using the open-source finite-difference time-domain simulator gprMax [5] (www.gprmax.com). Moreover, it was compared with MATLAB® codes implementing two different methods, with good results: a classical hyperbola analysis based on a minimum mean square error technique [6] (see [1]), and an advanced algorithm for the localization of hyperbola apexes and characteristic points based on artificial neural networks and pattern recognition [7-9] (this comparison is not yet published at the time when this paper is written).

The present paper aims to provide practical information on how to use SPOT-GPR and includes some examples. It is advised to read [1] before reading the following sections of this paper and using the software.

2. DESCRIPTION OF THE SOFTWARE

As mentioned in the introduction, SPOT-GPR needs to receive a radargram as main data input, i.e., a set of N traces. The software gives the following output:

1. A plot of the radargram.
2. A plot of the compressed Fast Fourier Transform (FFT) of the radargram, over the signal bandwidth, showing the compressed frequency-content of the field measured by the GPR.

Open access | www.GPRadar.eu/journal
Volume 1 | Issue 1 | January 2018

105

Published in Rome, Italy
by TU1208 GPR Association

https://doi.org/10.26376/GPR2018005

3. An interactive "crossing pattern" that allows the user estimating the number of targets and their coordinates in a two-dimensional scenario (horizontal position and burial depth).

The approach implemented in SPOT-GPR is schematized in Figure 1.

In the field of smart antennas, DoA techniques are used to estimate the number of incident signals impinging over an antenna array, along with their arrival directions. A SAP approach is adopted for the DoA-based detection of electromagnetic sources lying in the near field of an antenna array. In particular, the array of N receivers is partitioned in M sub-arrays, so that the sources can be assumed to be locally planar at each sub-array. Then, by applying DoA estimation algorithms, it is possible to predict the dominant direction of the incoming signal at each sub-array. By triangulating all the DoAs estimated by the sub-arrays, a pattern of crossings can be obtained. This pattern can be filtered in order to remove a noisy background of unwanted crossings and a subset of crossings $\{x,y\}_k$ can be extracted, with $k = 1,\dots K$, where K is the number of crossings. Subsequently, the number of sources and their positions can be estimated, by averaging the coordinates of clustered crossings.
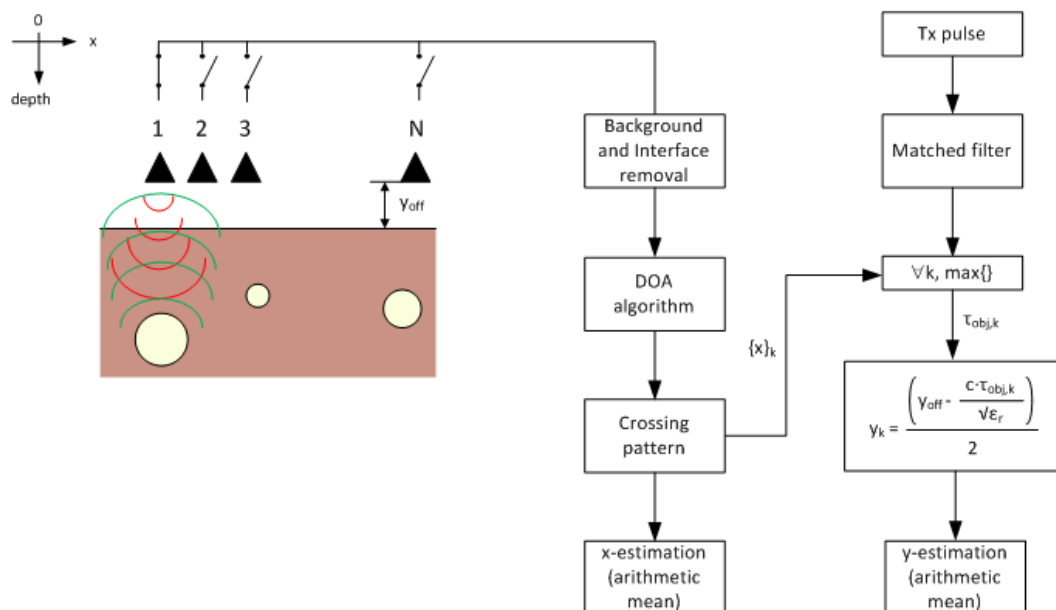
FIG. 1 – Geometry of the GPR scenario and signal-processing block diagram, illustrating the method implemented in SPOT-GPR.

Open access | www.GPRadar.eu/journal
Volume 1 | Issue 1 | January 2018

106

Published in Rome, Italy
by TU1208 GPR Association

https://doi.org/10.26376/GPR2018005

In the scenario that we considered (namely, the use of a SAP-DoA approach for the interpretation of GPR radargrams acquired over a soil or structure), the situation is similar. The electromagnetic sources are the currents induced on the sought targets and DoA algorithms can provide information about where the electromagnetic field back-scattered by the targets comes from.

In order to work in near-field conditions, the radargram to be analysed has to be partitioned in sub-radargrams of suitable size (SAP approach); then, a dominant DoA is predicted for each sub-radargram. The estimated angles are triangulated, thus obtaining a set of crossings with intersections condensed around object locations. This pattern is filtered, in order to remove the unwanted crossings and according to the desired fals-alarm rate. The horizontal coordinates of the crossings, $\{x\}_k$, are processed by using a SAP-DoA approach without pulse compression. For each x_k, the nearest A-scan is then compressed in the time domain, by exploiting information about the pulse emitted by the GPR. Afterwards, the time instant value corresponding to the maximum of the pulse-compressed signal $\tau_{obj,k}$ is extracted and the y-coordinate (depth) is estimated for the k-th crossing. When all the crossings of the pattern have been processed, the (x,y) position of each target is calculated by a simple coordinate average.

The SPOT-GPR archive, downloadable from the TU1208 website, includes the files listed and described in Table 1. Moreover, the package includes a folder called "input" where some datasets are stored: they can be used to familiarize with the software.

The layout of the GUI, before executing the software, is shown in Fig. 2(a). It includes three main sections, corresponding to three steps to be done by the user in order to obtain the estimation of target positions:

Step-1. **Load input files**: the user is required to select the relevant input files (background, simulation, Tx-pulse). More details about the content of such files and required format are given in Subsection 2.1.

Step-2. **Settings**: the user is required to encode the simulation settings, as described in Subsection 2.2.

Step-3. **Spotting**: by interactively drag the mouse on the spotting figure, the user will extract the estimated positions of the targets,

Open access | www.GPRadar.eu/journal
Volume 1 | Issue 1 | January 2018

107

Published in Rome, Italy
by TU1208 GPR Association

https://doi.org/10.26376/GPR2018005

calculated by the software from the coordinates of the crossings included within the selected area, as described in Subsection 2.3.

The three steps of the procedure have to be performed consecutively and in the order that we outlined.

TABLE 1 – SPOT-GPR PACKAGE FILES.

DESCRIPTION	INPUT	OUTPUT
File Name: COST_DOA_main.fig		
GUI main figure, used by the GUI main code	*None*	*None*
File Name: COST_DOA_main.m		
GUI main code	*None*	*None*
File Name: COST_DOA_init_status_flag.m		
Function for the inizialization of variables	*None*	*None*
File Name: COST_DOA_bscan2D.m		
B-scan plot function	*B-Scan data*	*B-scan plot*
File Name: COST_DOA_fft.m		
B-scan FFT c*alculation and plot function*	*Electric-field values, interpolation factor*	*FFT plot*
File Name: COST_DOA_sel.m		
SAP-DoA evaluation for each sub-array	*Angular scan resolution, number of sub-arrays, number of elements per sub-array, steering vector, correlation matrix*	*DoA vector for each preferred DoA method (only MUSIC is implemented in release 1.0)*
File Name: COST_DOA_code.m		
Function that builds the SAP-DoA crossing pattern, by triangulating DoAs, and filters the noise	*None - For release 1.0 the input parameters of this function are freezed and not editable in the GUI*	*x-y coordinates of the crossings composing the refined crossing pattern*
File Name: COST_DOA_cross_centre_estim.m		
Target localization function	*Rectangular area containing crossings to be considered (dragged by user)*	*Target position estimation*
File Name: logo_COST.png		
COST logo	*None*	*None*

Open access | www.GPRadar.eu/journal
Volume 1 | Issue 1 | January 2018

108

Published in Rome, Italy
by TU1208 GPR Association

https://doi.org/10.26376/GPR2018005
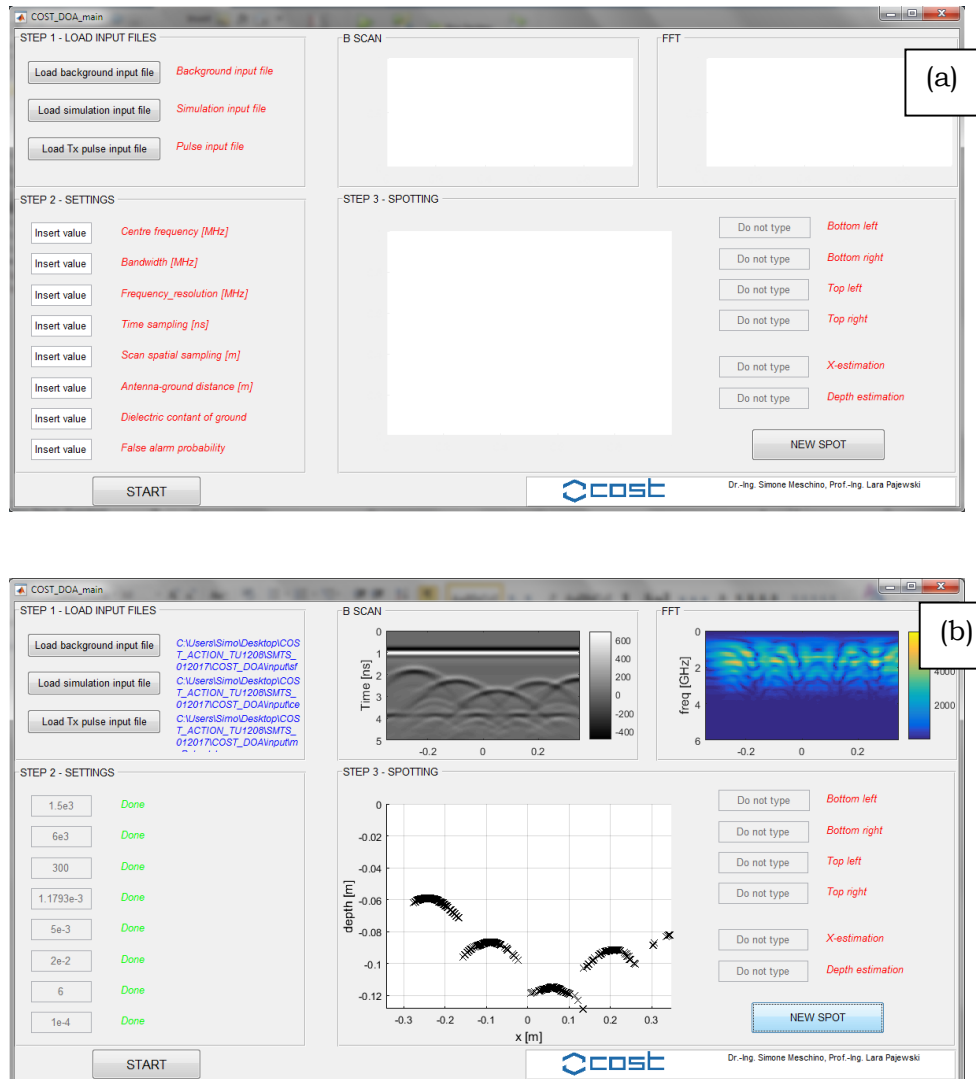
FIG. 2 – Layout of the COST_DoA GUI (release 1.0) (a) before and (b) after executing the software.

The layout of the GUI after executing the software is shown in Figure 2(b) and consists of:

- A grey-scale map of the synthetic or experimental radargram.
- A colour map of the FFT of the compressed radargram.
- The spotting interactive panel, where the user can select an area by simply dragging a rectangular region with the mouse. The relevant estimation of the target position is provided by the software in the dedicated box, on the right.

2.1. STEP 1: LOAD INPUT FILES

The "Step 1: LOAD INPUT FILES" panel is shown in Figure 3. Initially, each loading button is accompanied by a short description of the required file, in red. Such description disappears when the file is selected (and is replaced by the file path, in blue). Three files are required:

- Background input file (electric field amplitude measured by the GPR in the absence of the targets).
- Simulation input file (radargram).
- Tx-pulse input file (pulse emitted by the GPR).

The input files have to be formatted as described hereafter, and have to be saved as .txt text files.
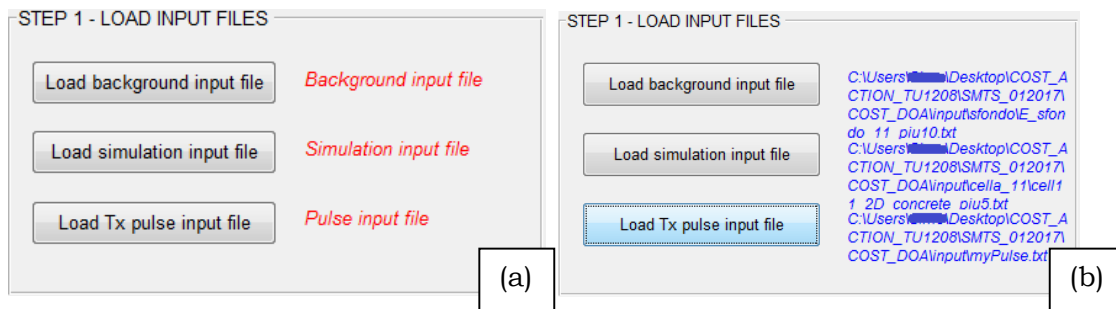
FIG. 3 – Step 1: Load input files: a) Before selection and b) after the files have been selected.

BACKGROUND INPUT FILE FORMAT (.TXT)

The SPOT-GPR tool is based on the two-dimensional geometry sketched in Fig. 1, where objects of arbitrary sections are embedded in a host medium. The background input file is a matrix of real values representing a collection of N traces that would be measured by the GPR in the absence of the targets (N has to be equal to the number of traces included in the radargram that the user wants to process).

The background input file can be produced by using an electromagnetic simulator, else it can be built from experimental data (the user can select in the B-scan a few traces measured in an area where, for sure, no targets are present; such traces can be averaged and the resulting trace can be repeated N times, to build the background input file).

Open access | www.GPRadar.eu/journal
Volume 1 | Issue 1 | January 2018

110

Published in Rome, Italy
by TU1208 GPR Association

https://doi.org/10.26376/GPR2018005

Let us assume that each trace composing the radargram is a vector of T real values. Then, the background input file is a matrix of T × N real values. Such matrix has to be saved as a .txt file, formatted in the following way:

(v1,1)space(v1,2)space(v1,3)space(v1,3)space(v1,5)...space(v1,N)

(v2,1)space(v2,2)space(v2,3)space(v2,3)space(v2,5)...space(v2,N)

...

(vT,1)space(vT,2)space(vT,3)space(vT,3)space(vT,5)...space(vT,N)

Additional spaces (vertical or horizontal) or text are not allowed. An example of background input file is given in Figure 4.
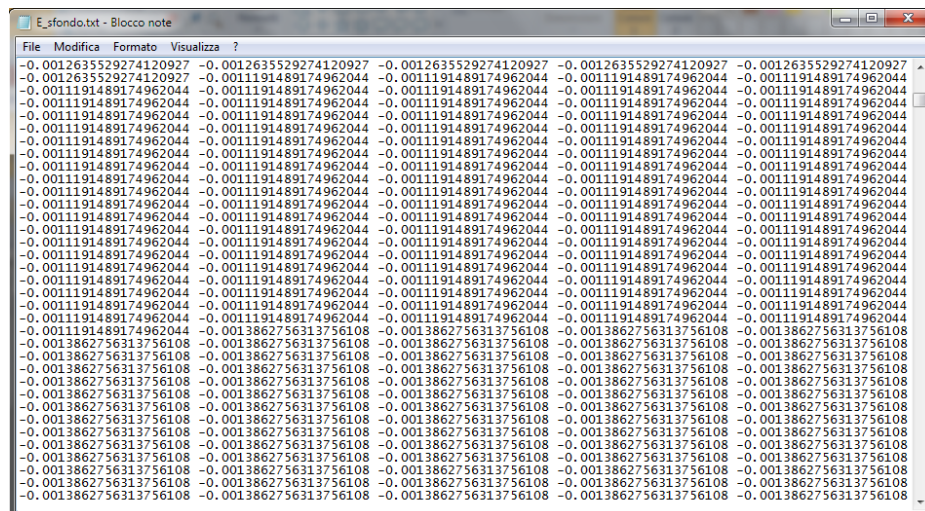
FIG. 4 – Background input file format – example.

SIMULATION INPUT FILE FORMAT (.TXT)

The so-called simulation input file contains the synthetic or experimental radargram that the user is willing to process, with N traces. Each trace is a vector of T real values. Hence, the simulation input file is a matrix of T × N real values. Such matrix has to be saved as a .txt file, formatted in the following way:

(v1,1)space(v1,2)space(v1,3)space(v1,3)space(v1,5)...space(v1,N)

(v2,1)space(v2,2)space(v2,3)space(v2,3)space(v2,5)...space(v2,N)

...

$$(vT,1)space(vT,2)space(vT,3)space(vT,3)space(vT,5)...space(vT,N)$$

Additional spaces (vertical or horizontal) or text are not allowed.

PULSE INPUT FILE FORMAT (.TXT)

The pulse input file contains a vector of T' samples of the pulse emitted by the GPR. The vector has to be saved as a .txt file, formatted in the following way:

$$(v1,1)space(v1,2)space(v1,3)space(v1,4)...space(v1,T)$$

Additional spaces (vertical or horizontal) or text are not allowed.

2.2. STEP 2: SETTINGS

The "Step 2: SETTINGS" panel collects the experimental/simulation GPR settings that were used to generate the input files described in Subsection 2.1. This information is exploited by the SAP-DoA method to provide an estimation of the positions of the targets.

All the relevant settings are described and commented in Table 2.

When a setting parameter is correctly entered, the red-coloured text description abreast turns into the green message "Done" (Figure 5).

After all settings have been entered (and all the red-coloured descriptions turned into a column of green messages), the "START" button below the SETTINGS panel becomes active and the SAP-DoA procedure can be executed.

When the software is executed, the first outputs that appear on the GUI are the grey-scale map of the B-scan and the colour map of the FFT, on top of the main window.

The FFT plot is the collection of the Fourier transformation of all the compressed received pulses. Each trace is cross-correlated, in the time domain, with the Tx-pulse; the output signal (compressed pulse) is then FFT-transformed.

The SAP-DoA method takes more time to return the crossing pattern, which is finally displayed within the SPOTTING panel, as shown in Figure 6(a). The sharper the frequency resolution, the longer it takes. While the SAP-DoA procedure is running, some pop-up messages appear, providing information about the calculation progress status.

Open access | www.GPRadar.eu/journal
Volume 1 | Issue 1 | January 2018

112

Published in Rome, Italy
by TU1208 GPR Association

https://doi.org/10.26376/GPR2018005

2.3. STEP 3: SPOTTING

The user can now select an area of interest in the SPOTTING panel, by dragging a rectangular region with the mouse. The coordinates of the four vertices of the selected region will appear on the GUI, along with the estimated position of the target within the selected region.

When all the red-coloured text descriptions have turned into the green message "Done" (see Figure 6(b)), the spotting (estimation) session is complete. A new spotting session can now be started, by pressing the "NEW SPOT" button, so that a new area of interest can be selected and the position of a new target can be estimated.

2.4. DEMO FILES

A few demo files are available for the user, which can be used to practice with the software. Each file is the .txt properly converted version of the output file obtained by running a gprMax simulation; the considered scenarios are the concrete cells with reinforcing elements studied in [1, 10]. In particular, radargrams for three different concrete cells are given:

1. **cell_11** folder: contains the .txt files for Cell 1.1 (original cell [10] and enlarged cells [1]).
2. **cell_12** folder: contains the .txt files for Cell 1.2 (original cell [10] and enlarged cells [1]).
3. **cell_13** folder: contains the .txt files for Cell 1.3 (original cell [10] and enlarged cells).

Additionally:

4. The **background** folder contains the .txt files of the background (gprMax results calculated without targets).
5. **MyPulse.txt**: .txt file of the pulse used for gprMax calculations.

The main settings to be used at Step 2 (see Subsection 2.3) are listed in Table 3.

The geometrical configuration and physical properties of Cells 1.1 and 1.2 are described in [1, 10]; SPOT-GPR results obtained for those cells are found in [1]. Here, we deal with Cell 1.3. The user is encouraged to try and reproduce the results presented in [1] and here, before using SPOT-GPR for the analysis of his/her own data.

Open access | www.GPRadar.eu/journal
Volume 1 | Issue 1 | January 2018

113

Published in Rome, Italy
by TU1208 GPR Association

https://doi.org/10.26376/GPR2018005

TABLE 2 – SETTINGS.

| SETTING NAME (Unit)	DEMO FILES DESCRIPTION AND COMMENTS
Centre frequency (MHz)	**Description**: Pulse centre frequency f_c transmitted by the GPR (Tx pulse). **Comments:** We call this quantity: f_c.
Bandwidth (MHz)	**Description:** Bandwidth of the Tx pulse. **Comments:** $[f_c-BB/2; f_c+BB/2]$. We suggest considering a -10 dB bandwidth.
Frequency resolution (MHZ)	**Description**: Frequency step to be used by the SAP-DoA procedure. For each frequency, the SAP-DoA procedure will estimate DoAs and triangulate them, thus producing a collection of crossings. **Comments:** For each point within the range $f_c-BB/2$: f_{RES}: $f_c+BB/2$, the procedure is executed. The crossing patterns are summed up: the global crossing pattern is the sum of the patterns obtained at each frequency.
Time sampling (ns)	**Description**: Tx/Rx time sampling. **Comments:** Assumed the same in Tx and Rx.
Scan spatial sampling (m)	**Description:** Distance between consecutive A-scan traces. **Comments:** Ideally this is the spacing of a linear uniform array collecting all the A-scans simultaneously. As in GPR applications the scenario does not change with time, the A-scans can be collected in different instants.
Antenna-ground distance (m)	**Description:** Distance between Tx/Rx antennas and the interface between air and the material hosting the targets. **Comments:** Assumed same for Tx and Rx antennas.
Dielectric constant of ground (N/A)	**Description:** Relative permittivity of ground. **Comments:** In release 1.0, this is a real value, i.e., losses are not considered by the SAP-DoA procedure.
False-alarm probability (N/A)	**Description:** False alarm probability used by the SAP-DoA procedure for the crossing pattern filtering. **Comments:** Typically between 10^{-3} and 10^{-6}, depending on f_{RES}. For a coarse f_{RES}, a lower number of crossings has to be expected and a lower false-alarm probability is recommended.
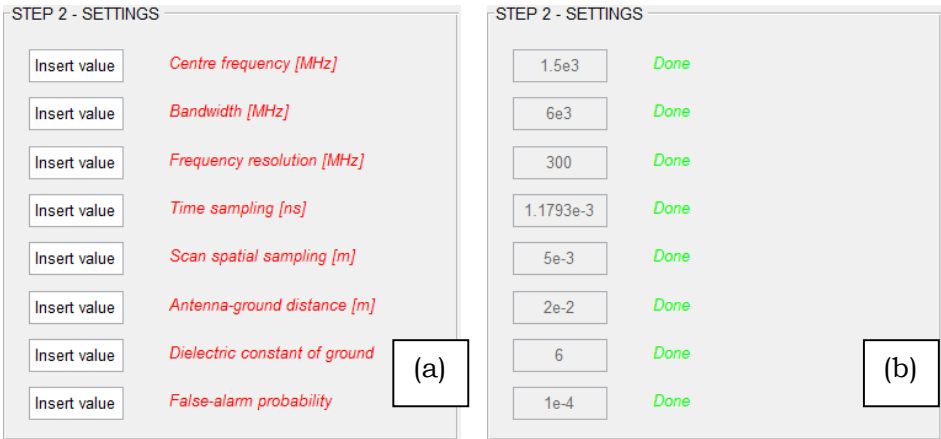
FIG. 5 – Step 2: Settings: (a) Before entering the settings and (b) after all settings have been entered (release 1.0).
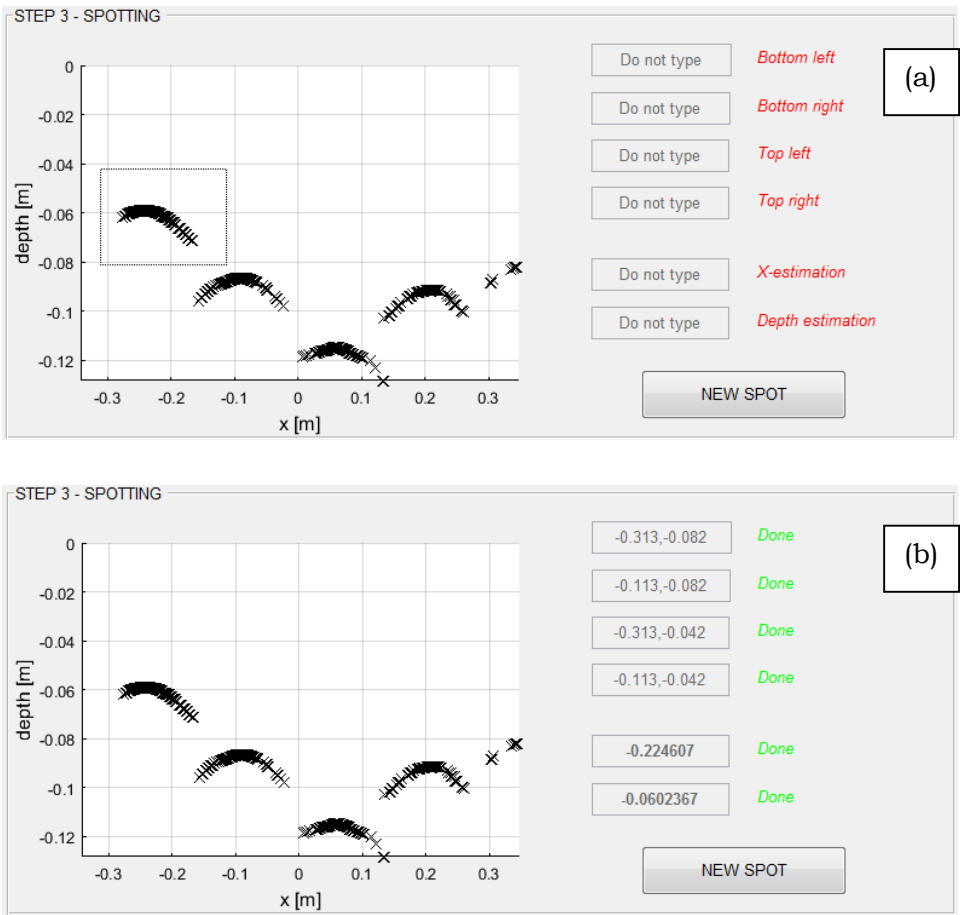
FIG. 6 – Step 3: Spotting: (a) SAP-DoA procedure output and (b) target position estimation (release 1.0).

Table 4 resumes the physical and geometrical properties of Cell 1.3, which transverse section is schematized in Figure 7; the Table describes also four enlarged versions of the same structure. The cell hosts three metallic ∟-, ─-, and ∪-shaped reinforcing elements and is positioned on a compacted fill. The original structure has a section of 60 × 18 cm; in this case, the reinforcing elements are rather close to each other and strong electromagnetic interactions take place when they are illuminated by a pulse emitted by a GPR; for this reason, although the geometry of the cell is rather simple, an accurate localization of the targets from GPR data is not a trivial task. We simulated four additional configurations, where we gradually increased the spacing between adjacent reinforcing elements with a 5-cm step, to investigate the performance of SPOT-GPR in the presence of different levels of interaction between targets.

TABLE 3 – MAIN SETTINGS FOR ALL DEMO FILES.

NAME	UNIT	VALUE
Center frequency	MHz	1.5E3
Bandwidth	MHz	6E3
Frequency resolution	MHz	300
Time sampling	ns	1.1793E-3
Scan spatial sampling	m	5E-3
Antenna-ground distance	m	2E-2
Dielectric constant of ground	N/A	6
False-alarm probability	N/A	1E-3 to 1E-6

In all the simulations, the central frequency of the pulse emitted by the GPR was f_c = 1.5 GHz. The transmitting antenna (a dipole) and the receiving antenna (not modelled) were at 2 cm from the air-concrete interface; the distance between the antennas was 10 cm. Results were calculated on a time window of 5 ns, by moving the antennas along a line orthogonal to the axes of the targets. The distance between consecutive traces was 5 mm and the time sampling respected the Courant stability condition. The relative permittivity of concrete was $\varepsilon_{r,c}$ = 6 and its conductivity was σ_c = 0.01 S/m (but, SPOT-GPR 1.0 does not take into account the effects of losses in the host medium). The

relative permittivity of the compacted fill was $\varepsilon_{r,cf}$ = 16 and its conductivity was σ_{cf} = 0.005 S/m.

Figure 8 shows the radargram obtained for the original version of Cell 1.3, Figure 9 shows the radargrams for the enlarged versions of the cell.

SPOT-GPR results are reported in Table 5, for the five considered configurations. For this cell, a hyperbolic fitting estimation would not yield good localization results, due to the shape and size of the targets: hyperbolic signatures in radargrams are generated by small circular-section targets. SPOT-GPR, instead, is capable to provide a rather accurate estimation of the positions of the targets; this result is considered to be significant, because it shows that our SAP-DoA approach can be successfully employed to detect objects different than cables, pipes and tubes.
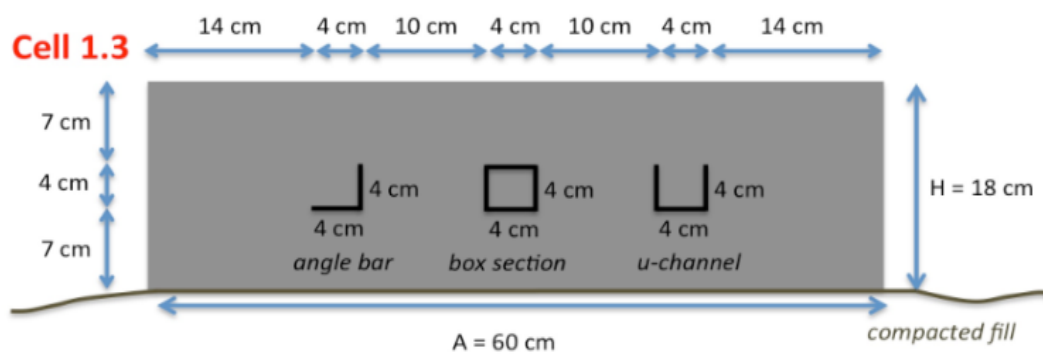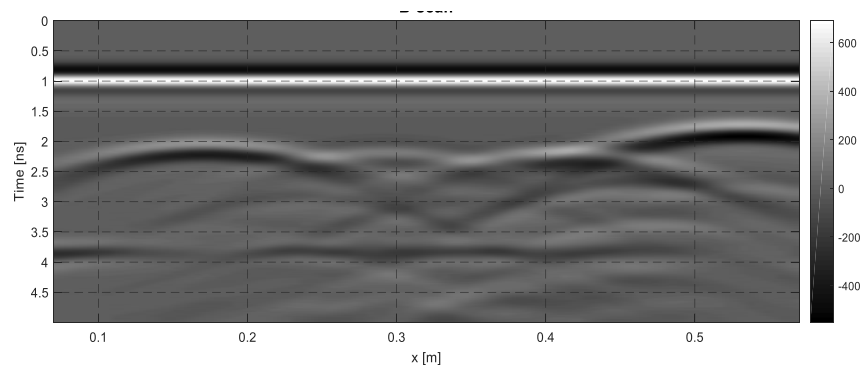

FIG. 7 – Geometry of Cell 1.3 [10].

FIG. 8 – Radargram for Cell 1.3 [10].

TABLE 4 – CELL 1.3 SCENARIO (*PEC* STANDS FOR PERFECTLY CONDUCTING).

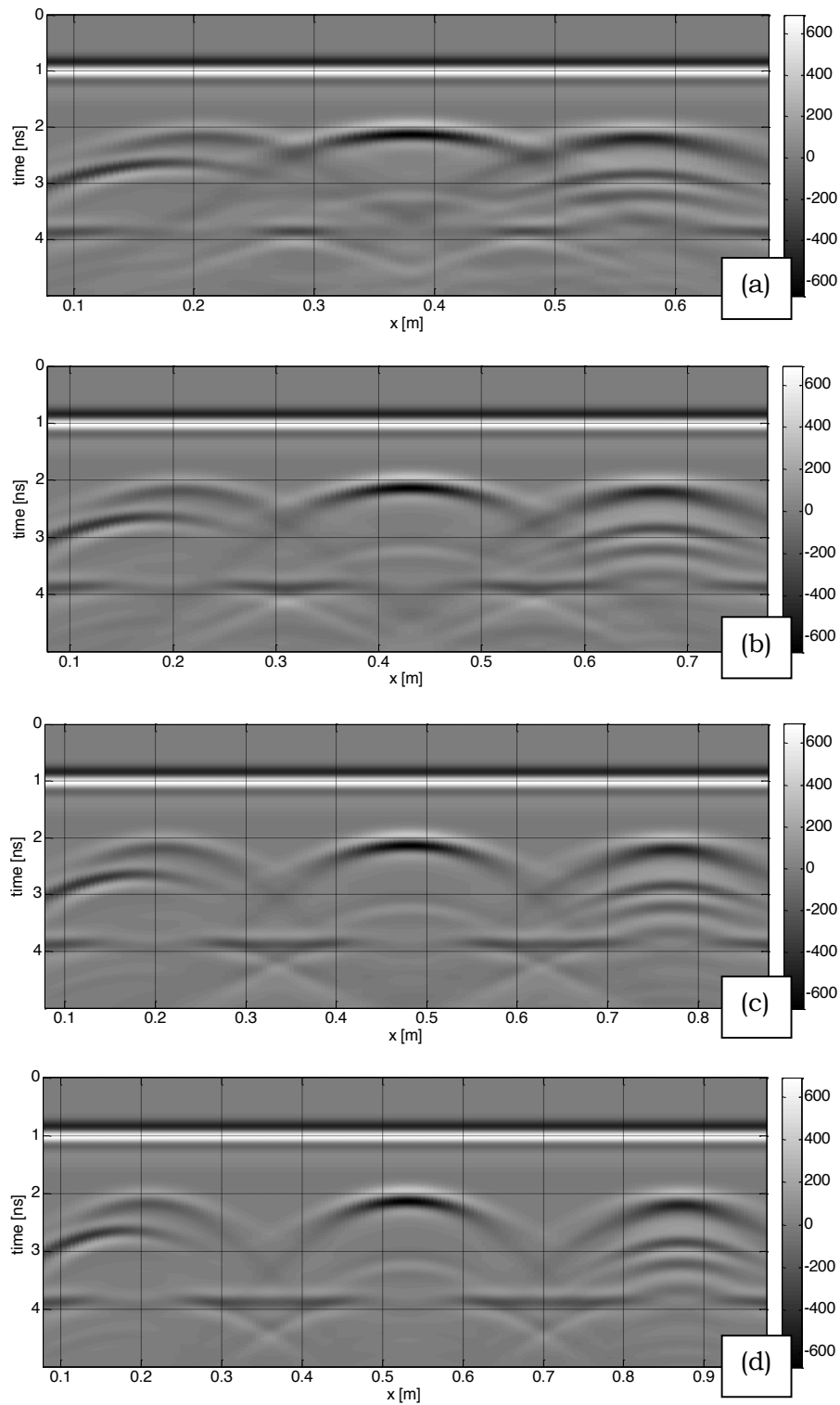| CELL 1-3 original			
Object	**Position [m]**	**Shape**	**Material**
No. 1: Left	X: from 0.17 to 0.21 Y: from 0.12 to 0.16	∟	Pec
No. 2: Centre	X: from 0.31 to 0.35 Y: from 0.12 to 0.16		Pec
No. 3: Right	X: From 0.45 to 0.49 Y: From 0.12 to 0.16	∪	pec
Cell section size: 0.60 x 0.28 cm² – **Number of traces in the radargram**: 100			
CELL 1-3 a)			
Object	**Position [m]**	**Shape**	**Material**
No. 1: Left edge	X: from 0.17 to 0.21 Y: from 0.12 to 0.16	∟	pec
No. 2: Centre	X: from 0.36 to 0.4 Y: from 0.12 to 0.16		pec
No. 3: Right edge	X: From 0.55 to 0.59 Y: From 0.12 to 0.16	∪	pec
Cell section size: 0.70 x 0.28 cm² – **Number of traces in the radargram**: 120			
CELL 1-3 b)			
Object	**Position [m]**	**Shape**	**Material**
No. 1: Left	X: from 0.17 to 0.21 Y: from 0.12 to 0.16	∟	pec
No. 2: Centre	X: from 0.41 to 0.45 Y: from 0.12 to 0.16		pec
No. 3: Right	X: From 0.65 to 0.69 Y: From 0.12 to 0.16	∪	pec
Cell section size: 0.80 x 0.28 cm² – **Number of traces in the radargram**: 140			
CELL 1-3 c)			
Object	**Centre position [m]**	**Shape**	**Material**
No. 1: Left	X: from 0.17 to 0.21 Y: from 0.12 to 0.16	∟	pec
No. 2: Centre	X: from 0.46 to 0.5 Y: from 0.12 to 0.16		pec
No. 3: Right	X: From 0.75 to 0.79 Y: From 0.12 to 0.16	∪	pec
Cell section size: 0.96 x 0.28 cm² – **Number of traces in the radargram**: 160			
CELL 1-3 d)			
Object	**Centre position [m]**	**Radius [m]**	**Material**
No. 1: Left edge	X: from 0.17 to 0.21 Y: from 0.12 to 0.16	N/A shape: ∟	pec
No. 2: Centre	X: from 0.51 to 0.55 Y: from 0.12 to 0.16	N/A shape:	pec
No. 3: Right edge	X: From 0.85 to 0.89 Y: From 0.12 to 0.16	N/A shape: ∪	pec
Cell dimensions: 1.06 x 0.28 cm² – **Number of traces in the radargram**: 180			
Relative permittivity medium 1: 6 (concrete) **Relative permittivity medium 2:** 16 (compacted fill)			
Trace spacing: 5 cm - **Time window**: 5 ns - **Centre freq**: 1500 MHz (Ricker pulse)			

FIG. 9 – Radargrams for enlarged versions of Cell 1.3. The distance between adjacent targets is increased of (a) 5 cm, (b) 10 cm, (c) 15 cm, and (d) 20 cm.

TABLE 5 – SPOT-GPR RESULTS FOR CELL 1.3: POSITION ERROR.

CELL 1-3 original	
Object	**SAP-DOA position error [m]**
No. 1: Left	(0.00001,-0.008)
No. 2: Centre	(-0.005, 0.008)
No. 3: Right	(0.0026, 0.008)
CELL 1-3 a)	
Object	**SAP-DOA position error [m]**
No. 1: Left	(0.001, 0.008)
No. 2: Centre	(-0.0005, 0.008)
No. 3: Right	(0.0033, 0.008)
CELL 1-3 b)	
Object	**SAP-DOA position error [m]**
No. 1: Left	(-0.013, 0.008)
No. 2: Centre	(-0.00425, 0.008)
No. 3: Right	(-0.001, 0.008)
CELL 1-3 c)	
Object	**SAP-DOA position error [m]**
No. 1: Left	(-0.01, 0.008)
No. 2: Centre	(-0.0014, 0.008)
No. 3: Right	(0.00001, 0.008)
CELL 1-3 d)	
Object	**SAP-DOA position error [m]**
No. 1: Left	(-0.01, 0.008)
No. 2: Centre	(0.0018, 0.008)
No. 3: Right	(0.003, 0.008)

3.   CONCLUSIONS

In this paper, practical information was given on how to use SPOT-GPR release 1.0, a freeware tool implementing a Sub-Array Processing (SAP) approach. The tool has a graphical user interface; it can be employed to analyse Ground-Penetrating Radar (GPR) data and estimate the position of targets in a two-dimensional scenario.

The implemented procedure is based on beamforming techniques widely used in radar systems different than GPR, consisting in the estimation of the Direction of Arrival (DoA) of the incoming signals, in order to decipher how many scatterers are present and predict their positions.

So far, SPOT-GPR was tested only on synthetic radargrams generated by using gprMax; in the near future, we plan to test our software on experimental data, as well (in particular, we will use the TU1208

Open access | www.GPRadar.eu/journal
Volume 1 | Issue 1 | January 2018

120

Published in Rome, Italy
by TU1208 GPR Association

https://doi.org/10.26376/GPR2018005

dataset coming from measurements performed at the IFSTTAR Geophysical Test Site, in Nantes, France).

In release 1.0 of SPOT-GPR, only the MUltiple SIgnal Classification (MUSIC) DoA algorithm is available; however, many other algorithms exist and can be easily implemented, such as the high-resolution approach Estimation of Signal Parameters via Rotational Invariance Technique (ESPRIT) [2]. Based on our preliminary investigations, MUSIC and ESPRIT are the most efficient DoA algorithms, for the purposes of analysing GPR radargrams. However, we already implemented and tested also the Bartlett, Capon, Linear Prediction, Maximum Entropy, Minimum Norm, and Pisarenko Harmonic Decomposition approaches. Because some users might be interested in comparing the performance of different algorithms on particular scenarios, we will release a new version of SPOT-GPR soon, where all these algorithms will be available.

Our plans for future work also include: the publication of results obtained by comparing SPOT-GPR with an automatic detection algorithm based on neural networks developed at the Faculty of Technical Sciences of Novi Sad (Serbia) [7]-[9]; and the integration of our SAP-DoA approach with Support-Vector-Machine techniques, in cooperation with the University of Genoa (Italy) [11]. The latter techniques are expected to increase the robustness of our approach with respect to the distance between sought targets, as they are considered to be more powerful than standard DoA algorithms in handling electromagnetic interactions between objects.

4.   ACKNOWLEDGEMENT

REFERENCES

[1]   S. Meschino and L. Pajewski, "SPOT-GPR: A Freeware Tool for Target Detection and Localization in GPR Data Developed within the COST Action

Open access | www.GPRadar.eu/journal
Volume 1 | Issue 1 | January 2018

121

Published in Rome, Italy
by TU1208 GPR Association

https://doi.org/10.26376/GPR2018005

TU1208," Journal of Telecommunications and Information Technology, 2017, vol. 3, pp.43-54.

[2]   S. Chandran, Advances in Direction-of-Arrival Estimation. Norwood, MA: Artech House, 2005.

[3]   R. Kumaresan and D. W. Tufts, "Estimating the angles of arrival of multiple plane waves," IEEE Transactions on Aerospace and Electronic Systems, vol. 19, no. 1, pp. 13–139, 1983.

[4]   C. E. Cook and M. Bernfeld, Radar Signals: An Introduction to Theory and Application, 1st ed. Artech House Radar Library, 1993.

[5]   C. Warren, A. Giannopoulos, and I. Giannakis, "gprMax: Open source software to simulate electromagnetic wave propagation for Ground Penetrating Radar," Computer Physics Communications, vol. 209, pp. 163–170, 2016.

[6]   Bello. Y. Idi and Md. N. Kamarudin, "Utility mapping with Ground Penetrating Radar: an innovative approach," Journal of American Science, vol. 7, no. 1, pp. 644–649, 2011.

[7]   A. Ristić, Ž. Bugarinović, M. Vrtunski, M. Govedarica and D. Petrovački, Integration of modern remote sensing technologies for faster utility mapping and data extraction, Construction and Building Materials, vol. 154, pp. 1183-1198, 2017.

[8]   A. Ristic, Z. Bugarinovic, M. Govedarica, L. Pajewski, and X. Derobert, "Verification of Algorithm for Point Extraction from Hyperbolic Reflections in GPR Data," 9th International Workshop on Advanced Ground Penetrating Radar, 28-30 June 2017, Nantes, France, pp. 1-5.

[9]   A. Ristic, M. Vrtunski, M. Govedarica, L. Pajewski, and X. Derobert, "Automated Data Extraction from Synthetic and Real Radargrams of District Heating Pipelines," 9th InternationalWorkshop on Advanced Ground Penetrating Radar, 28-30 June 2017, Nantes, France, pp. 1-5.

[10]   L. Pajewski, A. Giannopoulos, "Electromagnetic modelling of Ground Penetrating Radar responses to complex targets," Short Term Scientific Missions and Training Schools – Year 1, COST Action TU1208, L. Pajewski & M. Marciniak, Eds., Aracne Editrice, Rome, Italy, May 2014, ISBN 978-88-548-7225-7, pp. 7-45.

[11] M. Pastorino and A. Randazzo, "A smart antenna system for direction of arrival estimation based on a support vector regression," in IEEE Transactions on Antennas and Propagation, vol. 53, no. 7, pp. 2161-2168, July 2005.

THERMOGRAPHY: PRINCIPLES AND APPLICATIONS

MERCEDES SOLLA[1] & SUSANA LAGÜELA[2]

[1] DEFENSE UNIVERSITY CENTER, SPANISH NAVAL ACADEMY, MARÍN, SPAIN
MERCHISOLLA@CUD.UVIGO.ES

[2] UNIVERSITY OF SALAMANCA, DEPARTMENT OF CARTOGRAPHIC AND TERRAIN ENGINEERING, ÁVILA, SPAIN
SULAGUELA@USAL.ES

ABSTRACT

This tutorial presents the main principles of the thermography technique and the civil-engineering applications of this non-destructive testing method. Several examples are given and two case studies are presented, where thermography and Ground Penetrating Radar are jointly used to assess a radiant heating floor installed in a building, and to detect moisture in a masonry arch bridge.

KEYWORDS: Thermography; Ground Penetrating Radar; Non-destructive testing; Civil engineering.

1. FUNDAMENTALS OF THERMOGRAPHY

Infrared thermography is a non-destructive testing method based on the capacity of measuring temperature values from the radiation emitted by bodies in the thermal-infrared range of the electromagnetic spectrum.

The infrared range consists of four different bands, as shown in Table 1. The 5 – 7 μm band is not included in the table because it corresponds to the so-called 'low transmittance window,' where infrared radiation is not transmitted through the atmosphere. The 7 – 14 μm band, denominated 'Thermal Infrared' (TIR) can be related to temperature values. In particular, bodies that emit radiation in the TIR band have a temperature over absolute zero (0 K; -273.15 °C).

TABLE 1 – INFRARED BAND OF THE SPECTRUM

Band	Wavelength (μm)
Near Infrared (NIR)	0.4 – 1
Short-wave Infrared (SWIR)	1 – 3
Mid-wavelength infrared (MWIR)	3 – 5
Thermal Infrared (TIR)	7 – 14

Open access | www.GPRadar.eu/journal
Volume 1 | Issue 1 | January 2018

123

Published in Rome, Italy
by TU1208 GPR Association

https://doi.org/10.26376/GPR2018006

A thermographic camera captures radiation in the thermal infrared band and gives information about the temperature of the body under study. The radiation is received as an electric signal by the sensor, and its magnitude is directly related to the temperature of the body. The relationship between radiation and temperature is defined by the Stefan-Boltzmann law:

$$W_{bb} = \sigma T^4 \tag{1}$$

where W_{bb} is the radiation emitted by a black body, σ is Stefan-Boltzmann constant, equal to $5.67{\cdot}10^{-8}$ W/m^{2}K, and T is the temperature of the black body. This law is implemented in the camera, so that the user receives directly a temperature value per pixel.

Every object receives radiation from the Sun and surrounding elements, which acts in different ways once it reaches the object. The radiation arriving to an object is therefore divided into:

- ❑ Absorbed radiation. This is the portion of radiation that enters the object and changes its thermal condition, and consequently its temperature.
- ❑ Reflected radiation. This is the portion of radiation that does not enter the object.
- ❑ Transmitted radiation. This is the portion of radiation that enters the objects and travels through it without causing any important effect in the object.

The radiation outgoing from an object consists of emitted, reflected and transmitted radiations. The reflected radiation goes towards sources in front of the object, while the transmitted radiation goes to bodies behind the object. The emitted radiation can be associated to absorbed radiation: the absorbed radiation changes the thermal state of the body, and then the body emits radiation proportional to its temperature. This fraction of radiation is commonly denoted by the term 'emissivity' and represented by the symbol ε. Transmitted radiation is considered as null for non-transparent bodies: for such bodies, outgoing radiation consists of the emitted and reflected portions, only.

The emissivity is an essential parameter to be taken into account for a correct calculation of a real-body temperature with respect to the temperature of a black body. A black body is an unreal object with a

Open access | www.GPRadar.eu/journal
Volume 1 | Issue 1 | January 2018

124

Published in Rome, Italy
by TU1208 GPR Association

https://doi.org/10.26376/GPR2018006

perfect behaviour regarding emittance; thus, all radiation emitted by a black body is the result of its temperature, without a reflected portion. For this reason, the emissivity value of a black body is 1, while real bodies present emissivity values from 0.1 to 0.99. Because total radiation is quantified as 1, the portion of radiation that is not emitted, is reflected. Thus, bodies with high reflectivity present low emissivity, and vice versa. For example, construction materials commonly present emissivity between 0.9-0.96; non-oxidized metals present low emissivity, ranging between 0.2 and 0.5 [1]. Regarding temperature calculation, emissivity is introduced in Stefan-Boltzmann law as follows:

$$W_{bb} = \varepsilon \sigma T^4 \tag{2}$$

The emissivity value of materials can be extracted from tables [1], through the simultaneous measurement of the object under study and a piece of black tape with known emissivity [2], or by direct computation based on Equations (1) and (2), by using apparent temperature values measured with a camera and real temperature values measured with a contact thermometer [3].

In addition to emissivity, other factors influence the quantity of radiation emitted by each body (see Figure 1), as well as the quantity of radiation received by the camera. The attenuation effect of the atmosphere on the infrared radiation coefficient is taken into account to correct the computation of the temperature value. This attenuation coefficient depends on three factors: distance to the objects from the camera, ambient temperature and relative humidity.

Deeper explanation about fundamentals and principles of infrared thermography are found in the literature [3, 4].

2.   CLASSIFICATION OF THERMOGRAPHIC APPROACHES

There are two classifications of infrared thermography methods, based on the possible presence of a heat source, on the relative positions between camera, object under study and heat source, and on the importance given to the temperature value (e.g., whether temperature differences or temperature absolute values are measured and interpreted). More details are given in the following sub-sections.
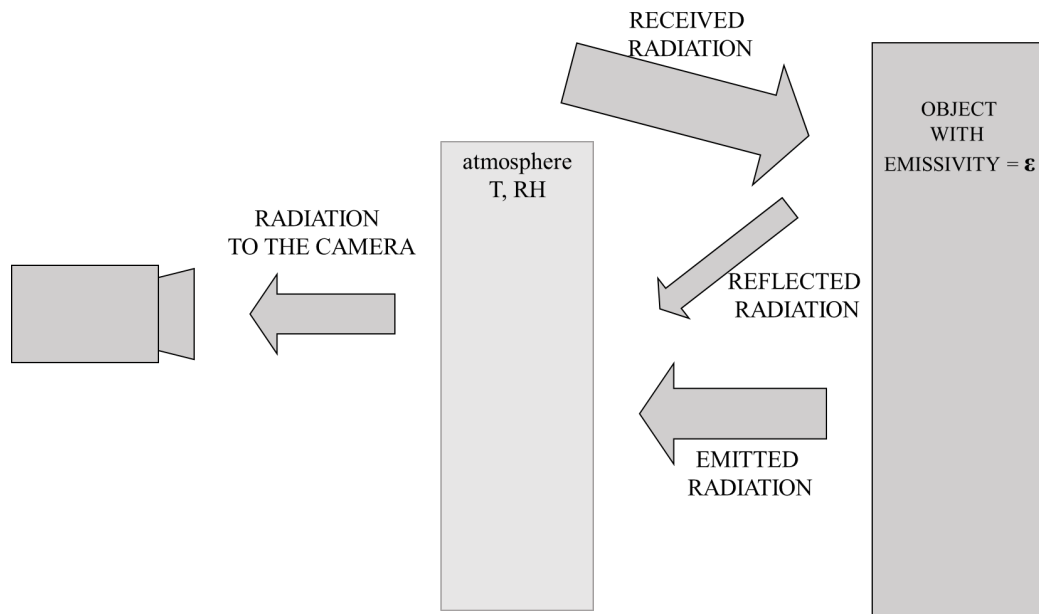
Open access | www.GPRadar.eu/journal
Volume 1 | Issue 1 | January 2018

125

Published in Rome, Italy
by TU1208 GPR Association

https://doi.org/10.26376/GPR2018006

FIG. 1 – Distribution of infrared radiation [3].

2.1. ACTIVE VERSUS PASSIVE APPROACHES

❑ Passive thermography: no external heat source is used. The camera measures the radiation of the objects under test in their normal state, that is, under the usual conditions of received radiation. The Sun is not considered as an external heating source in this classification, due to its natural presence, but of course its presence (or absence) is important for the correct development of the study.

❑ Active thermography: implies the use of an artificial heat source. The heat source can vary from pulsed laser and flash lamps [5, 6], to non-optical sources such as mechanical vibration, acoustic wave excitation and microwaves [7-9]. Active thermography is divided into transmission-mode thermography and reflection-mode thermography, depending on the relative positions between camera, object and heat source, and the consequent origin of the radiation measured (see Figure 2).
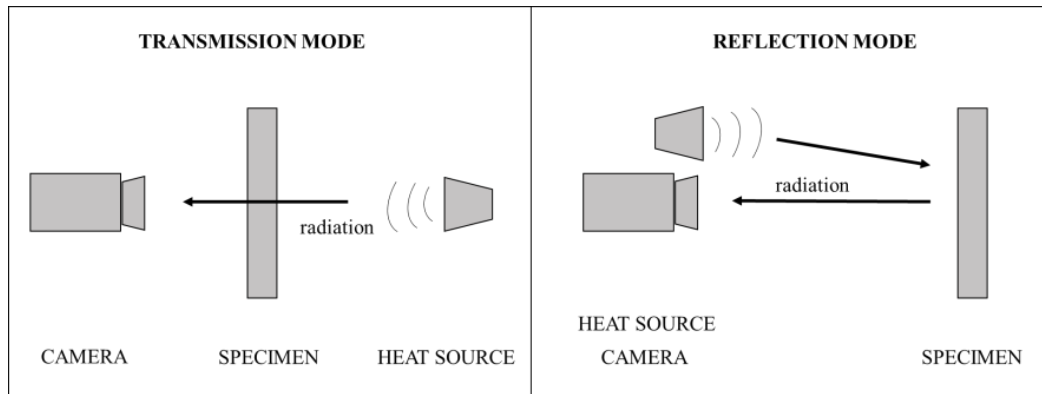
FIG. 2 – Configuration of transmission and reflection mode thermography, for active thermography [3].

2.2. QUALITATIVE VS QUANTITATIVE APPROACHES

❑ Qualitative thermography is focused on the search of thermal pathologies in the objects, based on temperature differences instead of temperature values. Thus, in this approach, the evaluation of real absolute temperatures is not the objective of the study and relative temperatures are measured. In this way, the presence of thermal anomalies can be detected.

   E.g.: detection of moisture areas in buildings.

❑ Quantitative thermography is an approach based on the accurate measurement of temperature values. This method requires the application of both emissivity and ambient compensations, as well as a careful data acquisition, taking into account every factor of influence such as the presence of reflectors and air currents. This approach allows the evaluation of the severity of the problems and the thermal characterization of the objects.

   E.g.: identification of pathology as a critical or a medium problem, estimation of thermal diffusivity of a material.

Qualitative studies are based on passive thermography; whereas quantitative analysis is based on both passive and active approaches.

Open access | www.GPRadar.eu/journal
Volume 1 | Issue 1 | January 2018

127

Published in Rome, Italy
by TU1208 GPR Association

https://doi.org/10.26376/GPR2018006

3. CIVIL ENGINEERING APPLICATIONS OF INFRARED THERMOGRAPHY

3.1. BUILDING INSPECTION

Possible tasks performed in buildings, where infrared thermography finds application, are:

- Detection of structural defects, such as joint failure, cracking, delamination/detachment and moisture/efflorescence [10-12].

- Detection of thermal bridges, i.e., areas where heat transfer is facilitated due to the construction weakness (e.g. no insulation in junctions between walls and the building envelop) [13].

- Detection of tightness weaknesses, allowing the escape of heated air from the interior (e.g. no sealing around elements such as windows, free space under doors) [14].

- Detection of air infiltration, similar to the previous failure but allowing the entrance of exterior air in the building (e.g. around windows and doors without sealing)[14].

- Detection of building installations and pathologies (e.g. electricity, plumbing) [15].

As an example, Figure 3 presents two thermal images showing: a case of lack of insulation around the windows, and of thermal bridge between the facade and roof, where red/yellow colours indicate higher temperatures or heated air from the interior (left panel); a case of air infiltration where dark blue colours indicate lower temperatures or colder air entering from the exterior (right panel).

3.2. CIVIL INFRASTRUCTURE INSPECTION

Possible tasks performed in civil infrastructure assessment, where infrared thermography finds application, are:

- Security and safety issues, such as pedestrian [16] or vehicle [17] recognition, which was the first application of infrared thermography as a night-vision tool.
- Inspection of pavement (e.g. cracks) [18].

- Diagnosis of bridges and tunnels (e.g. moisture or delamination areas in concrete bridges) [19-22].

Figure 4 illustrates an example of cracking in asphalt pavement. The presence of cracks is associated with red colour, given that cracks allow the accumulation of air inside, and the inspection was performed during a day with ambient temperature around 31°C.

Figure 5 shows an example of a masonry arch bridge inspected by means of infrared thermography. In the thermal images, colours go from dark red for the lowest temperatures, to red, light red, orange, yellow and white for the highest temperatures. The analysis of the thermal images leads to the detection of moisture in the central part of the arch, and near the border with the pathway. The presence of water becomes more evident in the downstream wall of the same arch (left), where water can be detected all around the arch in spite of the presence of a large quantity of vegetation hiding part of the faults.
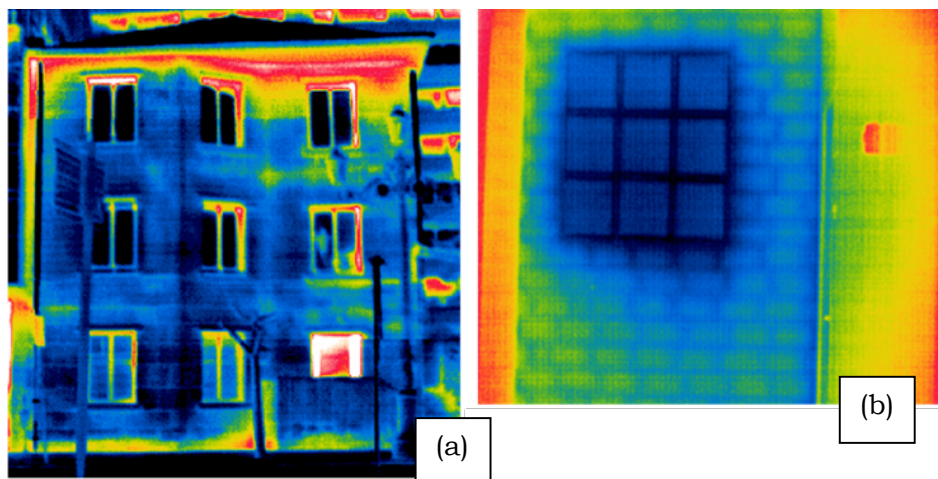

FIG. 3 –Examples of (a) lack of insulation around windows and (b) air infiltration from the exterior of the building.
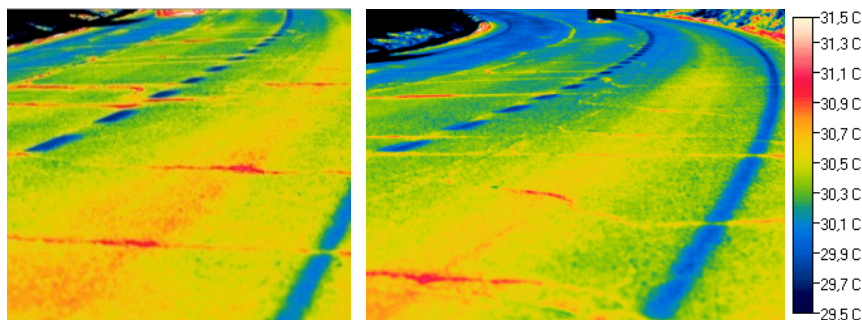

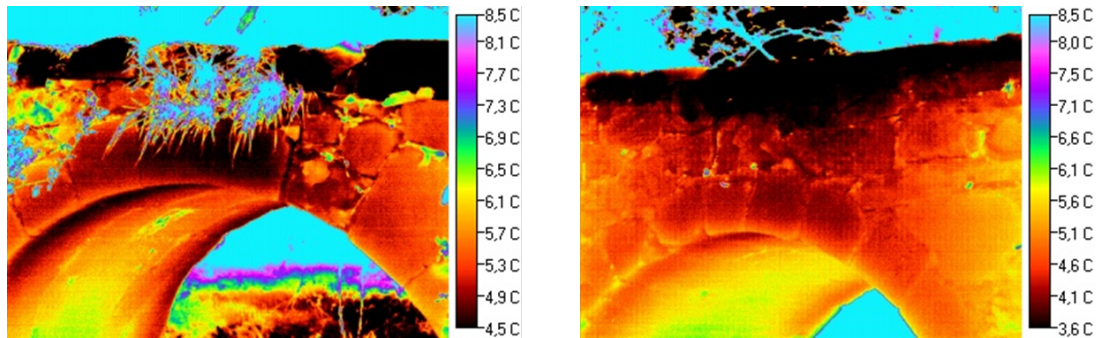**FIG. 4 –**Example of cracking in asphalt pavement.

Open access | www.GPRadar.eu/journal
Volume 1 | Issue 1 | January 2018

129

Published in Rome, Italy
by TU1208 GPR Association

https://doi.org/10.26376/GPR2018006

FIG. 5 – Example of thermographic survey to detect moisture in a masonry bridge: downstream wall on the left, upstream wall on the right.

3.3   INSPECTION OF HERITAGE SITES

Possible tasks where infrared thermography finds application are:

- Identification of archaeological remains due to the presence of subsurface air cavities [23, 24].
- Diagnosis of paintings and murals (e.g. cracks, holes, voids) [25, 26].
- Monument conservation (moisture, cracks, temperature evolution) [27-29].

Figure 6 shows thermal images acquired in the ruins of a historic church. Most pathologies detected in the inspection were structural (loose rocks, left panel) and presence of moisture with different levels of severity (right panel).
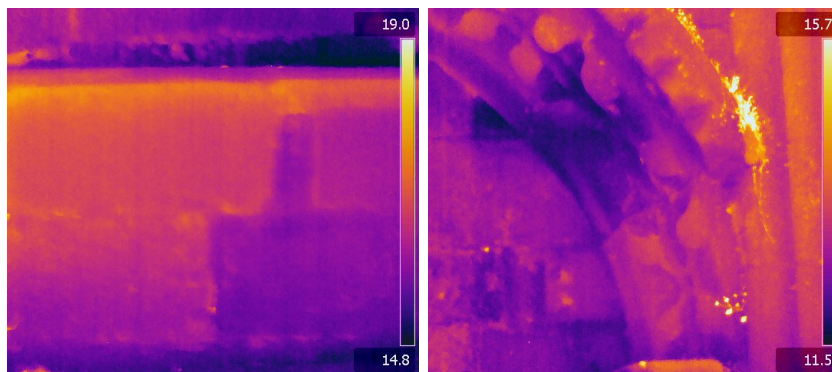

FIG. 6 – Example of thermographic survey in the ruins of a historic church. Thermal images show a loosened stone (left), presence of moisture within the masonry, efflorescence and moss (right).

Open access | www.GPRadar.eu/journal
Volume 1 | Issue 1 | January 2018

130

Published in Rome, Italy
by TU1208 GPR Association

https://doi.org/10.26376/GPR2018006

Figure 7 is a thermal image of a cave painting in Cáceres (Spain). The objective of the study is to determine the ambient conditions of the cave in order to evaluate the need of measures to optimize the conservation of the paintings. Blue colour is associated to the lowest temperatures, with increasing temperatures corresponding to green, yellow and red.
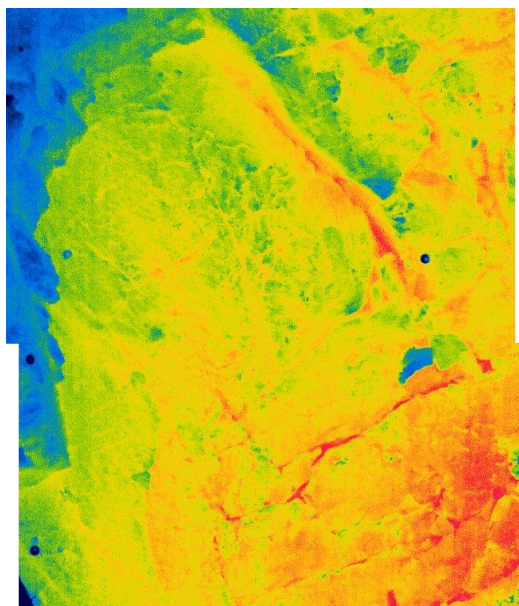

FIG. 7 – Thermal image of a cave painting, showing an increasing trend for the temperature from top to bottom of the cave.

4. COMBINING INFRARED THERMOGRAPHY AND GROUND PENETRATING RADAR

4.1. DETECTION OF BUILDING INSTALLATIONS (RADIANT HEATING FLOOR) [30]

Infrared thermography

o The thermographic survey was developed with an active approach, in the transmission mode, as the installation is used as heating source.

o The installation was turned on 5 h before the inspection, with the aim to reach a 5-10ºC temperature difference between the pipelines and the surrounding environment. The existence of a temperature difference allows for the determination of thermal anomalies due to defects in the installation.

Open access | www.GPRadar.eu/journal
Volume 1 | Issue 1 | January 2018

131

Published in Rome, Italy
by TU1208 GPR Association

https://doi.org/10.26376/GPR2018006

o The thermographic inspection was performed by using a NEC TH9260 camera with a 640*480UFPA sensor, having a 0.06°C resolution and ±2°C accuracy.

o A single image could not cover the dimensions of the grid or area under study. Three different thermal images were therefore acquired to create a thermographic mosaic covering the whole area.

o In order to avoid reflections, their main source, lamps, were off during the inspection. In addition, the camera operator was located at a 90° angle so that the reflection by his body did not affect the measurement.
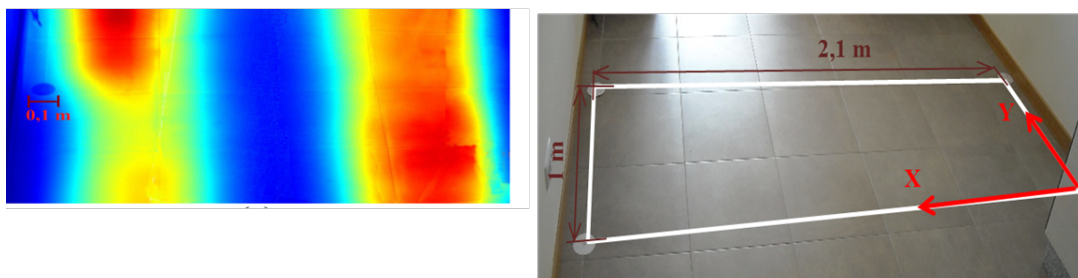
The results of the investigation are shown in Figure 8.

FIG. 8 – Thermographic mosaic (adapted from [30]) on the left; dark red colours represent higher temperatures (pipeline paths). Photo of the inspect surface on the right.

Ground Penetrating Radar

o A ProEx Ground Penetrating Radar (GPR) system was used, with a 2.3-GHz antenna. This frequency was selected because, in the considered scenario, it provides a signal penetration depth of about 40 cm and a vertical resolution of about 1-2 cm.

o The survey was carried out with a 2-cm spatial sampling and a 12-ns time window.

o An encoder-based wheel was attached to the antenna, as a distance measurement instrument, to measure the profile length and to control the 2 cm spatial sampling.

Open access | www.GPRadar.eu/journal
Volume 1 | Issue 1 | January 2018

132

Published in Rome, Italy
by TU1208 GPR Association

https://doi.org/10.26376/GPR2018006

o The data were collected with the antenna polarization orthogonal to the longitudinal direction of the heating pipelines (X direction in the right panel of Figure 8).

o Three-dimensional (3D) data acquisition of equidistant parallel profiles, at regular intervals of 5 cm, was done.

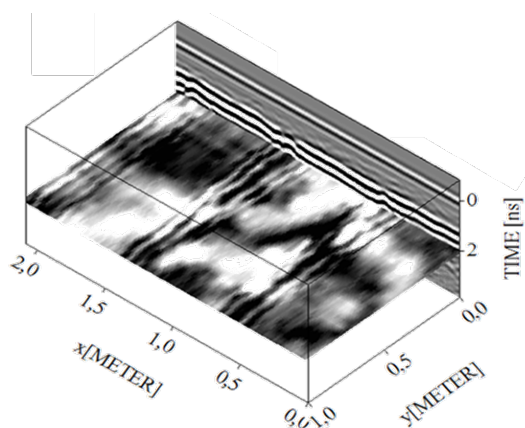The results of the investigation are shown in Figure 9.

FIG. 9 – Results of the GPR survey (adapted from [30]).

Discussion of the results and integrated interpretation

o GPR provided information about the number of pipelines and distribution. In particular, GPR data revealed the presence of three pipelines.

o The thermographic mosaic showed the presence of two pipelines.

o The spatial correspondence between radargram and thermographic mosaic (see Figure 10) leads to the conclusion that the central pipeline is not working.

o GPR gives information about all pipelines but cannot distinguish whether they are working or not. Thermography can detect only the working installations.

o The different thermal print between the pipelines on the left and on the right shows a malfunctioning of the pipeline on the left, given its colder temperature distribution.
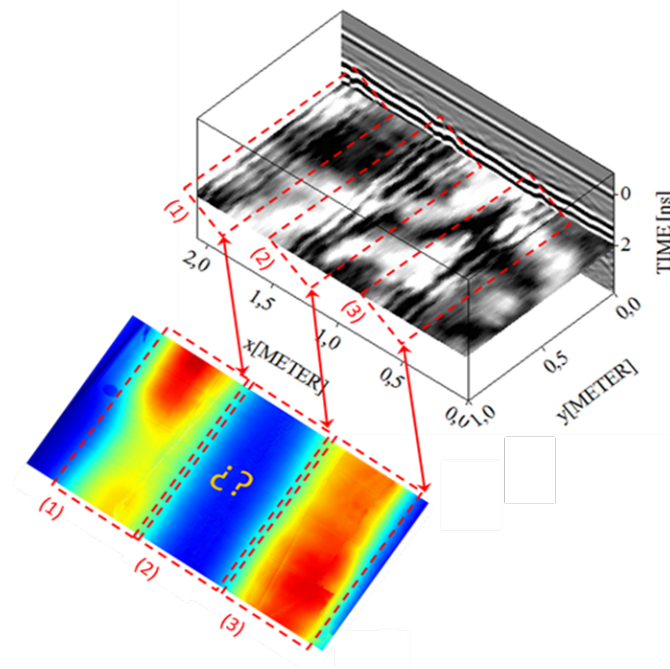
Open access | www.GPRadar.eu/journal
Volume 1 | Issue 1 | January 2018

133

Published in Rome, Italy
by TU1208 GPR Association

https://doi.org/10.26376/GPR2018006

FIG. 10 – Comparison of 3D GPR data and thermographic mosaic (adapted from [30]).

4.2.   DETECTION OF MOISTURE IN MASONRY ARCH BRIDGES [31]

Infrared thermography

o The thermographic survey was developed with a passive approach.

o The passive solar radiation was used to increase the evaporation rate of water inside the structure and to maximize the temperature difference between moist and dry areas thanks to the evaporation process.

o Environment conditions were: a temperature of 10°C, with 40% relative humidity.

o Object distance: ~ 5m (see Figure 11(a)).

o Emissivity value: 0.80 (test in situ).

o The thermographic inspection was performed by using aNEC TH9260 camera with a 640*480UFPA sensor, with 0.06°C resolution and ±2°C accuracy.

Open access | www.GPRadar.eu/journal
Volume 1 | Issue 1 | January 2018

134

Published in Rome, Italy
by TU1208 GPR Association

https://doi.org/10.26376/GPR2018006

o The thermographic survey included the walls of the bridge (both upstream and downstream walls) and the inner part of the vault of the arch under study.

o The temperature interval selected was from 6 to 12ºC, with colours going from dark red for the lowest temperatures, to red, light red, orange, yellow and white for the highest temperature (see Figure 11(b)).

o The thermal images obtained were also registered in a 3D model see Figure 11(d)), enabling the study of the complete vault instead of studying each thermal image separately, thus reducing the confusion caused by the lack of reference points in individual images.

o The 3D model was provided through photogrammetric approaches, by using a digital camera Nikon D200 (see Figure 11(c)).

o Finally, in order to avoid the effects of the perspective view, each wall, upstream and downstream, were orthogonally projected to the parallel plane, and the corresponding orthothermograms were obtained (see Figure 11(e)).
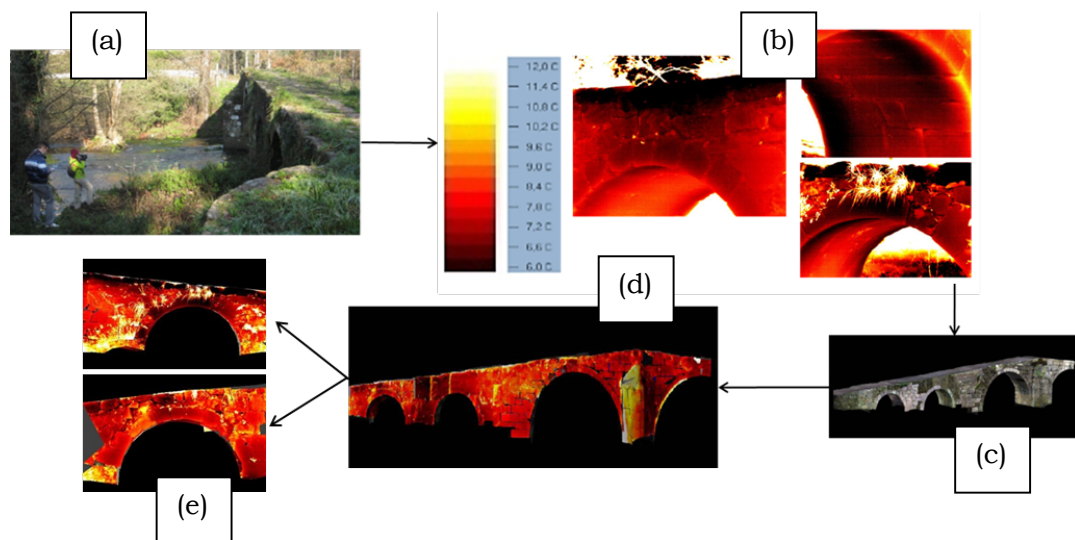

FIG. 11 – Results of the thermographic survey: (a) data acquisition, (b) orthothermograms, (c) 3D model with RGB texture, (d) 3D model with thermographic texture, and (e) orthothermograms of the arch under study.

Open access | www.GPRadar.eu/journal
Volume 1 | Issue 1 | January 2018

135

Published in Rome, Italy
by TU1208 GPR Association

https://doi.org/10.26376/GPR2018006

Ground Penetrating Radar

o The GPR data were collected with a RAMAC/GPR CU-II system.

o The 1-GHz antenna was chosen because it provides a signal penetration depth of about 1 m and a vertical resolution of about 4 cm.

o The survey parameters were: 2-cm spatial sampling and 45-ns time window.

o The GPR survey was carried out passing the GPR antenna around the internal surface of the vault (see Figure 12) in order to avoid scattering and complex reflection patterns produced by the heterogeneous filling commonly used during construction.

o An encoder-based wheel was attached to the back of the antenna to measure the profile lengths as well as to control the spatial sampling.

FIG. 12 – 1-GHz GPR data acquisition through the intrados of the vault arch.

Results and combined interpretation:

o The orthothermograms of both the upstream and downstream walls of the bridge were obtained from the thermographic 3D model.

o The thermography results facilitated the identification of probable moist areas in the bridge surface as those having lower temperatures (dark red). This is due to the cooling effect of evaporation on the surface where it takes place.

o Important evidence of moisture appears on the upper part of the walls, near the border with the road, and in the masonry over the arch (Figure 13(a)).

o GPR provided information on the inner materials of the bridge. Observing the radargram, a stronger reflection generated from the backfill/stone interface can be noted (red arrow in Fig. 13(b)), which is clearly visible only in the zones contiguous to the keystone of the arch (≈ at 20 ns). The most probable explanation is that water could be accumulated there.

o The GPR interpretation agreed with the thermographic data obtained, which showed a more critical presence of water (dark red areas) around the keystone, more pronounced towards the face of the upstream wall.
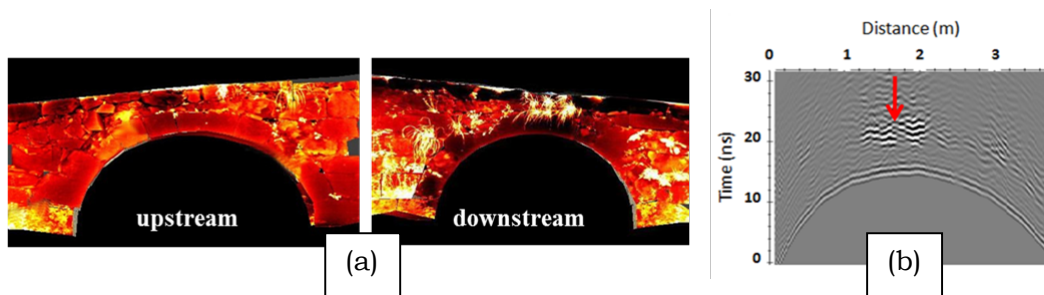

FIG. 13 – (a) Orthothermograms obtained from both the upstream and downstream walls of the bridge and (b) 1-GHz GPR data.

5. CONCLUSIONS

Thermal infrared thermography has proved to be an adequate technique for detecting and analysing faults and pathologies that can affect heat transfer. Although the technique only provides information from the surface of the objects, different procedures allow the extraction of information from the subsurface, such as heating from an external source (Sun radiation or artificial sources).

Thermal infrared thermography is a good complementary technique to Ground Penetrating Radar (GPR), both prior and during the GPR inspection. In the first case, infrared thermography can provide information about the presence of water or the conductivity of the material under study, so that the GPR processing can be optimized. In

the second case, infrared thermography can yield information concerning the most superficial part of the inspected object, where the GPR signal can be less accurate than in deeper regions. Thus, both techniques can be used jointly to perform a more exhaustive analysis about the state of constructions.

ACKNOWLEDGEMENTS

REFERENCES

[1]   T. Suesut, N. Nunak, T. Nunak, A. Rotrugsa, and Y. Tuppadung, "Emissivity measurements on material and equipment in electrical distribution system," International Conference on Control, Automation and Systems, Gyeonggi-do, South Korea, October 2011.

[2]   P. Fokaides, S. Kalogirou, "Application of infrared thermography for the determination of the overall heat transfer coefficient (U-value) in building envelopes", Applied Energy, vol. 88, pp. 4358-4365, 2011.

[3]   S. Lagüela, L. Díaz-Vilariño, and D. Roca, "Infrared thermography: fundamentals and applications," book chapter in Non-destructive techniques for the evaluation of Structures and Infrastructures (Eds. B. Riveiro and M. Solla), CRC/Balkema, Taylor & Francis Group, 2016.

[4]   C. Meola and G. Carlomagno, "Recent advances in the use of infrared thermography", Measurement Science and Technology, vol. 15, pp. 27-58, 2004.

[5]   L. Teng, D. Almond, D. Andrew and S. Rees, "Crack imaging by scanning pulsed laser spot thermography", NDT&E International, vol. 44, pp. 216-25, 2011.

[6]   N. Tsopelas, N. Siakavellas, "Experimental evaluation of electromagnetic-thermal non-destructive inspection by eddy current thermography in square aluminium plates", NDT&E International, vol. 44, pp. 609-620, 2011.

Open access | www.GPRadar.eu/journal
Volume 1 | Issue 1 | January 2018

138

Published in Rome, Italy
by TU1208 GPR Association

https://doi.org/10.26376/GPR2018006

[7]   L. Favro, X. Han, Z. Ouyang, G. Sun, H, Sui, R. Thomas, "Infrared imaging of defects heated by a Sonic pulse", Review of Scientific Instruments, vol. 71, pp. 2418-2421, 2000.

[8]   F. Mabrouki, M. Thomas, M. Genest, A. Fahr, "Numerical modelling of vibrothermography based on plastic deformation", NDT&E International, vol. 43, pp. 476-483, 2010.

[9]   S. Keo, F. Brachelet, F. Breaban and D. Defer, "Steel detection in reinforced concrete wall by microwave infrared thermography", NDT&E International, vol. 62, pp. 172-177, 2014.

[10]   Ch. Maierhofer, R. Arndt, M. Röllig, C. Rieck, A. Walther, H. Scheel, and B. Hillemeier, "Application of impulse-thermography for non-destructive assessment of concrete structures," Cement and Concrete Composites, vol. 28(4), pp. 393-401, 2006.]

[11]   S. Bagavathiappan, B.B. Lahiri, T. Saravanan, J. Philip, and T. Jayakumar, "Infrared thermography for condition monitoring – A review," Infrared Physics & Technology, vol. 60, pp. 35-55, 2013.

[12]   M.R. Clark, D.M. McCann, and M.C. Forde, "Application of infrared thermography to the non-destructive testing of concrete and masonry bridges," NDT & E International, vol. 36(4), pp. 265-275, 2003.

[13]   F. Bianchi, A. Pisello, G. Baldinelli, and F. Asdrubali, "Infrared thermography assessment of thermal bridges in building envelope: experimental validation in a test room setup," Sustainability, vol. 6(10), pp. 7107-7120, 2014.

[14]   C.A. Balaras, and A.A. Argiriou, "Infrared thermography for building diagnostics," Energy and Buildings, vol. 34, pp. 171-183, 2012.

[15]   N. Laaidi, S. Belattar, and A. Elbaloutti, "Pipeline corrosion, modelling and analysis," Journal of Nondestructive Evaluation, vol. 30(3), pp. 158-163, 2011.

[16]   M. Khozium, A. Abuarafah, and E. AbdRabou, "A proposed computer-based system architecture for crowd management of pilgrims using thermography," Life Science Journal, vol. 9(2), pp. 277-282, 2012.

[17]   Y. Iwasaki, S. Kawata, and T. Nakamiya, "Robust vehicle detection even in poor visibility conditions using infrared thermal images and its application to road traffic flow monitoring," Measurement Science and Technology, vol. 22(8), 085501 (10pp), 2011.

[18]   M. Solla, S. Lagüela, and H. González-Jorge, "Approach to identify cracking in asphalt pavement using GPR and infrared thermographic

Open access | www.GPRadar.eu/journal
Volume 1 | Issue 1 | January 2018

139

Published in Rome, Italy
by TU1208 GPR Association

https://doi.org/10.26376/GPR2018006

methods: Preliminary findings," NDT&E International, vol. 62, pp. 55-65, 2014.

[19]   J. Dumoulin, A. Crinière, and R. Averty, "The detection and thermal characterization of the inner structure of the Musmeci bridge deck by infrared thermography monitoring," Journal of Geophysics and Engineering, vol. 10(6), 064003 (11pp), 2013.

[20]   M. Matsumoto, K. Mitani, F. Catbas, and S. Hayashi, "On-site application of innovative bridge inspection methods using image processing and infrared technology," 7th International Conference on Bridge Maintenance, Safety and Management, Shanghai, China, July 2014.

[21]   T. Sakagami, "Remote non-destructive evaluation technique using infrared thermography for fatigue cracks in steel bridges," Fatigue and Fracture of Engineering Materials and Structures, vol. 38(7), pp. 755-779, 2015.

[22]   G. Barla, F. Antolini, and G. Gigli, "3D Laser scanner and thermography for tunnel discontinuity mapping," Geomechanics and tunnelling, vol. 9(1), pp. 29-36, 2016.

[23]   B. Lunden, "Aerial thermography: a remote sensing technique applied to detection of buried archaeological remains at a site in Dalecarlia, Sweden," Geografiska Annaler, vol 67(1), pp. 161-166, 1985.

[24]   J. Casana, J. Kantner, A. Wiewel, and J. Cothren, "Archaeological aerial thermography: a case study at the Chaco-era Blue J community, New Mexico," Journal of Archaeological Science, vol. 45, pp. 207-219, 2014.

[25]   F. Mercuri, U.Zammit, N.Orazi, S.Paoloni, M.Marinelli, andF. Scudieri, "Activeinfrared thermography applied to the investigation of art and historic artefacts,"Journal of Thermal Analysis and Calorimetry, vol. 104, pp. 475-485, 2011.

[26]   E. Kordatos, D.Exarchos, C.Stavrakos, A.Moropoulou, andT. Matikas, "Infrared thermographicinspection of murals and characterization of degradation in historic monuments," Construction and Building Materials, vol. 48, pp. 1261-1265, 2013.

[27]   E. Rosina, and J. Spodek, "Using infrared thermography to detect moisture in historicmasonry: a case study in Indiana," APT Bulletin, vol. 34(1), pp. 11-16, 2003.

[28]   A. Kandemir-Yucel, A.Tavukcuoglu, and E. Caner-Saltik, "In situ assessment of structuraltimber elements of a historic building by infrared thermography and ultrasonic velocity," Infrared Physics & Technology, vol. 49, pp. 243-248, 2007.

Open access | www.GPRadar.eu/journal
Volume 1 | Issue 1 | January 2018

140

Published in Rome, Italy
by TU1208 GPR Association

https://doi.org/10.26376/GPR2018006

[29]   E. Rosina, S. Della Torre, P.Gasparoli, L.Lazzaroni, L. Di Bella, A. Castiglioni, M.Radaelli, and C.Sotgia, "Localizing historical clues using IRT and petrographic analysis at Villa Mirabello, Monza (Italy)," Archaeometry, vol. 51(5), pp. 715-732, 2009.

[30]   S. Lagüela-López, M. Solla-Carracelas, L. Díaz-Vilariño, and J. Armesto-González,"Inspection of radiant heating floor applying non-destructive testing techniques: GPR and IRT," DYNA Colombia, 82(190), pp. 221-226, 2015.

[31]   M. Solla, S. Lagüela, B. Riveiro, andH. Lorenzo, "Non-destructive testing for the analysisof moisture in the masonry arch bridge of Lubiáns (Spain)," Structural Control and Health Monitoring, vol. 20, pp. 1366-1376, 2013.

Open access | www.GPRadar.eu/journal
Volume 1 | Issue 1 | January 2018

141

Published in Rome, Italy
by TU1208 GPR Association

https://doi.org/10.26376/GPR2018006

TABLE OF CONTENTS